Single and Entangled Photon Manipulation for Photonic Quantum Technologies

A thesis submitted for the degree of

Doctor of Philosophy

by

XIANG ZHANG

Centre for Ultrahigh bandwidth Devices for Optical Systems (CUDOS)

Institute of Photonics and Optical Science (IPOS)

School of Physics

University of Sydney

2019

Declaration of Originality

I declare that this thesis titled 'Single and entangled photon manipulation for photonic quantum technologies' and the work presented in it are my own. I confirm that:

- This thesis describes work performed by myself and colleagues at the University of Sydney.
- Where any part of this thesis has previously been submitted for a degree or any other qualification at this University or any other institution, this has been clearly stated.
- Where I have consulted the published work of others, this is always clearly attributed.
- Where I have quoted from the work of others, the source is always given. With the exception of such quotations, this thesis is entirely my own work.
- I have acknowledged all main sources of help.
- Where the thesis is based on work done by myself jointly with others, I have made clear exactly what was done by others and what I have contributed myself.

Signature

Date

Acknowledgements

I leave this part at the end of the thesis writing, because I want to review every memorable moment during last four years. I realize it is such a long list to appreciate. I am a lucky man. I have received endless love and infinite support from my Mum and Dad. I have been taught to pursue the dream with all my strength and energy. Without your support and encouragement, I would never finish my doctorate study.

I would also like to thank Prof. Benjamin J. Eggleton for giving me such a great opportunity to pursue a doctor degree in the University of Sydney. I still remember the day I received the invitation letter, I was so excited and yelling loudly. During last four years, you taught me the right way and attitude to solve problems. My postgraduate scholarship is also funded by your project. Without your sponsorship, my Ph.D. study would not be so grateful and fruitful. I am so proud of being a member of CUDOS, which is surrounded by a group of brilliant and friendly people. It is such a stimulating environment to do top-notch research. Thank you, Ben, for giving me such a great opportunity.

I would also like to thank my co-supervisors, Dr. Chunle Xiong and Dr. Bryn A. Bell. My Ph.D. journey can be separated into two parts. From 2014 to 2016, I was mainly supervised by Dr. Chunle Xiong. I did not expect my co-supervisor such a knowledgeable and patient man. At very beginning, I nearly knew nothing about quantum optics, however, Chunle not only taught me the knowledge of quantum optics and nonlinear optics, but also the experimental skills which would take years of experience to obtain. He also inspired me to solve the problems independently and creatively. We have worked together and published several important papers over the past two years. In 2016, Chunle left for a new position in the Australian National University and Bryn became my co-supervisor. I am so honoured to work with Bryn. He is one of the most brilliant persons I had ever known. I was completely astonished by his knowledge and wisdom. Every time we discussed the experiment issues, he can directly point out the problem and offer several solutions to address it. I still remember the time when I was characterising an unbalanced interferometer in our silicon nitride entanglement circuits. I did not notice the asymmetric output of the unbalanced interferometer. He not merely pointed out the problem, but also suggested a new approach to generate identical outputs. Chunle and Bryn, thank you so much for supervising and supporting me over the last four years.

Deeply, I feel so privileged to work in such a fantastic group. I would like to thank our collaborators and my lab mates, Prof. Philip H. W. Leong, Prof. Zhengyu Liu, Dr. Andri Mahendra, Dr. Yeehui Lee, Dr. Eric Magi, Dr. Jiakun He, Mr. Iman Jizan, and Mr. Runyu Jiang. We worked together for so many important works, such as temporal multiplexing, relative multiplexing, and entanglement circuits. Everyone above in this group was dedicated to the project and we even worked until the midnight during the weekend. I am so honoured to have your support.

I would also like to say thank you to my office mates, Mr. Yang Liu, Dr. Blair Morrison, Dr. Moritz Merklein, Miss Atiyeh Zarifi, Dr. Loris Marini, Dr. Caitlin

Fisher, Dr Haishu Li, Dr. Hengyun Jiang and Miss Yuchen Zhao. Our happiest moments are engraved in my mind. Wish you all the best, my dearest friends. I would also like to extend my appreciation to the CUDOS supporting team, including Shelley Martin, Vera Brinkel, Silke Weiss, Joseph Zhang and Simone Kingston.

Last but not least, I want to express my special thanks to my soul mate, Miss Tingjuan Hu who is my wife now. Thank you so much for your consistent accompany. Your smile and encouragement eliminate the frowns from my face. I am so excited about the new phase of our life.

Abstract

Classical computing is insufficient to solve specific problems which have exponentially increased complexity with the problem scale. Meanwhile, in practical circumstance, classical communication cannot guarantee unconditional information security as it relies on computational complexity. Quantum technologies that harness the fundamental laws of quantum physics open the possibility of developing quantum computing and communication that could show unprecedented computational power on specific problems and unconditional information security, respectively. One of the leading approaches involves photonic quantum technologies that encode the information onto single photons. However, the lack of high-efficiency single-photon sources is the major hurdle to demonstrate the quantum advantages of photonic quantum computing over classical computing. Meanwhile, to build a scalable, robust and cost-efficient quantum network, the quantum node requires integrated photonic circuits that can generate, manipulate and analyse entanglement states in a single chip. One of the most promising solutions is integrated time-bin entanglement chips. However, such an integrated chip has not yet been demonstrated. The potential solutions to develop a high-efficiency single-photon source and an integrated time-bin entanglement chip are clearly explained in this thesis.

Chapter 1 provides a brief overview that explains the theme of each chapter. Chapter 2 emphasises the importance of a high-efficiency single-photon source and an integrated time-bin entanglement chip, after explaining the advantages of photonic quantum computing and communication over their classical counterparts. In Chapter 3, three different temporal multiplexing schemes are experimentally demonstrated as the potential solutions to build a high-efficiency single-photon source that can emit highly indistinguishable single photons. Chapter 3 also identifies the potential limitations of temporal multiplexing with high repetition rate. In Chapter 4, the linear processing circuits and nonlinear photon source are separately demonstrated in a low-loss double-stripe silicon nitride waveguide. In the final section of Chapter 4, an integrated silicon nitride time-bin entanglement chip that combines linear processing circuits and nonlinear photon sources is demonstrated as a potential solution to build a robust, scalable and cost-efficient quantum network in the real world. After a succinct summarisation, the final chapter briefly discusses the promising strategies and platforms to build an integrated high-efficiency single-photon source and an integrated quantum node with broad bandwidth and long storage time.

Publications included in this thesis

1. Xiang Zhang, Bryn A. Bell, Andri Mahendra, Chunle Xiong, Philip H. W. Leong, and Benjamin J. Eggleton, "Integrated silicon nitride time-bin entanglement circuits," *Optics Letters*, **15**, 3469-3472 (2018).

2. Xiang Zhang, Bryn A. Bell, Mark Pelusi, Jiakun He, Wei Geng, Yunchuan Kong, Philipp Zhang, Chunle Xiong, and Benjamin J. Eggleton, "High repetition rate correlated photon pair generation in integrated silicon nanowires," *Applied Optics* **56**, 8420-8424 (2017).

3. Xiang Zhang, Yeehui Lee, Bryn A. Bell, Philip H. W. Leong, Terry Rudolph, Benjamin J. Eggleton, and Chunle Xiong, "Indistinguishable heralded single photon generation via relative temporal multiplexing of two sources," *Optics Express* **25**, 26067-26075 (2017).

4. Xiang Zhang, Runyu Jiang, Bryn A. Bell, Duk-Yong Choi, Chang Joon Chae, Chunle Xiong, and Benjamin J. Eggleton, "Interfering heralded single photons from two separate silicon nanowires pumped at different wavelengths," *Technologies* **4**, 25 (2016).

5. Xiang Zhang, Yanbing Zhang, Chunle Xiong, and Benjamin J. Eggleton, "Correlated photon pair generation in low-loss double-stripe silicon nitride waveguides," *Journal of Optics* **18**, 074016 (2016).

6. Chunle Xiong, Xiang Zhang, Matthew J. Collins, Andri Mahendra, Luke G. Helt, Michael J. Steel, Duk-Yong Choi, Chang Joon Chae, Philip H. W. Leong, and Benjamin J. Eggleton, "Active temporal multiplexing of indistinguishable heralded single photons," *Nature Communications* **7**, 10853 (2016).

7. Chunle Xiong, Xiang Zhang, Andri Mahendra, Jiakun He, Duk-Yong Choi, Chang Joon Chae, David Marpaung, Arne Leinse, René G. Heideman, Marcel Hoekman, Chris Roeloffzen, Ruud Oldenbeuving, Paul W. L. van Dijk, Caterina Taddei, Philip H. W. Leong, and Benjamin J. Eggleton, "Compact and reconfigurable silicon nitride time-bin entanglement circuit," *Optica* **8**, 724-727 (2015).

8. Xiang. Zhang, Iman Jizan, Jiakun He, Alex S. Clark, Duk-Yong Choi, Chang Joon Chae, Benjamin J. Eggleton, and Chunle Xiong, "Enhancing heralded single-photon rate from a silicon nanowire by time and wavelength division multiplexing pump pulses," *Optics Letters* **40**, 2489-2492 (2015).

List of abbreviations

A Accidental

AKE asymmetric-key encryption

ATM active temporal multiplexing

BS-FWM bragg-scattering four-wave-mixing

C Coincidence

C_{raw} raw coincidence rate

CAR coincidence to accidental ratio

CMOS complementary metal-oxide-semiconductor

CNOT controlled-NOT

CW continuous wave

CZ controlled phase

DPR distributed-phase-reference

DV discrete-variable

EB entanglement-based

EPR Einstein-Podolsky-Rosen

F finesse

FCA free-carrier absorption

FMUX frequency multiplexing

FSR free spectral range

FWHM full-width at half maximum

FWM four-wave mixing

GVD group velocity dispersion

HBT Hanbury Brown and Twiss

HOM Hong-Ou-Mandel

KLM Knill-Laflamme-Milburn

MUX multiplexing

NA numerical aperture

NS nonlinear sign

***N*-photon** *N* single photons

PIC photonic integrated circuit

PM prepare and measure

QD quantum dot

qubit quantum bit

QKD quantum key distribution

QST quantum state tomography

RSA Ron Rivest, Adi Shamir and Leonard Adleman

RTM relative temporal multiplexing

RMUX relative multiplexing

SEM scanning electron microscope

SFWM spontaneous four-wave mixing

SHG second harmonic generation

SKE symmetric-key encryption

SMUX spatial multiplexing

Si_3N_4 silicon nitride

SNR signal to noise ratio

SOI silicon-on-insulator

SPDC spontaneous parametric down conversion

SPM self-phase modulation

SpRS spontaneous Raman scattering

SRS stimulated Raman scattering

SSB single side-band

STM standard temporal multiplexing

TE transverse electronic

TMUX temporal multiplexing

TM transverse magnetic

TPA two-photon absorption

TWDM time and wavelength division multiplexing

XPM cross-phase modulation

Contents

Chapter 1

Introduction

This chapter explains the structure of the thesis and the themes of each chapter.

Chapter 2 includes four sections. The first section explains the concept of the single photon, as well as its non-classical properties that underpin photonic quantum technologies. In the second section, after explaining the origin of the intractable computing problem, photonic quantum computing is indicated as a potential solution. The development of photonic quantum computing is explained with emphasis on nonlinear and linear schemes. The formidable challenge of achieving π phase in a nonlinear scheme is circumvented by using a particular projective measurement in the linear scheme. We then review the experimental progress over the last two decades, identifying that the bottleneck in the linear scheme derives from the lack of high-efficiency single-photon sources that can generate indistinguishable single photons. In the third section, after explaining the conditional information security in classical communication, quantum communication is emphasised as a promising solution because it allows unconditional information security. The two most well-known quantum key distribution (QKD) protocols—prepare and measure (PM) and entanglement-based (EB) protocol—are defined as short-term and long-term strategies for a global-scale quantum communication network. One of the major hurdles in the entanglement scheme is identified as an integrated photonic circuit with reconfigurable elements that can generate, manipulate and analyse time-bin entangled photons. Moreover, the final section of this chapter reviews two complementary metal-oxide-semiconductor (CMOS) compatible platforms, silicon and silicon nitride, as these two platforms are used to build photon sources and linear processing circuits in the following chapters.

Chapter 3 begins with an explanation of multiplexing schemes with emphasis on the temporal multiplexing scheme, which is indicated as a more resource-efficient approach than the spatial multiplexing scheme. Three temporal multiplexing schemes are proposed and experimentally demonstrated in the Chapter 3. The proof-of-concept results of active temporal multiplexing and time and wavelength division multiplexing schemes indicate that the single-photon generation efficiency can be significantly enhanced to satisfy the threshold of the aforementioned linear scheme. For N single photons (N-photon) generation, which is the basic requirement of photonic quantum computing, theoretical analysis indicates that the relative temporal multiplexing scheme can significantly enhance the N-photon generation probability. The proof-of-principle results confirm the theoretical analysis that N-photon generation efficiency is enhanced with the number

of single-photon sources being multiplexed together, without increasing the complexity. Besides the different multiplexing schemes that are discussed, the potential limitations of temporal multiplexing with high repetition rate are included in the discussion at the end of this chapter, since the temporal multiplexing scheme relies on the correct temporal information.

Chpater 4 emphasises the concept of time-bin entanglement and the importance of integrated photonic circuits in the context of fibre-based QKD. A comprehensive explanation indicates that the key building block of a quantum network is integrated photonic circuits that offer stability for time-bin entanglement state generation and analysis, and meanwhile allow scalability for more complicated extensions, such as quantum memory and single-photon wavelength conversion. The entanglement state analysis circuits are designed and fabricated based on a low-loss double-stripe silicon nitride waveguide structure, and illustrated with a photon interference measurement. The nonlinear property of the low-loss double-stripe silicon nitride waveguide is characterised via coincidence measurements. The nonlinear characterisation indicates that the double-stripe silicon nitride waveguide is a viable structure for both linear and nonlinear components. The final section presents the quantum state tomography results of integrated silicon nitride time-bin entanglement circuits that include nonlinear pair generation, noise suppression, wavelength division and entanglement analysis in a single photonic chip. The negligible discrepancy of the quantum state tomography result between two identical circuits on the same photonic chip verifies the repeatability of this CMOS-compatible platform.

Chapter 5 includes three sections. The first section summarises the proof-of-principle demonstrations of three temporal multiplexing schemes and an integrated time-bin entanglement chip. Future works of building an integrated high-efficiency single-photon source and integrated quantum node are separately discussed in two sections. Based on the experimental progress over the last decades, further improvements are required in optical switching, transmission and detection to achieve an integrated high-efficiency single-photon source. In the section on the integrated quantum node, another two important functionalities—quantum memory and single-photon wavelength conversion—are expected to be integrated with entanglement circuits to allow remote key distribution via an ultra-high bandwidth quantum network. Any improvements in these aspects will take a crucial step towards a practical quantum system.

Appendix presents the supplementary information for active temporal multiplexing and the second time-bin entanglement circuits.

Chapter 2

Background

Chapter 2 includes four sections. The single photon and its non-classical properties, which underpin photonic quantum technologies, are explained in the first section. In the second section, intractable computing problems emphasise the importance of quantum computing, as well as the major hurdle of large-scale photonic quantum computing. In the third section, the conditional information security in classical communication indicates the importance of quantum communication that allows unconditional information security. One of the major hurdles of building a practical quantum network is also explained in the third section. Two CMOS-compatible platforms for integrated quantum optics—silicon and silicon nitride (Si_3N_4)—are separately explained in the final section.

In this thesis, photonic quantum technologies mainly refer to photonic quantum computing and communication. Moreover, photonic quantum technologies are only discussed in the discrete-variable (DV) regime where qubits are encoded onto single photons.

2.1 The single photon and its non-classical properties

2.1.1 Single photons

In the nineteenth century, the wave nature of light was experimentally verified by several canonical works. The most notable work is Thomas Young's double-slit experiment in 1803, which demonstrated an interference of two optical waves. In 1865, James Clerk Maxwell took a historical step forwards by proposing the light is an electromagnetic wave [1]. Its propagation can be described by four equations, as follows:

$$\nabla \cdot \vec{E} = \frac{\rho}{\varepsilon_0}, \tag{2.1}$$

$$\nabla \cdot \vec{B} = 0, \tag{2.2}$$

$$\nabla \times \vec{E} = -\frac{\partial \vec{B}}{\partial t}, \tag{2.3}$$

$$\nabla \times \vec{B} = \mu_0(\vec{J} + \varepsilon_0 \frac{\partial \vec{E}}{\partial t}), \tag{2.4}$$

where $\vec{E}$ is the electrical field, $\vec{B}$ is the magnetic field and $\vec{J}$ and ρ are the free current and charge density, respectively. These four invaluable equations are named Maxwell's equations, and form the foundation of classical optics.

However, near the end of the nineteenth century, the emission spectrum of a blackbody indicated the incompleteness of classical optics, as it presented an unphysical prediction that a black body would emit infinite energy at higher frequency. In 1900, the aforementioned anomaly was solved by Max Planck, who proposed the concept of 'quantised energy levels'. The central assumptions behind his proposal implied that electromagnetic energy could be a multiple of an elementary unit:

$$E = h\nu, \tag{2.5}$$

where h and ν are the Planck's constant ($h = 6.67^{-34} Js$) and the frequency of the electromagnetic wave, respectively. Meanwhile, his proposal also implied that the occupation of each energy mode follows the Bose-Einstein distribution:

$$N_{BE} = \frac{1}{e^{\frac{h\nu}{k_B T}} - 1}, \tag{2.6}$$

where k_B and T are the Boltzmann constant ($k_B = 1.38^{-23} J/K$) and the temperature of the blackbody, respectively. The theoretical analysis predicted by the Planck theorem was consistent with the experimental data at the time. This heuristic work catalysed the study of single photons, as well as the quantum mechanics. Following Planck's quantised solution, in 1905, Albert Einstein successfully explained the photo-electric effect by quantising light into indivisible packets, which were later known as—'single photons' [2]. However, Einstein's

explanation of single photons was quite controversial because of the contradiction between the quantised energy and Maxwell's equations. Most scientists did not accept that light itself is indeed quantised until Arthur H. Compton observed the scattering of single photons by electrons in 1923 [3].

Nowadays, the photon plays an essential role in society, and photonic quantum technologies that harness the non-classical properties of single photons will have a profound effect on our society in the short-term future. The non-classical properties of single photons are briefly explained in Section 2.1.2.

2.1.2 Non-classical properties of the single photon

This section introduces the non-classical properties of the single photon, which will be used in later sections and chapters.

Anti-bunching

Anti-bunching defines a non-classical phenomenon in which more than one photon is unlikely to arrive within a specific time interval. In a more general scenario, when an electron drops down from an excited state to a low state, the energy difference between these two states is converted into one photon. A second photon cannot be emitted until the electron is loaded back to the excited state. The loading process is not instantaneous, so that it defines the time interval (T), which only allows one photon to exist.

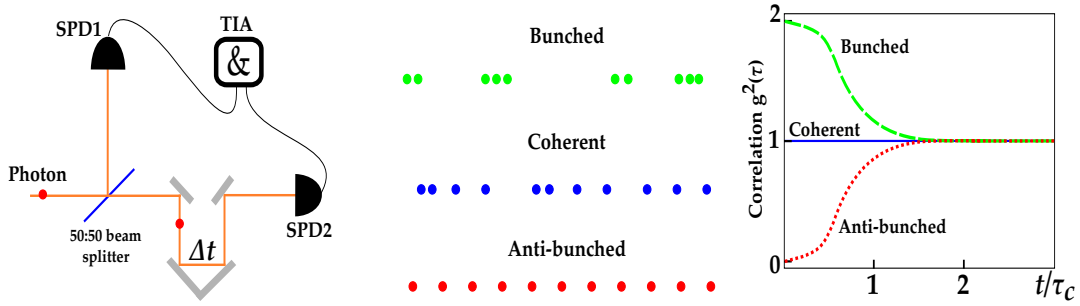

FIGURE 2.1: (a) Illustration of a Hanbury Brown and Twiss (HBT) experiment to measure photon number correlations, $g^{(2)}(\tau)$. SPD: single-photon detector; Δt: adjusted time delay; TIA: time interval analyser. (b) $g^{(2)}(0) = 2$ for a bunched source; $g^2(0) = 1$ for a coherent source; and $g^{(2)}(0) = 0$ for an anti-bunched source. (c) $g^{(2)}(\tau) \to 1$ after a time longer than the coherence length, τ_c.

The anti-bunching phenomenon is verified by a HBT interferometer, as shown in Figure 2.1(a) [4]. A 50:50 beam splitter splits photons between two single-photon detectors (SPD1 and SPD2) connected to a time interval analyser (TIA), which measures the time interval, τ, between consecutive detections. The HBT interferometer is designed to measure the second-order correlation, $g^{(2)}(\tau)$, which can be expressed as:

$$g^{(2)}(\tau) = \frac{\langle n_1(t) n_2(t+\tau) \rangle}{\langle n_1(t) \rangle \langle n_2(t+\tau) \rangle}, \tag{2.7}$$

where $\langle n_1(t) \rangle$ and $\langle n_2(t+\tau) \rangle$ represent the photon number detected by SPD1 and SPD2 at the moment of t and $t+\tau$, respectively. $\langle n_1(t) n_2(t+\tau) \rangle$ represents the coincidence count between SPD1 and SPD2. For a single-photon source shown in Figure 2.1(b), no coincidences are detected when $\tau < T$ and $g^{(2)}(0)$ is 0, as shown in Figure 2.1(c). Besides the anti-bunched photon source, photons can also be bunched together, where each photon arrives randomly and independently of the other photons. A thermal state shows bunching of photons, and its $g^{(2)}(\tau)$ varies from 2 to 1, as shown in Figure 2.1(b) and Figure 2.1(c), respectively. A coherent source, such as a laser, shows Poisson photon statistics and its $g^{(2)}(\tau)$ is constant at 1, as shown in Figure 2.1(b) and Figure 2.1(c), respectively.

Although single-photon detection does not provide sufficient experimental evidence for the existence of a single quanta of light, a measurement of $g^{(2)}(0) = 0$ is a strong piece of evidence for quantised light. The $g^{(2)}(\tau)$ measurement has been widely used to characterise the single-photon purity of the quantum light source [5–8].

Hong-Ou-Mandel quantum interference

Hong-Ou-Mandel (HOM) quantum interference is a non-classical effect occurring between two indistinguishable single photons. This effect was first demonstrated by Chun Ki Hong, Zhe Yu Ou and Leonard Mandel in 1987 [9], and this counter-intuitive effect became a crucial element of photonic quantum computing [10]. Two indistinguishable single photons indicate that they are identical with each other in all degrees of freedom, such as the spectral, spatial, temporal and polarisation domains. The schematic of the HOM quantum interference is illustrated in Figure 2.2(a). Two photons are injected into a 50:50 beam splitter from two separate directions. The coincidences between single-photon detector1 (SPD1) and detector2 (SPD2) are collected by a time interval analyser (TIA). A time delay device precisely adjusts the arrival time of one photon, so that these two photons can interfere with each other at the 50:50 beam splitter.

For indistinguishable photons, there are four possible outcomes with the same probability, as shown in Figure 2.2(b): (I) both photons (red circles) are transmitted through a 50:50 beam splitter; (II) both photons are reflected by a 50:50 beam splitter; (III) and (IV) two photons are paired off a 50:50 beam splitter in either c or d output. However, if two indistinguishable photons interfere with each other at 50:50 beam splitter, only (III) and (IV) will exist, instead of four outcomes. The absence of (I) and (II) derives from a destructive interference between two indistinguishable single photons. A mathematical description of the HOM interference is explained in the following paragraphs.

Initially, two indistinguishable single photons are injected into the 50:50 beam splitter from the input ports a and b, respectively. These two input ports represent two optical modes that carry annihilation and creation operators. In mode a, $\hat{a}$ and $\hat{a}^\dagger$ represent annihilation and creation operators, respectively, similar for

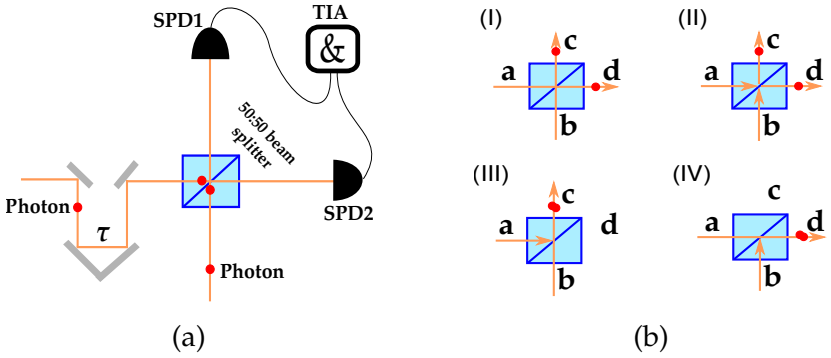

FIGURE 2.2: (a)Illustration of a HOM quantum interference experiment. SPD: single-photon detector; τ: adjusted time delay; TIA: time interval analyser. (b) Four possible outcomes; a, b, c and d represent two inputs and two outputs, respectively.

mode b. The Fock state is used to describe two indistinguishable photons in different modes:

$$\hat{a}^\dagger \hat{b}^\dagger \left|0,0\right\rangle_{ab} = \left|1,1\right\rangle_{ab}, \tag{2.8}$$

where $|0\rangle$ and $|1\rangle$ represent zero and single-photon states, respectively. After the 50:50 beam splitter shown in Figure 2.2(b), modes a and b are converted into another two modes, c and d. The corresponding operator transformation can be expressed as follows:

$$\hat{a}^\dagger = \frac{\hat{c}^\dagger + \hat{d}^\dagger}{\sqrt{2}} \quad \text{and} \quad \hat{b}^\dagger = \frac{\hat{c}^\dagger - \hat{d}^\dagger}{\sqrt{2}}. \tag{2.9}$$

The minus sign is introduced by a unitary transformation from 50:50 beam splitter. Physically, it means that a reflected mode induces a relative phase shift of π with respect to the reflection from the other side of the 50:50 beam splitter. Therefore, the output mode after the 50:50 beam splitter can be expressed as:

$$\begin{aligned} \hat{a}^\dagger \hat{b}^\dagger \left|0,0\right\rangle_{ab} &\rightarrow \frac{1}{2}(\hat{c}^\dagger + \hat{d}^\dagger)(\hat{c}^\dagger - \hat{d}^\dagger)\left|0,0\right\rangle_{cd} \\ &= \frac{\hat{c}^{\dagger 2} + \hat{d}^\dagger \hat{c}^\dagger - \hat{c}^\dagger \hat{d}^\dagger - \hat{d}^{\dagger 2}}{2} \\ &= \frac{1}{2}(\hat{c}^{\dagger 2} - \hat{d}^{\dagger 2})\left|0,0\right\rangle_{cd} \\ &= \frac{\left|2,0\right\rangle_{cd} - \left|0,2\right\rangle_{cd}}{\sqrt{2}}. \end{aligned} \tag{2.10}$$

Two indistinguishable single photons and the relative π phase difference result in a destructive interference between $\hat{c}^\dagger \hat{d}^\dagger$ and $\hat{d}^\dagger \hat{c}^\dagger$. Therefore, the final optical modes indicate that two indistinguishable photons pair off either the output c or d.

Figure 2.3 presents the first experimental verification of HOM quantum interference [9]. The arrival time of one photon is controlled by the position of a beam splitter. When two photons interfere with each other in a 50:50 beam splitter, the

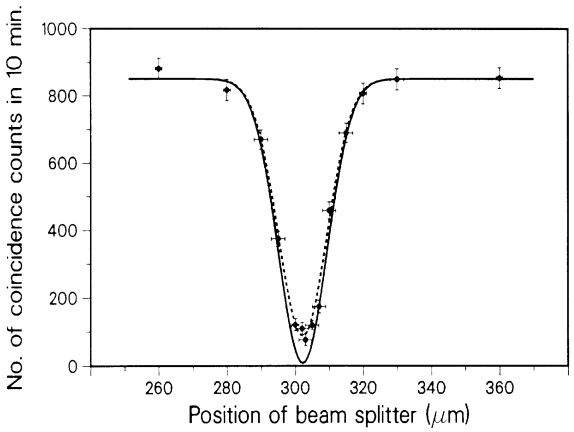

FIGURE 2.3: The first experimental results of HOM quantum interference.

coincidence counts will dramatically decrease, since two photons pair off, as in the dip shown in Figure 2.3. HOM quantum interference has been widely used to rigorously verify single photons' indistinguishability. A visibility equation has been developed to characterise the indistinguishability mathematically, and can be expressed as:

$$Visibility = \frac{C_{max} - C_{min}}{C_{max}} \tag{2.11}$$

C_{max} and C_{min} represent the coincidence count outside the dip and the minimal count inside the dip, respectively. The theoretical values of HOM quantum interference and the classical limitation are 100% and 50%, respectively.

Superposition and entanglement

Superposition state is a non-classical state in which a single photon exists in multiple states simultaneously. A general description of two states is written as follows:

$$|\psi\rangle = \alpha\,|0\rangle + \beta\,|1\rangle\,. \tag{2.12}$$

α and β are complex numbers and amplitudes for the state of $|0\rangle$ and $|1\rangle$ in $|\psi\rangle$. The photon state can be illustrated by a vector pointing to the surface of the Bloch sphere, as $|\psi\rangle$ in Figure 2.4. Here, $|1\rangle$ and $|0\rangle$ in Figure 2.4 represent two orthogonal quantum states.

When the consideration extends from one photon to multiple photons (≥ 2), a counterintuitive phenomenon appears as a '*spooky action at distance*'. This phenomenon is named 'entanglement', and was originally called '*Verschränkung*' by Schrödinger. Entanglement shows a non-classical correlation between multiple photons. The entire state of entangled photons cannot be factored as a product state of each single photon. For instance, two entangled photons can be prepared in a state as:

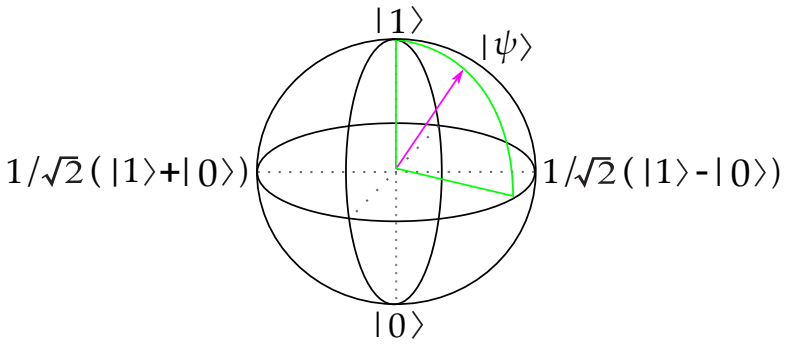

FIGURE 2.4: The Bloch sphere. $|1\rangle$ and $|0\rangle$ represent two orthogonal states. $|\psi\rangle$ represents a superposition state.

$$|\phi^+\rangle = \frac{|11\rangle + |00\rangle}{\sqrt{2}}, \tag{2.13}$$

where $|11\rangle \equiv |1\rangle_1 |1\rangle_2$ and $|00\rangle \equiv |0\rangle_1 |0\rangle_2$ represent the states of two entangled photons. $|\phi^+\rangle$ indicates that the entangled photons are an inseparable entity, rather than a summation of individual photons. There is a basis of four maximally entangled states, called 'bell states', and their mathematic descriptions are as follows:

$$|\phi^+\rangle = \frac{|11\rangle + |00\rangle}{\sqrt{2}}, \quad \text{and} \quad |\phi^-\rangle = \frac{|11\rangle - |00\rangle}{\sqrt{2}}, \tag{2.14}$$

$$|\psi^+\rangle = \frac{|10\rangle + |01\rangle}{\sqrt{2}}, \quad \text{and} \quad |\psi^-\rangle = \frac{|10\rangle - |01\rangle}{\sqrt{2}}. \tag{2.15}$$

Bell states play an essential role in photonic quantum technologies, particularly in photonic quantum communication, because a projective measurement of bell states—known as bell state measurement (BSM)—creates maximal entanglement between two independent photons. To date, entanglement states have been demonstrated in different degrees of freedom, such as polarisation, path, frequency and time-bin [11–15]. Among these well-defined degrees of freedoms, the time-bin entanglement state is a promising option for a fibre-based quantum network. A more specific definition of time-bin entanglement will be explained in Section 4.1.

No-cloning theorem

The no-cloning theorem is the foundation of photonic quantum communication, as it states that perfectly copying an unknown quantum state by a copy machine is impossible. Suppose there are two photons—one photon is in an unknown quantum state $|\psi\rangle$ and the other photon is in a well-defined state, such as $|1\rangle$. A perfect copy machine would transfer the initial quantum state $|1\rangle$ into an unknown state $|\psi\rangle$:

$$|\psi\rangle |1\rangle \xrightarrow{\text{copy}} |\psi\rangle |\psi\rangle . \tag{2.16}$$

The unknown state $|\psi\rangle$ exists in two orthogonal states, $|1\rangle$ and $|0\rangle$, simultaneously, and the basic operation of a copy machine is:

$$|1\rangle|1\rangle \xrightarrow{\text{copy}} |1\rangle|1\rangle, \quad \text{and} \quad |0\rangle|1\rangle \xrightarrow{\text{copy}} |0\rangle|0\rangle. \tag{2.17}$$

When an unknown state $|\psi\rangle = (\alpha|1\rangle + \beta|0\rangle)$ is sent into such a copy machine:

$$|\psi\rangle|1\rangle = (\alpha|1\rangle + \beta|0\rangle)|1\rangle \xrightarrow{\text{copy}} \alpha|1\rangle|1\rangle + \beta|0\rangle|0\rangle. \tag{2.18}$$

However, the right state after a perfect copy is:

$$\begin{aligned} |\psi\rangle|1\rangle \xrightarrow{\text{copy}} |\psi\rangle|\psi\rangle &= (\alpha|1\rangle + \beta|0\rangle)(\alpha|1\rangle + \beta|0\rangle) \\ &= \alpha^2|1\rangle|1\rangle + \beta\alpha|0\rangle|1\rangle + \alpha\beta|1\rangle|0\rangle + \beta^2|0\rangle|0\rangle. \end{aligned} \tag{2.19}$$

The difference between Equation (2.18) and Equation (2.19) explicitly explains that copying an unknown state is an impossible task. Thanks to the no-cloning theorem, quantum communication allows unconditional information security, since an eavesdropper cannot perfectly copy an unknown quantum state.

2.2 Photonic quantum computing

This section first explains intractable computing problems in classical computing. As a potential solution, a general discussion of quantum computing is transferred into a specific solution—photonic quantum computing. After explaining the difficulties of a nonlinear scheme, a linear scheme is discussed as a more promising strategy. The major hurdle of large-scale photonic quantum computing is emphasised as the lack of a high-efficiency single-photon source.

2.2.1 Intractable computing problems

Back in 1947, the first transistor was invented by William Shockley, John Bardeen and Walter Brattain, three brilliant scientists at Bell Laboratories, as shown in Figure 2.5(a). This rudimentary prototype is one of the most significant inventions in the twentieth century, as it opened the possibility of integrated circuits and the microprocessor. Thanks to the extraordinary development of semiconductor technologies, the transistor density doubles per 18 months, as predicted by Moore's law. Nowadays, one microprocessor can be integrated with billions of transistors on an area of around 300 mm^2, as shown in Figure 2.5(b). The exponential incrementation of transistor density will be eventually terminated when the feature-scale of each transistor becomes so small that quantum effects play a significant role. To further exploit computational power, 'supercomputers' have been developed, which allow millions of microprocessors to process data simultaneously. For example, IBM's 'Summit' allows 200 petaflops. As a result of the explosive development of the computational power, supercomputers are used for a wide range of computationally intensive tasks in various fields, such

as real-time weather analysis, spacecraft aerodynamic, molecular modelling and real-time navigation.

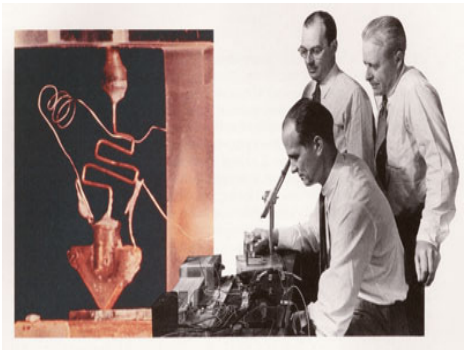

(a)

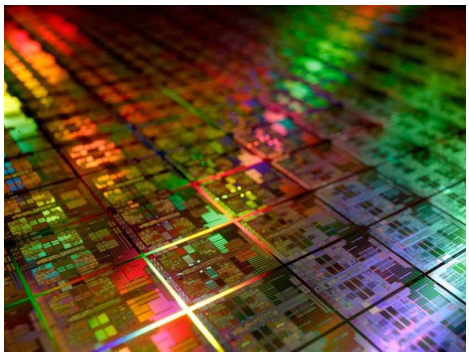

(b)

FIGURE 2.5: (a) First transistor and three inventors: William Shockley (seated), John Bardeen (left) and Walter Brattain (right). (b) Microprocessor on silicon wafer.

The microprocessor and supercomputers explained above are two representative examples of classical computing that use two well-separated regions of a macroscopic system to define each classical bit, for example, 0 and 5 V represent '0' and '1', respectively. More generally, in classical computing, a string of n classical bits could exist in any of 2^n logic states, labelled from '000...0' to '111..1'. The logic states obtained from classical computing offer an incomplete approximation of many problems we would like to understand, such as the universe's evolution and the quantum behaviour of black holes [16, 17]. Moreover, these problems have exponentially increased complexity with the problem scale. Therefore, these problems are intractable computing problems in the sense of requiring an exponentially large amount of memory or operations.

In 1982, a potential solution to address intractable computing problems, including, but not limited to, the aforementioned problems, was discussed in Richard Feynman's famous proposal [18]:

'*Nature isn't classical and if you want to make a simulation of Nature, you better make it quantum mechanical*'.

The first part of this statement indicates the non-classical properties of nature, and the second part indicates a quantum mechanical approach to solve the problem, such as simulating nature. Feynman's proposal catalysed the development of quantum computing both in theoretical and experimental aspects [19–23]. A more general discussion of quantum computing is provided in Section 2.2.2.

2.2.2 Quantum computing

Similar to classical computing, quantum computing can be expressed as a sequence of one- and two-bit operations; however, the intrinsic difference between quantum computing and classical computing lies in the state of each bit and inseparable correlation—entanglement—among these bits. In classical computing,

each bit state is unambiguously defined by a macroscopic system, such as voltage, either '1' or '0' as shown in Figure 2.6(a). However, in quantum computing, each quantum bit (qubit) is represented by a microscopic particle, such as an ion, electron and photon, which allows a continuum of intermediate state or 'superposition' states [16]. As explained in Section 2.1.2, this counterintuitive state indicates that each qubit exists in two states, $|0\rangle$ and $|1\rangle$, simultaneously, with a probability of $|\alpha|^2$ and $|\beta|^2$, respectively, as shown in Figure 2.6(b). Figure 2.6 indicates that each qubit represents an entire space, instead of two particular states as in classical computing.

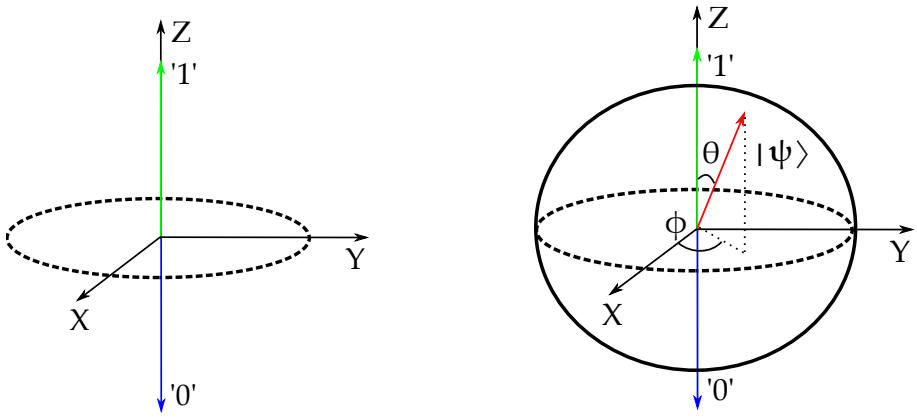

FIGURE 2.6: (a) Classical bit. (b) Qubit in a Bloch sphere. The green, blue and red arrows represent state '1', '0' and $|\psi\rangle$, respectively; θ and ϕ represent the vertical and horizontal angle, respectively.

The quantum state of n qubits can be expressed as

$$\psi = \sum_{n=0\ldots000}^{1\ldots111} c_x |x\rangle , \tag{2.20}$$

where the complex number, c_x, represents the probability amplitude of the corresponding quantum state $|x\rangle$, so that $\sum_x |c_x|^2 = 1$. The 2^n dimensional 'Hilbert space' indicates the advantages of quantum computing over classical computing, which only allows 2^n logic states with n bits.

Another distinct difference between quantum computing and classical computing is the entanglement state, such as $\frac{1}{\sqrt{2}}(|00\rangle + |11\rangle)$, which cannot be separated into the product state of two single qubits, as explained in Section 2.1.2. The computational power of quantum computing exponentially increases with the number of entangled qubits. Moreover, entangled qubits allow parallel operation and processing, so that quantum computing offers exponential or quadratic speed-up on specific problems, such as large integers factorisation, searching problems and many-body simulation [16, 21, 24, 25]. To date, a number of platforms, such as electrons, ions and photons, have been exploited to demonstrate

the advantages of quantum computing. In Section 2.2.3, photonic quantum computing is explained as a prominent candidate.

2.2.3 Photonic solution for quantum computing

During the last three decades, quantum technologies have been demonstrated in different platforms with remarkable progress [23, 26]. Among various platforms, photons are a unique option because they offer a natural interface between quantum computing and quantum communication. The following paragraphs will explain their advantages.

The idea of a 'quantum computer' was first proposed by Richard Feynman in 1982 [18]. In his proposal, he suggested that simulating quantum physics with a classical computer is difficult because of the amount of memory required to store a high-dimensional wave function. Therefore, he proposed a quantum computer as a potential solution. In 1985, D. Deutsch took another important step forwards with a proposal that created the possibility of building a universal quantum computer [27]. Although Deutsch's seminal proposal presented a blueprint of quantum computing, the physical approach to build such a quantum computer was not clear until 2000, when David P. DiVincenzo explicitly proposed a set of criteria to physically implement quantum computing, with two additional criteria of quantum communication [28]. These criteria were as follows:

1. a scalable physical system with well-characterised qubits
2. the ability to initialise the state of the qubits to a simple fiducial state, such as $|000...\rangle$
3. long relevant decoherence times-much longer than the gate operation time
4. a '*universal*' set of quantum gates
5. a qubit-specific measurement capability
6. the ability to interconvert stationary and flying qubits
7. the ability to faithfully transmit flying qubits between specified locations

In 2010, criteria (1) to (5) were rephrased into three general criteria: scalability, universal logic and correctability [23]. A number of platforms have been systematically investigated, such as photons [19, 20, 29–32], trapped ions [33–35], electrons [36, 37], superconducting circuits [38–40] and nuclear magnetic resonance (NMR) [41, 42]. Although trapped ions and superconducting circuits are considered the most likely platforms to demonstrate quantum advantages over classical computing on specific problems, it is too early to claim that these two platforms have a clear edge over other platforms, since quantum computing is still in its infancy.

Single photons—the indivisible quanta of light—have several intrinsic advantages over other candidates, such as being nearly free of thermal and electromagnetic noise and holding a long coherence time [43, 44]. The two-qubit logic gate,

such as the entangling gate, is one major difficulty of photonic quantum computing, since it relies on the nonlinearity between the interaction of two single photons. Fortunately, this major obstacle has been circumvented by the Knill-Laflamme-Milburn (KLM) scheme, which is explained in Section 2.2.5 [10]. Moreover, recent work has demonstrated the advantages of photonic quantum computing over the earliest electronic computers-'ENICA' and 'TRADIC'-that clearly indicate its potential for unprecedented computational power on specific problems [20, 45].

2.2.4 Nonlinear scheme and its technical challenge

The single- and two-qubit operations are the fundamental part of quantum computing, since quantum computation can be expressed as a sequence of one- and two-qubit operations. Suppose each photon qubit is encoded in polarisation, where vertical and horizontal polarisation represent '1' and '0', respectively. Essentially, in a polarisation encoding scheme, single-qubit operation is a quantum state rotation that can be achieved by a phase shifter, beam splitter and wave plate. A two-qubit operation is a logic control, but the control process is heavily reliant on a strong and controllable interaction between single photons. Such a strong interaction is the major difficulty of two-qubit operations because single photons barely interact with each other [46]. One canonical example of two-qubit operation is the controlled phase (CZ) gate. The CZ gate logic is illustrated in Table 2.1.

TABLE 2.1: **The logic of CZ gates.**

Control	Target	Output
$\|0\rangle$	$\|0\rangle$	$\|0,0\rangle$
$\|0\rangle$	$\|1\rangle$	$\|0,1\rangle$
$\|1\rangle$	$\|0\rangle$	$\|1,0\rangle$
$\|1\rangle$	$\|1\rangle$	-$\|1,1\rangle$

Table 2.1 indicates that when the control and target photon are in state $|1\rangle$ and $|1\rangle$, respectively, a π phase shift is imparted on the $|1,1\rangle$ state after the CZ gate. One potential approach to impart π phase shift on the two photon qubits is the Kerr nonlinear effect, such as cross-phase modulation (XPM). The XPM effect can be described by the Hamiltonian as:

$$H_{Kerr} = \kappa \hat{n}_C \hat{n}_T, \tag{2.21}$$

where κ is the Kerr coefficient and $\hat{n}_C$ and $\hat{n}_T$ are the number operators for the control and target qubits, respectively. Equation (2.21) indicates that the phase shift imparted on the target qubit depends on the number of photons in the control qubits.

Figure 2.7 presents a schematic of the CZ gate for two polarisation qubits. The blue rectangle is a polarising beam-splitter that transmits the horizontal polarised photons and reflects vertical polarised photons. The green rectangle represents a Kerr nonlinear medium. When the photons in paths a and b are both vertical polarised, these two photons will interact with each other in the nonlinear

medium to generate a phase shift. Theoretically, a CZ gate could be built if the cross-Kerr nonlinearity is strong enough to introduce π phase shift between two single photons. However, it is too challenging to experimentally demonstrate π phase shift because the cross-Kerr nonlinearity is extremely weak, despite a significant improvement on χ^3 demonstrated in multiple platforms, such as electromagnetically induced transparent material [47], high-Q and low-loss cavity[48–51], high nonlinear optical fibre [52] and Rydberg atom [53–57]. Further, the non-instantaneous behaviour of cross-Kerr effect and its noisy feature prohibit a high-fidelity quantum gate operation that also hinders the development of nonlinear photonic quantum computing [58].

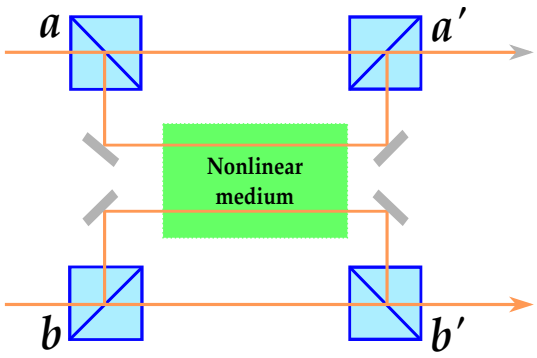

FIGURE 2.7: A Kerr nonlinearity-based CZ gate. The blue and green rectangles are the polarisation beam splitter and Kerr nonlinear medium, respectively.

2.2.5 Linear scheme and its 'Achilles heel'

In a seminal work published in 2001, E. Knill, R. Laflamme and G. J. Milburn proposed a linear scheme that only required single-photon sources, linear circuits and single-photon detectors to build a universal quantum computer[10]. The practical challenge of a π phase shift between two single photons is circumvented by a projective measurement. Figure 2.8 shows a nonlinear sign (NS) gate, where the general input state is taken to be a superposition of photon number terms:

$$|\psi\rangle = \alpha\,|0\rangle + \beta\,|1\rangle + \gamma\,|2\rangle\,. \tag{2.22}$$

Once the ancillary photon is detected at the upper detector and no photons are detected at the lower detector, as shown in the NS gate in Figure 2.8, it heralds a successful NS gate operation where the state $|2\rangle$ is imparted with a π phase shift, as follows:

$$|\psi^{'}\rangle = \alpha\,|0\rangle + \beta\,|1\rangle - \gamma\,|2\rangle\,. \tag{2.23}$$

The maximum probability of a successful NS gate operation can be improved from 1/16 to 1/2 [19, 59]. The matrix information of the NS gate was clearly explained in [10].

Based on the NS gate, a CZ gate can be constructed with HOM quantum interference. The schematic of CZ gate for two polarisation qubits is shown in Figure 2.8. Suppose the horizontal and vertical polarised photons are defined as $|0\rangle$ and $|1\rangle$, respectively. The polarisation beam splitters (blue rectangles) allow a transmission of a horizontal polarised photon and a reflection of a vertical polarised photon. Therefore, when the input states $|\psi\rangle$ are $|00\rangle$, $|10\rangle$ and $|01\rangle$, the output states $|\psi^{'}\rangle$ are exactly the same:

$$|\psi\rangle = |00\rangle \xrightarrow{\hat{U}_{CZ}} |\psi^{'}\rangle = |00\rangle\,, \tag{2.24}$$

$$|\psi\rangle = |01\rangle \xrightarrow{\hat{U}_{CZ}} |\psi^{'}\rangle = |01\rangle\,, \tag{2.25}$$

$$|\psi\rangle = |10\rangle \xrightarrow{\hat{U}_{CZ}} |\psi^{'}\rangle = |10\rangle\,. \tag{2.26}$$

When the input state $|\psi\rangle = |11\rangle$, both photons are in the vertical polarised mode and will be reflected by the polarisation beam splitters. The transformation process can be separated into three steps, as shown in Figure 2.8

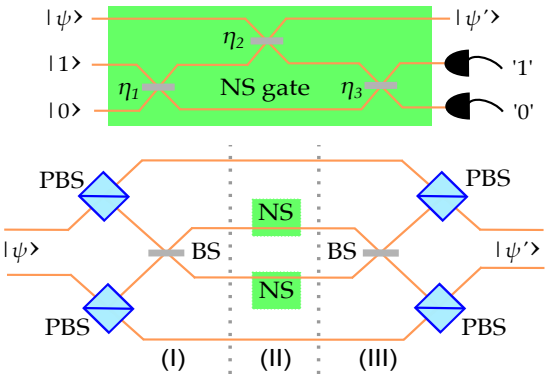

FIGURE 2.8: NS gate and CZ gate. $\eta_1 = \eta_2 = 1/(4-2\sqrt{2})$ and $\eta_3 = 3-2\sqrt{2}$ are the transmission amplitudes of beam splitters. PBS: polarisation beam splitter; BS: 50:50 beam splitter.

Step (I): Two vertical polarised photons interact with each other at beam splitter and pair off together:

$$|\psi\rangle = |11\rangle \xrightarrow{\hat{U}_{BS}} \frac{|20\rangle - |02\rangle}{\sqrt{2}}; \tag{2.27}$$

Step (II): The state of $|20\rangle$ and $|02\rangle$ get π phase shift probabilistically:

$$\frac{|20\rangle - |02\rangle}{\sqrt{2}} \xrightarrow{\hat{U}_{NS}} \frac{-|20\rangle + |02\rangle}{\sqrt{2}}; \tag{2.28}$$

Step (III): A reversed HOM quantum interference occurs between $|20\rangle$ and $|02\rangle$, so that the final output state is imparted with π phase shift:

$$\frac{-|20\rangle + |02\rangle}{\sqrt{2}} \xrightarrow{\hat{U}_{BS}} -|11\rangle = |\psi^{'}\rangle\,; \tag{2.29}$$

Equations (2.27) to (2.29) explain the transformation of state $|11\rangle$ in a CZ gate, and the final state is:

$$|\psi\rangle = |11\rangle \xrightarrow{\hat{U}_{CZ}} |\psi'\rangle = -|11\rangle . \tag{2.30}$$

Beside the projective measurement, the KLM scheme utilizes quantum teleportation to achieve a near deterministic quantum gate. Meanwhile, via quantum coding, it also presents a more resource-efficient scheme compared with previous linear schemes, because the required resources scale at a polynomial rate [10]. Over the last decade, theoretical works and experimental demonstrations clearly indicated the advantages of photonic quantum computing [20, 29–32, 43, 45, 60–63]. However, its potential applications in the real world are severely limited by one building block—the single-photon source, which is the 'Achilles heel' of the entire system.

Three ideal building blocks are required to build a linear photonic quantum computer. The first is a deterministic single-photon source that can generate indistinguishable single photons deterministically. The second building block is lossless linear components (or circuits) that can precisely control the state of single photons. The final building block is a single-photon detector with unity detection efficiency. These three building blocks are plausible from a theoretical perspective. However, to date, none of them achieve the ideal state because of practical barriers, such as inevitable loss, material defects and fabrication limits. In 2008, M. Varnava et al. proposed a highly robust linear scheme that allows efficient quantum computing with imperfect photon sources, linear circuits and single-photon detectors as long as the overall efficiency ≥ 0.67 [64]. The overall efficiency is a product of the single-photon generation, transmission and detection efficiency. Table 2.2 summarises the state-of-the-art of the three building blocks.

TABLE 2.2: **Summary of three building blocks.**

Building block	Platform	Performance
Photon source	Weak coherent laser Quantum dot (QD) Nonlinear source (NLS)	Multi-photon noise (Laser) >MHz (QD) [7, 65] 0.667 efficiency (NLS) [66]
Linear circuit	Bulk optics + free-space Semiconductor circuits	$\approx$ 99% (bulk optics) [67] 0.3 dB/cm (Si) [68] 0.0005dB/cm (Si_3N_4) [69]
Photon detector	Semiconductor detector Superconducting detector	$\geq$ 70% (semiconductor)[70, 71] $\geq$ 90% (superconducting) [72–74]

Table 2.2 shows the promising progress in linear circuits and single-photon detector. Suppose the bulk optical components or integrated photonic circuits are applied for linear quantum state processing, and the quantum states are finally detected by the superconducting single-photon detector, the maximum efficiency from these two blocks is around 0.9. In this context, the generation efficiency of the single-photon source has been reduced to 0.75 (0.67/0.9) instead of near-unity. However, to date, such a high-efficiency single-photon source has not yet

been demonstrated; thus, it is the main obstacle hindering the development of photonic quantum computing, particularly in a large-scale regime.

A single-photon source for photonic quantum technologies is characterised by six aspects:

1. brightness: the detected single-photon rate
2. signal to noise ratio (SNR): useful single photons/noise photons
3. $g^{(2)}(0)$: the indication of single-photon generation
4. indistinguishability: the indication of identical frequency and spatiotemporal mode
5. spatiotemporal mode: only one single photon in a certain spatiotemporal mode
6. spectral flexibility: tunable wavelength

Three approaches are typically used to build a single-photon source: weak coherent light source, 'single-photon emitter' and heralded single-photon source. Depending on the field of applications, the suitable quantum light source varies from one field to the other. In QKD, such as the PM protocol, the weak coherent light source is a suitable source. However, the weak coherent light source is not an appropriate photon source for photonic quantum computing. The other two types of single-photon source are considered a potential solution. The single-photon emitter and heralded single-photon source are explained in the Section 2.2.6 and Section 2.2.7, respectively.

2.2.6 Single-photon emitter

The single-photon emitter is an atom-like system that emits a single photon when the system decays from an excited state to a ground state. The single-photon emitter has been demonstrated in numerous materials or platforms, such as colour centre in crystals, self-assembled quantum dots, two-dimensional materials and carbon nanotubes, as shown in Figure 2.9. A comprehensive review in the field of solid-state single-photon emitter is explained in Ref.[79]

To date, self-assembled InAs/GaAs QD is one of the most promising single-photon emitters for its deterministic single-photon generation, ultra-high single-photon purity ($g^{(2)}(0) < 0.01$), brightness (> MHz detection rate) and indistinguishability ($\geq$ 99%) [7, 76]. Based on the aforementioned InAs/GaAs QD, scalable and high-efficiency boson sampling has experimentally demonstrated the advantages of photonic quantum computing over its classical counterpart [45, 67]. However, such an excellent single-photon emitter is still not an 'ideal' single-photon source because of the imperfect collection system, lack of spectral flexibility and distinguishable photons from separate quantum dots. Although the imperfect collection system and lack of spectral flexibility limit the use of QD, there are feasible solutions, such as boosting the extraction efficiency by large numerical aperture (NA)=0.85 [80, 81], improving the transmission efficiency of

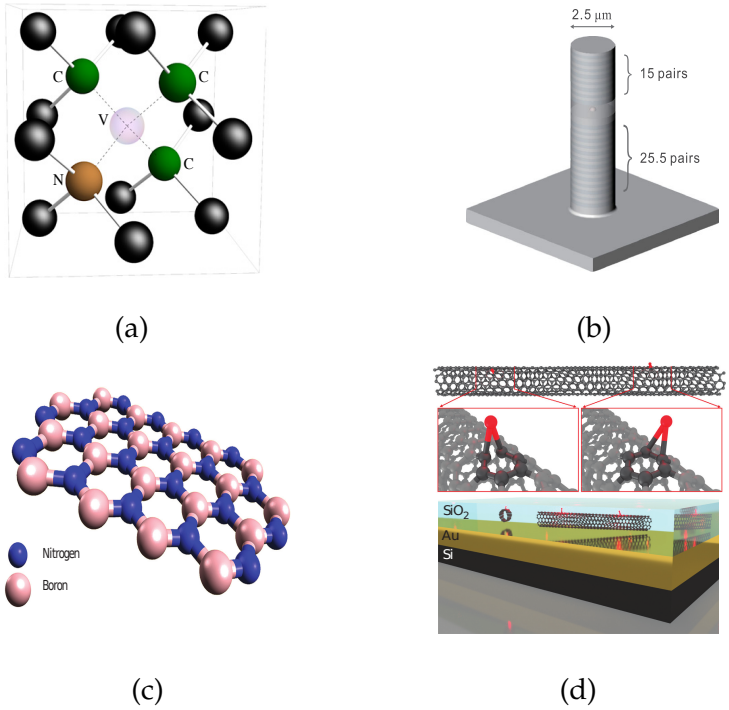

(a) (b)

(c) (d)

FIGURE 2.9: Single-photon emitter. (a) nitrogen-vacancy in diamond [75]. (b) InAs/GaAs QD [76]. (c) Hexagonal boron nitride (hBN) [77]. (d) Carbon nanotubes (CT) [78].

the optical path, and deterministic single-photon wavelength conversion [8, 82]. Indistinguishable photons from different quantum dots is the fundamental challenge since fabricating two identical quantum dots is beyond the state-of-the-art of CMOS fabrication facilities. Electrical tuning [83, 84] or temperature tuning [85] are potential approaches to adjust the emission spectrum of quantum dots, but the limited interference visibility and narrow tuning bandwidth indicate these approaches need further improvements. Demultiplexing the single photons from one QD is an alternative solution; however, it entails a price of lower photon rate and transmission efficiency [45, 67, 86]. The distinguishable issue indicates that the single-photon emitter may not be the best approach to build an 'ideal' or a promising single-photon source for large-scale photonic quantum computing that requires N-photon simultaneously.

2.2.7 Heralded single-photon source

A heralded single-photon source that harnesses stochastic nonlinear optical effects, such as SPDC and SFWM, is another viable approach to build a single-photon source. Unlike the single-photon emission from a single-photon emitter, a heralded single-photon source generates a time-correlated single-photon pair. The detection of one photon (heralding single photon) heralds the existence of the other single photon (heralded single photon). The principles of SPDC and SFWM are shown in Figure 2.10(a) and Figure 2.10(b), respectively.

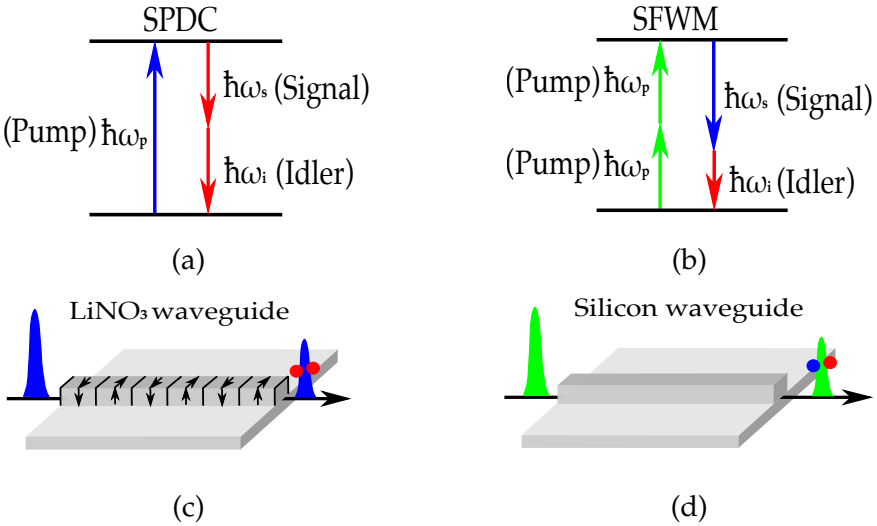

FIGURE 2.10: Principle of SPDC and SFWM. (a) Principle of SPDC. (b) Principle of SFWM. (c) Schematic of SPDC in a lithium niobate waveguide. (d) Schematic of SFWM in a silicon waveguide.

Figure 2.10(a) presents the principle of SPDC in the frequency domain. One pump photon (blue) is probabilistically split into a time-correlated photon pair (red), signal and idler. The energy conservation requires that:

$$\omega_p = \omega_s + \omega_i, \tag{2.31}$$

where ω_p, ω_i and ω_s represent the angular frequency of a pump, ideal and signal photon, respectively. Here, Figure 2.10(a) only depicts one possible SPDC process in which signal and idler have identical frequency ($\omega_s = \omega_i$), but it is sufficient to show the underlying principle. As a reversed second harmonic generation (SHG), the SPDC relies on the second-order nonlinearity ($\chi^{(2)}$), which only exists in a material with non-centre-symmetric lattices, such as lithium niobate [87, 88], β-barium borate (BBO) [89] and potassium-dihydrogen-phosphate (KDP) [90]. The schematic of SPDC in a periodically poled lithium niobate (PPLN) waveguide is depicted in Figure 2.10(c).

Figure 2.10(b) shows the principle of non-degenerate SFWM in the frequency domain. Instead of splitting one pump photon, two pump photons (green) are probabilistically converted into a time-correlated photon pair, signal (blue) and idler (red), with different frequencies ($\omega_s \neq \omega_i$). The degenerate SFWM creates two identical single photons ($\omega_s = \omega_i$) via two different pump wavelengths [91, 92]. SFWM is a third-order ($\chi^{(3)}$) nonlinear process in a quantum regime that is randomly stimulated by the fluctuation of vacuum state. Besides the vacuum state, the occurrence of SFWM is also determined by other two conditions: energy conservation and phase matching. The condition of energy conservation and phase matching can be expressed as:

$$\Delta\omega = \omega_{p1} + \omega_{p2} - \omega_s - \omega_i = 0 \tag{2.32}$$

$$\Delta k = k_s + k_i - k_{p1} - k_{p2} = 0, \tag{2.33}$$

where ω_x and k_x represent the angular frequency and wave-vector, respectively, and $x = p$, s and i represent the pump, signal and idler photons, respectively. The schematic of SFWM in a silicon nanowire is shown in Figure 2.10(d).

As a result of the photon pair generation, a heralded single-photon source is characterised by a coincidence measurement, as shown in Figure 2.11. After a nonlinear waveguide, time-correlated photon pairs are generated and separated into two channels for signal (blue) and idler (red) photons. A time interval analyser (TIA) collects the time-tag information of the signal and ideal photons after the single-photon detector (SPD). The detection of a time-correlated photon pair is illustrated by the orange dashed oval in Figure 2.11, and defined as Coincidence (C). Meanwhile, TIA also collects spurious coincidences, called Accidental (A). These accidentals are contributed by uncorrelated noise photons, as shown by the green dashed oval in Figure 2.11. The uncorrelated noise photon comes from the pump leakage, multi-photon pair, transmission loss, two-photon absorption (TPA), free-carrier absorption (FCA) and spontaneous Raman scattering (SpRS) [93–100].

Figure 2.11 illustrates a histogram of coincidence measurement within 60 s. The detection of time-correlated photon pairs results in an accumulation of C at a certain relative time delay, corresponding to the length difference between signal and idler channels. A significant peak in the histogram manifests the generation of the time-correlated photon pair. In contrast, the uncorrelated noise photons accidentally pair a spurious coincidence, irrespective of the fixed relative time delay, and periodically form small accidental peaks, as shown in Figure 2.11. The constant time interval between each peak is predefined by the periodic temporal mode of pump pulses.

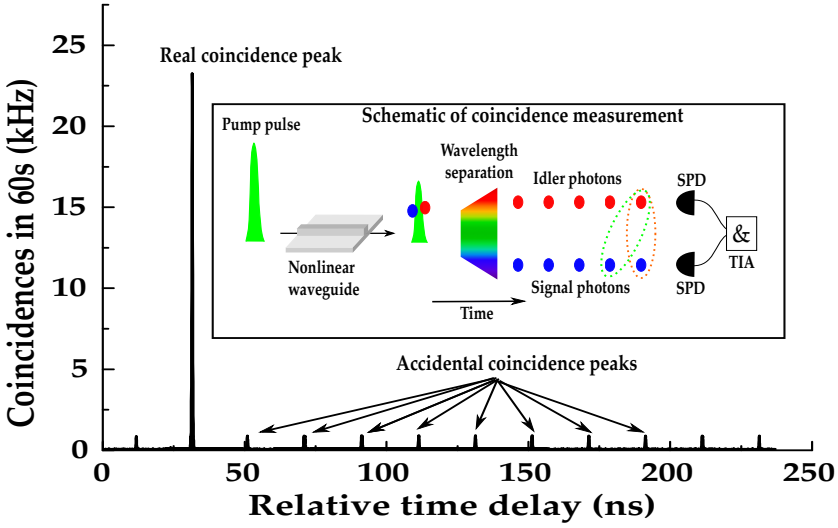

FIGURE 2.11: Histogram of coincidence measurement.

The spurious coincidences (A) immersed inside the coincidences (C) will limit the applications of a heralded single-photon source because of the SNR. As a quantum analogue to the SNR, the coincidence to accidental ratio (CAR) has been developed to characterise the quality of heralded single-photon source which can be expressed as:

$$CAR = \frac{C - A}{A} = \frac{C_{true}}{A}, \tag{2.34}$$

where C_{true} represents the detection of real time-correlated photon pairs after subtracting the spurious detections (A) from the 'raw' coincidence (C). The C_{true} of a heralded single-photon source can be estimated by:

$$C_{true} = \mu\eta_i\eta_s R, \tag{2.35}$$

where μ is the average probability (or efficiency) of generating one photon pair per pulse, and η_i, η_s and R are the overall collection efficiency of the idler and signal channel and pump repetition rate, respectively. Due to the stochastic nonlinear process, there is an uncertainty in C_{true}. Meanwhile, the independent photon generation indicates that the uncertainty can be analysed by the standard deviation of the Poisson distribution (denoted by Poisson error bar hereafter):

$$\sigma = \sqrt{C_{true}} = \sqrt{\mu\eta_i\eta_s R}. \tag{2.36}$$

The accidental rate in Equation (2.34) can be expressed as the product of the detection from each channel:

$$\begin{aligned} A &= (\mu\eta_s + d_s)(\mu\eta_i + d_i)R \\ &= (\mu^2\eta_s\eta_i + \mu\eta_s d_i + \mu\eta_i d_s + d_s d_i)R \end{aligned} \tag{2.37}$$

where, d_s and d_i are dark counts from the single-photon detector. $\mu^2\eta_s\eta_i$ and $d_s d_i$represent the noise counts contributed by multiple photon pairs and dark counts, respectively. $\mu\eta_s d_i$ ($\mu\eta_i d_s$) shows the noise counts contributed by unpaired photons and dark counts. Since most experimental setups have quite low generation probability (μ) and collection efficiency (η_s and η_i), Equation (2.37) is an appropriate approximation to analyse noise counts. After combining Equation (2.35) and Equation (2.37), CAR equals:

$$CAR = \frac{\mu\eta_i\eta_s}{(\mu\eta_s + d_s)(\mu\eta_i + d_i)}. \tag{2.38}$$

In the high count regime, the dark counts (d_s and d_i) play a trivial role in the measurement. Therefore, A can be estimated by $\mu\eta_s\mu\eta_i$, and CAR is simplified to:

$$CAR \approx \frac{\mu\eta_i\eta_s}{\mu\eta_s\mu\eta_i} = \frac{1}{\mu}. \tag{2.39}$$

To date, the heralded single-photon source has been experimentally demonstrated with broadband spectral flexibility [12, 101–103], ultra-high brightness [89, 104], single-photon purity [8, 105, 106] and indistinguishable photon from separate sources [104, 107]. However, the intrinsic limitation of the heralded single-photon source is the probabilistic photon pair generation that fails to satisfy the criterion of a high-efficiency single-photon source ($\mu \geq 0.75$). Increasing the pump power can improve the generation efficiency of a single-photon pair, but the maximum generation efficiency of a single-photon pair is only 0.25

[108]. Fortunately, the multiplexing scheme has been proposed to break the probabilistic nature of a heralded single-photon source by manipulating the heralded single photons in the spatial, temporal or frequency domain via an active switching [109–111]. The proof-of-principle demonstrations indicate that the multiplexing scheme creates the possibility of developing a high-efficiency single-photon source. In Chapter 3, three temporal multiplexing schemes are explained as a potential solution to enhance the generation probability of the heralded single-photon source.

2.3 Photonic quantum communication

This section first explains conditional information security in classical communication. As a potential solution, a general discussion of quantum communication is transferred into a specific solution-photonic quantum communication. After explaining two seminal protocols and two distribution channels, the lack of integrated time-bin entanglement circuits is indicated as one of the major hurdles to build a robust, scalable and cost-efficient quantum network.

2.3.1 Conditional information security

Information security is a long-standing puzzle in the field of communication. Information security is heavily reliant on the encryption scheme, which is the process of encoding plaintext into ciphertext so that it can be accessed by the authorised parties only. The encryption schemes can be classified into two types: symmetric-key encryption (SKE) and asymmetric-key encryption (AKE) schemes.

SKE defines an encoding process in which both the sender and receiver (called Alice and Bob in this example) share identical keys, as shown in Figure 2.12(a). Bob encrypts a plaintext into a ciphertext with a shared key, before sending it to Alice. Alice then decrypts the ciphertext back to the plaintext with the same key. Two representative SKE schemes are data encryption standard (DES) and advanced encryption standard (AES). As a result of the identical key for encryption and decryption, key management becomes extremely difficult, as the required key number equals the square of the communicant number. The practical obstacle of key management in SKE is addressed in AKE (or public-key encryption), which was first proposed by Whitfield Diffie and Martin Hellman in 1976 [112]. Compared with SKE, AKE applies private and public keys for each end-user, as shown in Figure 2.12(b). Bob sends a ciphertext encoded by Alice's public keys to Alice, and then Alice decrypts the ciphertext with her private keys. One of the best-known AKE schemes was proposed by Ron Rivest, Adi Shamir and Leonard Adleman (RSA) [113]. Another two representative AKE schemes are the Diffie-Hellman key exchange [114] and digital signature algorithm (DSA).

Compared with SKE, AKE is a more resource-efficient scheme. The AKE scheme has been widely used in a practical communication network. The information security of AKE relies on the computational complexity, which can be interpreted by a one-way function. By definition, it is straightforward to calculate

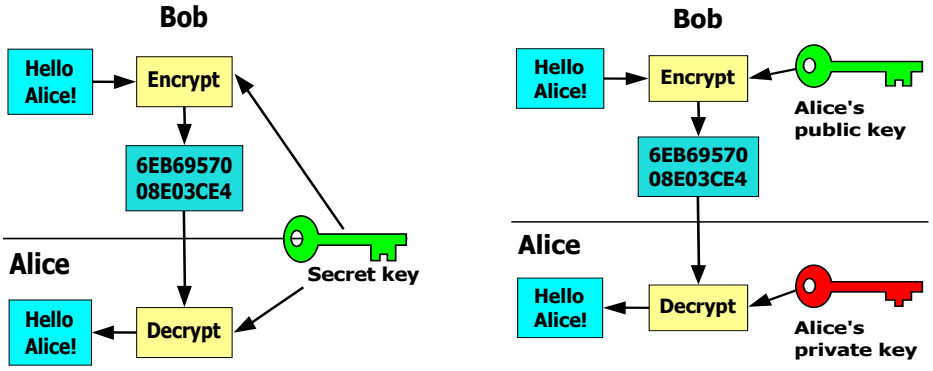

(a) (b)

FIGURE 2.12: (a)SKE scheme; (b) AKE scheme.

$f(x)$ with a given variable, x; however, it is difficult to reverse the calculation and deduce x from $f(x)$ [113, 115]. For instance, it is easy to work out the product of two prime numbers: $67 \times 71 = 4,757$; however, it takes much longer to find the prime factor of 4,757. The computational efforts to break the AKE exponentially increase with the bit number of the public key ($f(x)$). For instance, 2,048 bit public keys take years to factorise into private keys. Therefore, AKE is considered a reliable scheme to prohibit information leakage. However, in theoretical aspects, AKE offers conditional information security because its security depends on an unproven assumption-the nonexistence of an efficient factorisation algorithm in classical computing [115]. Moreover, the theoretical analysis of quantum computing magnifies the flaw of AKE since Shor's algorithm allows efficient factorisation of large integers in quantum computing [21, 116]. Information security is of the utmost importance in current society, and there is zero tolerance for any potential threats. Theoretical analysis and experimental demonstrations suggest that quantum communication is a promising way to achieve unconditional information security [26, 115, 117–120]. A general discussion of quantum communication is presented in Section 2.3.2.

2.3.2 Quantum communication

As explained in Section 2.3.1, classical communication cannot offer unconditional security if someone has a substantial amount of computational power or unanticipated algorithm. Quantum communication allows unconditional information security, as the encryption keys are protected by the law of quantum physics, rather than computational complexity. Here, the unconditional security does not equal 'absolute security', which does not exist. In 2009, V Scarani et al. explicitly clarified the difference between these two terms [121]. The unconditional security of quantum communication holds under several prerequisites:

1. An eavesdropper, Eve, cannot intrude into Alice's and Bob's devices to access either the emerging key or their choices of settings.

2. Alice and Bob must trust the random number generators that select the state to be sent or the measurement to be performed.

3. The classical channel is authenticated with unconditional secure protocols, which exist [122, 123].

4. Eve is limited by the law of quantum physics.

In quantum communication, there are two channels-the quantum and classical channels-between two communicants, as shown in Figure 2.13. The encryption keys are transferred or distributed by the quantum channel, and the classical channel is used to post-select (or sift) identical keys between two communicants. The encryption keys are encoded in the indivisible particles, such as electrons, ions and photons, to prohibit key stealing. Meanwhile, the no-cloning theorem explained in Section 2.1.2 indicates that Eve cannot perfectly copy an unknown quantum state. Although different types of indivisible particles are viable candidates to transfer quantum state from one place to another, single photons are the most practical way to communicate over long distances, as single photons have negligible interference with the environment. Photonic quantum communication is clearly explained in Section 2.3.3.

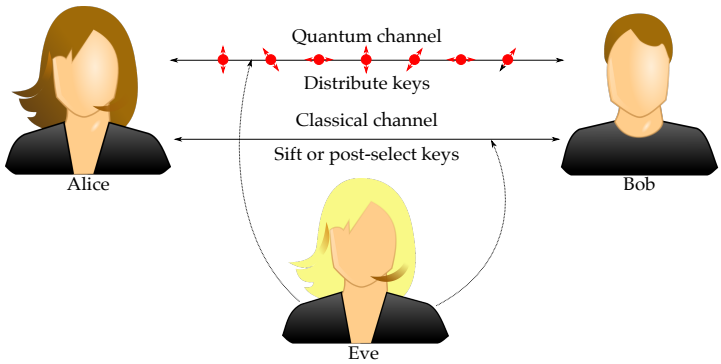

FIGURE 2.13: Schematic of quantum communication. Red circles: single photon with non-orthogonal quantum state (arrow). The dashed lines are the illegitimate channels for eavesdroppers (Eve)

2.3.3 Photonic solution for quantum communication

Transferring a quantum state from one place to another lies at the heart of quantum communication. Single photons are the most promising way to distribute the quantum state over a long distance in the real world. The transmission speed of single photons and the negligible interference with the environment enable the construction of an ultra-high bandwidth quantum network in the real world. There are two canonical protocols of QKD: (I) "prepare and measure" (or called PM) and (II) "entanglement-based" (or EB) [118, 124]. Theoretical works and experimental progress indicate that both the PM and EB protocols offer unconditional information security, but the technical challenges of developing a large-scale quantum network distinguish EB from PM [26, 119, 125]. The PM and EB protocols are explained in Section 2.3.4.

2.3.4 Two seminal protocols

Prepare and measure protocol

In 1984, C. Bennett and G. Brassard presented the first QKD protocol in an IEEE conference in India [124], which became one of best-known PM protocols. We call this the 'BB84' protocol. The PM scheme requires two non-orthogonal bases and four distinct quantum states to encode the photon qubits. To explain the PM protocol, polarisation is selected to encode the quantum state of each photon qubit. Figure 2.14 shows each step of the PM protocol. Suppose Alice plans to send nine-bits encryption key (010101100) and randomly selects two non-orthogonal bases (A and B) to encode photon qubits. Each base includes two orthogonal polarisation states for the binary values of 1 and 0. In Base A:

$$|H\rangle = 0, \quad \text{and} \quad |V\rangle = 1, \tag{2.40}$$

and in Base B:

$$|L\rangle = 0, \quad \text{and} \quad |R\rangle = 1, \tag{2.41}$$

where $|H\rangle$, $|V\rangle$, $|L\rangle$ and $|R\rangle$ represent the horizontal, vertical, left-hand circular and right-hand circular polarisation state, respectively. AAAABBBBA are the selected bases, while the encoded states are HVHVLRRLH, as shown in Figure 2.14. After receiving nine-qubits from Alice, Bob will randomly measure these qubits either in basis A or basis B. Presume he measures the qubit in basis chain ABABBBBAB. The measurement results in Bob's hand are HHHHLRRRV, which correspond to 000001111. Alice and Bob will compare their measurement basis in the classical channel and only retain the bits where their measurement bases agree: 'A - A - B B B - -'. The remaining basis will sift or post-select the secret keys for Alice and Bob: '0 - 0 - 0 1 1 - -' and '-' represent the discarded raw key bits after the post-selection. '00011' are the secret key bits that are only available to Alice and Bob.

Nine bits	**0**	**1**	**0**	**1**	**0**	**1**	**1**	**0**	**0**
Alice's bases	**A**	**A**	**A**	**A**	**B**	**B**	**B**	**B**	**A**
Alice's states	**H**	**V**	**H**	**V**	**L**	**R**	**R**	**L**	**H**
Bob's bases	**A**	**B**	**A**	**B**	**B**	**B**	**B**	**A**	**B**
Bob's states	**H**	**H**	**H**	**H**	**L**	**R**	**R**	**R**	**V**
Bob's bits	**0**	**0**	**0**	**0**	**0**	**1**	**1**	**1**	**1**
After key sifting	**0**	**-**	**0**	**-**	**0**	**1**	**1**	**-**	**-**
Final bits	**00011**								

FIGURE 2.14: Illustration of PM protocol. The red bases are the non-identical bases between Alice and Bob.

The previous paragraphs describe the process of the PM protocol without considering the existence of a potential eavesdropper. Suppose the eavesdropper,

Eve, is monitoring both channels between Alice and Bob, as shown in Figure 2.13, but cannot copy the key information from the quantum channel, because the keys are encoded on single photons and each state exists in two non-orthogonal bases simultaneously, so that Eve cannot deduce the correct state by an orthogonal measurement. In this context, the qubit is completely ambiguous to Eve, and the no-cloning theorem prohibits perfect duplication from the quantum channel. If Eve intercepts these nine photon qubits and resends another nine qubits to Bob, based on her measurement. Alice and Bob will pause further key distribution or abandon this quantum channel because Eve will introduce 25% error rate in the sifted key where Alice and Bob choose the same bases.

Entanglement-based protocol

In 1991, A. K. Ekert independently proposed another QKD protocol-E91 which is one of the best-known EB protocols. Compared with the PM scheme, the EB scheme uses maximally entangled photons, as explained in Section 2.1.2, to distribute the keys, and verifies the information security via Bell's inequality test [118]. Figure 2.15 demonstrates the difference between the PM and EB schemes. In the quantum channel, an Einstein-Podolsky-Rosen (EPR) source emits the entangled photon pairs, with one photon sent to Alice and the other sent to Bob. After receiving their photon qubits, Alice and Bob will randomly select their own measurement bases, either basis A or basis B, and measure their qubits independently. The following processes are similar to the PM scheme, such as comparing the basis in the classical channel and sifting the identical keys. The entangled photon pairs between Alice and Bob allow non-classical correlations. Any illegitimate measurements on these entangled photon pairs will irreversibly modify their correlation. Alice and Bob can identify the existence of eavesdropper through a test of Bell's inequality.

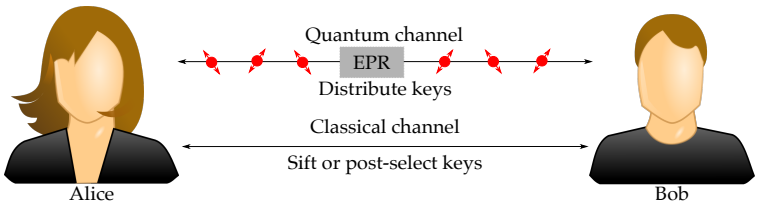

FIGURE 2.15: Schematic of EB protocol. EPR: Einstein-Podolsky-Rosen source generates entangled photons (red circles). The arrows with different directions indicate different quantum states.

In several aspects, the PM and EB schemes are similar with each other. In 1992, C. Bennett, G. Brassard and N. D. Mermin proposed another QKD scheme (called BBM92) to protect information security without a Bell's inequality test [126]. Theoretically, the PM scheme can be translated into the EB scheme:

$$|\phi^n\rangle_{AB} = \frac{1}{\sqrt{d_n}} \sum_{S_n} |S_n\rangle_A \otimes |\phi(S_n)\rangle_B \,. \tag{2.42}$$

where d_n is the number of possible S_n sequences and $|S_n\rangle_A$ form an orthogonal basis. After measuring the basis, $|\psi(S_n)\rangle_B$ is the corresponding quantum state

that Alice sends to Bob [121]. This formal translation does not mean that both schemes are feasible with current technologies. Based on the difficulty of technical requirements, the PM and EB schemes are considered a short-term and long-term (or ultimate) strategies, respectively.

As a short-term strategy, the technical requirements of the PM scheme are not as challenging as the EB scheme. The practical issues of the PM scheme, such as photon-number-splitting and side channel attacks, have been addressed by the decoy states and measurement-device-independent-QKD scheme [125, 127], respectively. The PM scheme has been experimentally demonstrated in optical fibres [128–132] and free-space link [133–138]. To our knowledge, the longest point-to-point fibre and free-space link is 404 km and 1,200 km [130, 136], respectively. More than 2,000 km of fibre-based quantum link has been built with trusted relay nodes that legitimately implement an intercept and resend strategy [139]. Meanwhile, the EB scheme not only offers unconditional information security, but also allows dense coding, quantum teleportation and entanglement purification [140–142]. Beside these advantages, the underlying properties of the EB protocol also present the possibility of a device-independent-QKD [143]. In 2005, G. Brassard presented the following comments on the EB protocol [144]:

'Finally, whenever the long-term storage of quantum information will become feasible, entanglement-based cryptography will provide a form of key distribution that would remain secure not only against eavesdropping, but also against burglary'.

G. Brassard's comments indicate the significance of the EB protocol in quantum communications, yet also indicate that the required technologies (such as quantum memory) are not mature enough to exploit its practical applications. Although the EB scheme has been experimentally demonstrated in optical fibre and free-space [145–148], the ultimate application of the EB protocol is developing a global-scale quantum network. This ambitious target not only imposes stringent requirements on the performance of each core unit (such as entanglement source, linear processing circuits and quantum memory), but also requires a scalable, reliable and repeatable platform to build integrated quantum nodes for a large-scale quantum network. The optimal solution is a fully integrated photonic chip that achieves multi-scale integration of passive and active components. The crucial step to start the aforementioned long-term project is to use the existing CMOS infrastructure to develop an integrated platform that can efficiently generate, actively control and precisely analyse the entanglement states. In Chapter 4, a double-stripe silicon nitride waveguide is exploited for entanglement state generation, manipulation and analysis. The corresponding principles and experimental results are detailed in Chapter 4.

2.3.5 Two distribution channels

The ultimate image of QKD is to build a global-scale quantum communication network. To date, there are two viable channels to distribute the photon qubits between remote users-one is free-space and the other one is optical fibre. More than 2,000 km of key distribution has been experimentally demonstrated in both channels, as shown in Figure 2.16.

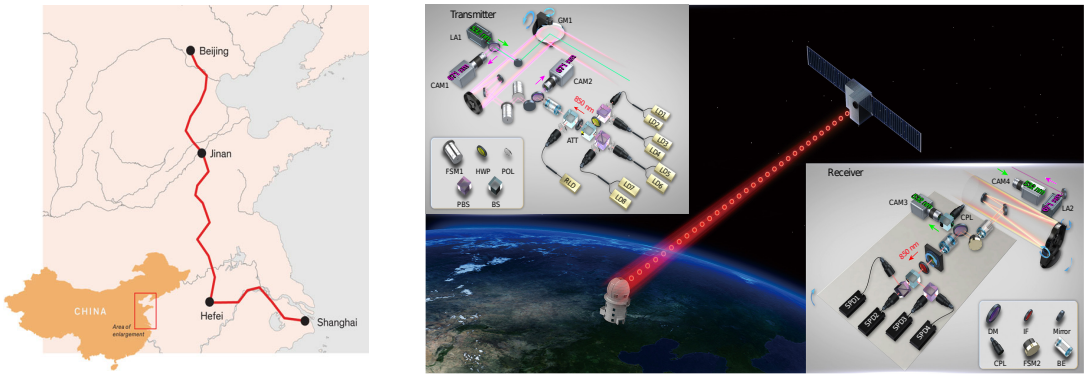

(a) (b)

FIGURE 2.16: QKD network based on fibre and free-space link. (a) Fibre link. (b) Free-space link [136].

Thanks to Charles K. Kao's pioneer work [149], the optical fibre became one of the most promising ways to transmit optical signals or single photons. The specifications of a standard single mode fibre (Corning SMF-28) show that its propagation loss at two telecom windows 1,330 nm and 1,550 nm is 0.35 dB/km and 0.2 dB/km, respectively. Although the propagation losses exponentially increase with the length of the optical fibre and the no-cloning theorem prohibits the amplification of single photons, dense coding and quantum memory can significantly elevate the capacity per qubit and the key distribution rate (or distance) in the future.

The free-space link is another promising channel to develop a global-scale quantum network. A recent demonstration of key distribution during the daytime significantly expands the applications of free-space QKD [150]. Propagation loss in a free-space channel mainly results from two aspects: atmospheric scattering and collection loss. In clear weather, the transmission loss of atmosphere in the telecom window from 1,520 nm to 1,600 nm is less than 0.1 dB/km [151]. The collection losses are determined by the apertures of the telescopes, the alignment between sender and receiver, and other vibration parts. There is a simple mode to estimate the overall transmission efficiency (t) of a free-space channel with length ℓ:

$$t \approx [d_r/(d_s + D\ell)]^2 \times 10^{-\alpha\ell/10}, \tag{2.43}$$

where d_r and d_s are the apertures of the sending and receiving telescopes, and D and α are the divergence of the beam and the atmospheric attenuation, respectively [121].

It is increasingly likely that optical fibre and free-space link will coexist in the future to construct a global-scale quantum network, as a result of their unique advantages. The free-space link is a better option for long-distance QKD between different countries or different continents than is the fibre-link [145]. Meanwhile, the optical-fibre link is a cost-efficient way to realise key distribution within a city or between different cities [152–154]. In practical circumstances, each channel prefers to encode the qubits in different degrees of freedom. In the free-space channel, the negligible decoherence of polarisation in free-space determines the

optimal way to encode the flying qubits. In optical fibre, a polarisation mode dispersion induced by the birefringent effect, temperature and stress variation will be the main obstacle to distributing polarisation qubits between remote users. Time-bin qubits that encode the key information in a time domain allow a robust scheme for a fibre link. This robust scheme, combined with an integrated photonic chip, paves the way to build a robust, scalable and cost-efficient quantum network in the real world-see Chapter 4.

2.4 Integrated quantum optics

This section briefly explains the motivation of integrated quantum optics and the two CMOS-compatible platforms, silicon and silicon nitride, used in this thesis.

2.4.1 Motivation

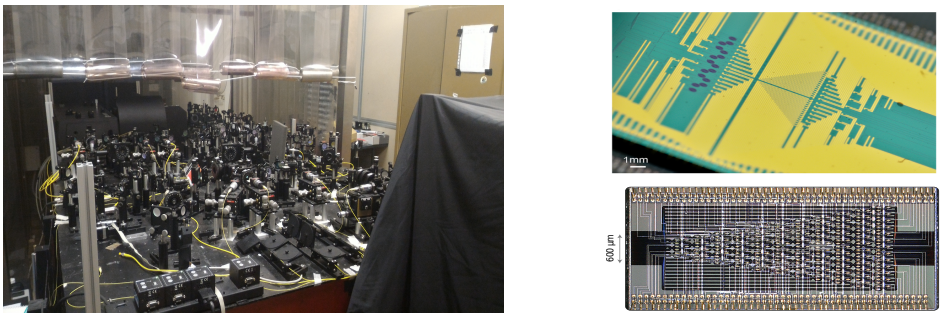

(a) (b)

TECHNOLOGY PLATFORMS FOR QUANTUM PHOTONICS

Metric	Silicon	Silica	Direct-Write	Si_3N_4	InP	GaAs	$LiNbO_3$
Density ($1/r^2$)	•••••	••	•	•••	•••	•••••	••
Loss ($1/ar$)	•••••	••••	••	••••	•••	••••	•••
Passive optics	•••••	•••••	••••	••••	••	•	•••
Active optics	•••	•	•	•	••••	•••	•••••
Photon sources	•••	•	••	••••	••	•••••	••••

(c)

FIGURE 2.17: Bulk optics and integrated optics. (a) Bulk optics [107, 155]. (b) Integrated optics. (c) Table of integrated platforms [156]. More dots indicate better performance.

Over the last two decades, research activities in the field of quantum optics not only exploited the surprising breakthroughs in fundamental science, but also investigated its potential in practical applications [19, 60, 67, 107, 136, 145, 154, 155, 157, 158]. The major challenge of its practical applications lies in developing a highly reliable and scalable photonic quantum system. The present-day technologies offer two available approaches to build such a quantum system: (I) bulk optics and (II) integrated quantum optics. Bulk optics is an excellent platform for

scientific demonstrations because of its ultra-low loss, straightforward qubit control and negligible cross-talk noise, as shown in Figure 2.17(a). However, it does not seem to be a viable approach to build a practical quantum system because of its lack of robustness, stability, and scalability. The optimal way to build such a reliable and scalable quantum system is integrated quantum optics that harnesses CMOS technologies, as with the two large-scale integrated photonic chips shown in Figure 2.17(b). A perfect integration platform for photonic quantum technologies requires high nonlinearity for photon generation and negligible linear and nonlinear loss for qubit processing. Figure 2.17(c) from Ref. [156] summarises the performance of several integrated platforms. It indicates that, to date, a perfect integration platform has not yet been demonstrated. For instance, the silicon platform has excellent nonlinearity for photon pair generation, but its linear and nonlinear loss severely limits its performance. Another typical example is the silicon nitride platform, which has demonstrated ultra-low propagation loss and negligible nonlinear loss within a broadband wavelength. In this thesis, silicon nanowire and double-stripe silicon nitride waveguide have been used to generate single and entangled photons and manipulate their quantum states. Therefore, Section 2.4.2 and Section 2.4.3 briefly explain the linear and nonlinear properties of silicon and silicon nitride platforms, respectively. A more comprehensive study can be found in [156, 159, 160].

2.4.2 Silicon

As well as playing a dominant role in micro-electronics, silicon is considered an excellent platform in the field of integrated quantum optics. Excellent nonlinearity and thermal conductivity allow efficient photon pair generation and active qubit control in the silicon platform. The silicon platform also offers a natural interface between electronic and optical devices. Compared with previous works in silica [161–167], the ultra-high nonlinearity ($\gamma \geq 300$ /W/m) and dense refractive index of silicon unlock a higher level of scaling and performance in quantum optics, as partially shown in Figure 2.18 and Figure 2.17(b) [159, 168–175].

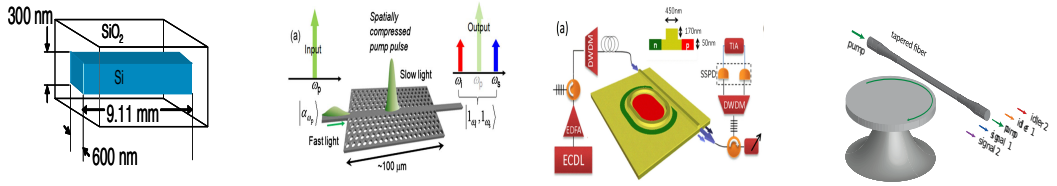

(a) (b) (c) (d)

FIGURE 2.18: Schematic of silicon sources. (a) Nanowire [176]. (b) Photonic crystal waveguide [171]. (c) Ring resonator [177]. (d) Micro-disk [170].

In Chapter 3 and Chapter 4, SFWM is used to generate correlated photon pairs in a 3 mm silicon nanowire fabricated by IMEC. Since the silicon crystal exhibits an inversion symmetry, the lowest-order nonlinear effects stem from the third-order susceptibility, $\chi^{(3)}$. As explained in Section 2.2.7, SFWM is a $\chi^{(3)}$ nonlinear process stochastically triggered by a vacuum state. The energy conservation and

phase-matching condition explained in Equation (2.32) and Equation (2.33) do not include the phase change induced by other Kerr nonlinear effects, such as self-phase modulation (SPM) and XPM. To include these processes, the overall momentum phase mismatch (κ) is added with additional term:

$$\kappa = \Delta k + \gamma_{p1} P_{p1} + \gamma_{p2} P_{p2}, \tag{2.44}$$

where k is the wave-vector of the single photons; P_{p1} and P_{p2} are the peak powers of the two pump fields; and γ is the nonlinearity, which can be described as:

$$\gamma = \frac{n_2(\omega_p)\omega_p}{cA_{eff}}, \tag{2.45}$$

where n_2 and c are the nonlinear refractive index of silicon at the pump frequency (ω_p) and the velocity of light (2.998×10^8m/s), respectively, and A_{eff} is the effective mode area of the pump field when it is confined to a waveguide:

$$A_{eff} = \frac{(\int\int_{-\infty}^{\infty} |F(x,y)|^2 dxdy)^2}{\int\int_{-\infty}^{\infty} |F(x,y)|^4 dxdy}, \tag{2.46}$$

where $F(x,y)$ is the mode distribution of the fundamental transverse electronic (TE) mode. In this thesis, non-degenerate SFWM is used to generate time-correlated photon pairs, instead of degenerate SFWM; therefore, the following discussion only considers non-degenerate SFWM. It is convenient to separate κ into two parts: $\Delta\beta$ represents the mismatch induced by dispersion, while ΔK_{NL} represents the phase mismatch because of other Kerr nonlinear effects. The term $\Delta\beta$ can be expressed in the Taylor series:

$$\begin{aligned} \Delta\beta &= \beta(\omega_s) + \beta(\omega_i) - 2\beta(\omega_{p1,2}) \\ &= \beta(\omega_p + \Omega) + \beta(\omega_p - \Omega) - 2\beta(\omega_p) \\ &= \beta_2\Omega^2 + \frac{2}{4!}\beta_4\Omega^4 + \frac{2}{6!}\Omega^6 + \cdots, \end{aligned} \tag{2.47}$$

where Ω represents the frequency interval (or detuning) between the pump and signal/idler. The higher-order terms of $\Delta\beta$, such as β_4 and β_6, are negligible parts compared with the first term, β_2, so that $\Delta\beta \approx \beta_2\Omega^2$. The corresponding ΔK_{NL} term is:

$$\Delta K_{NL} = 2\gamma_p P_p, \tag{2.48}$$

as $P_{p1} = P_{p2}$ in the non-degenerate SFWM. The overall phase mismatch, κ, can be simplified to:

$$\kappa = \beta_2\Omega^2 + 2\gamma P_p, \tag{2.49}$$

where β_2 is also known as the group velocity dispersion (GVD):

$$\beta_2 = \frac{d}{dw}(\frac{1}{v_g}), \tag{2.50}$$

which is used to describe the changing rate of the group velocity (v_g) while the light propagates inside a medium. In a waveguide, β_2 can be calculated by its dispersion, D:

$$D = -(\frac{2\pi c}{\lambda^2})\beta_2. \tag{2.51}$$

The TE mode distribution inside a silicon nanowire is shown in Figure 2.19(a). The negligible energy leakage outside the silicon core indicates the origins of nonlinear effects, the interactions between the pump pulses and the silicon nanowire. The 220 × 460 nm dimensions offer anomalous dispersion ($D > 0$ or $\beta_2 < 0$) for TE mode in the telecom-band, as shown in Figure 2.19(b).

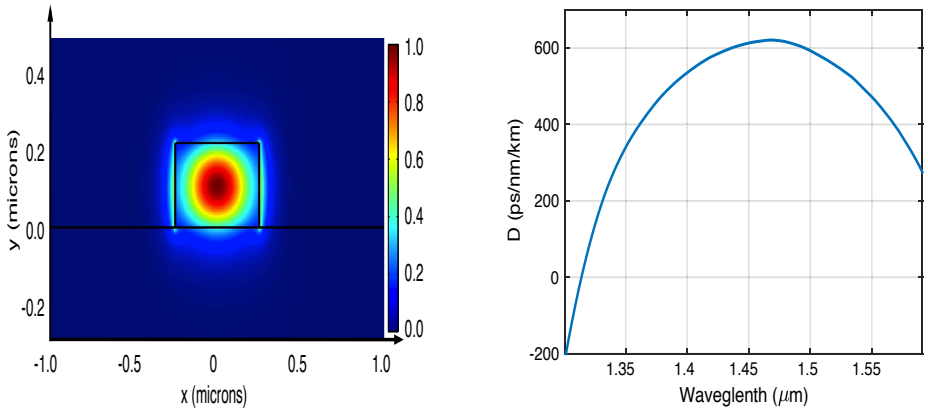

(a) (b)

FIGURE 2.19: Analysis of silicon nanowire. (a) TE mode distribution in silicon nanowire [178]. (b) Its dispersion.

After calculating the overall phase mismatch (κ), the average photon-flux spectral density from SFWM-defined as the number of photons generated per unit frequency and per time, at frequency detuning Ω between the pump and signal/idler-is generated over an effective length (L_{eff}) [179]:

$$f_x(L,\Omega) = \frac{1}{2\pi}\frac{\gamma^2 P_p^2}{|\varphi(\Omega)|^2}|sinh[\lambda(\Omega)L_{eff}]|^2, \tag{2.52}$$

where $\varphi(\Omega) = \sqrt{(\gamma P_p)^2 - (\beta_2\Omega^2 + 2\gamma P_p)/4}$. The effective length ($L_{eff}$) can be expressed as follows:

$$L_{eff} = \frac{1 - exp(-\alpha L)}{\alpha}. \tag{2.53}$$

Here, 3 mm length and 3 dB/cm propagation loss result in a 2.8 cm effective length. The γ of the silicon nanowire is around 300 /W/m. To significantly suppress the multi-photon contaminations in the SFWM, the peak power (P_p) of each pump pulse is usually limited to less than 1 mW, so that $\gamma P_p L_{eff} \ll 1$. In this condition, the average photon-flux spectral density from SFWM can be calculated by:

$$f_x(L,\omega) = \frac{(\gamma P_p)^2}{2\pi} sinc^2(\frac{\beta_2\Omega^2 + 2\gamma P_p}{2} L_{eff}), \tag{2.54}$$

The calculation results shown in Figure 2.20 indicates that the aforementioned silicon nanowire offers 12 THz full-width at half maximum (FWHM). Such a broad bandwidth allows sufficient frequency detuning between the pump and signal/idler to eliminate the pump leakage noise without sacrificing too much photon pair generation efficiency.

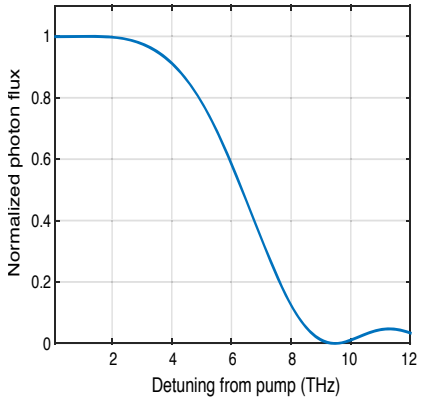

FIGURE 2.20: Normalised SFWM photon flux as a function of frequency detuning from pump frequency.

Although the high nonlinearity and refractive index of silicon allow fabrication of optical devices in a micro-scale footprint, silicon is not a perfect integration platform in two aspects. One is that the 3 dB/cm propagation loss in the standard silicon nanowire (220 × 460 nm) prohibits the construction of long circuits, as single photon qubits will dissipate during the linear transmission and processing. The potential solutions include an etchless silicon waveguide with 0.3 dB/cm [68] and a hybrid integration, such as silicon-silica [180]. The nonlinear loss of silicon platform, such as TPA and FCA, is an intrinsic hurdle of the silicon platform [93]. TPA and FCA are explained in the next section.

Two photon absorption and free carrier absorption

TPA is a process where two photons are absorbed simultaneously by a material to excite a single atom or ion to an excited state. In silicon, half of the band-gap energy (0.6 eV) is smaller than the photon energy at 1,550 nm (0.8 eV). Therefore, TPA will adversely affect the generation efficiency of SFWM at a wavelength of around 1,550 nm. TPA not only reduces the collection efficiency, but also affects the phase matching condition of SFWM. With the presence of TPA, the nonlinear phase shift parameter (ϕ) for SFWM can be expressed as:

$$\phi = \frac{\gamma A_{eff}}{\alpha_2} ln[1 + \alpha_2 I_p L_{eff} \frac{n_g}{n_0}], \tag{2.55}$$

where α_2 is the TPA coefficient, $I_p = P_p / A_{eff}$ is the pump intensity with the peak power P_p, and n_g and n_0 are the group index and refractive index, respectively.

Meanwhile, the generated photon pairs are affected by TPA. The collection efficiency determined by TPA can be expressed as follows:

$$\eta_{TPA} = \frac{n_g^2}{(1+\alpha_2 I_p L_{eff})^2}. \tag{2.56}$$

Moreover, free electrons released by TPA will also absorb the generated photons; this process is known as FCA. The collection efficiency determined by FCA can be described as follows:

$$\eta_{FCA} = \frac{1}{[1+\sigma N_c L_{eff}(2\alpha)](1/2)}, \tag{2.57}$$

where σ and N_c are the absorption cross-section and free-carrier density, respectively. Overall, TPA and FCA not only modify the phase matching of SFWM, but also add an extra nonlinear loss into the overall photon collection efficiency, $\eta_{NL} = \eta_{TPA}\eta_{FCA}$.

2.4.3 Silicon nitride

Another CMOS platform, Si_3N_4, has attracted significant research interest over the last decade because of its promising results and unique properties compared with silicon. Although the nonlinearity (γ) of the Si_3N_4 waveguide is not as high as silicon, the maximal photon pair generation rate in a silicon ring resonator is surpassed by a Si_3N_4 ring resonator, which can generate $> 10^7$ single-photon pairs per second [181]. Unlike the limited transparency window at the telecom window and nonlinear absorption in the silicon platform, Si_3N_4 has an ultra-broadband transparency window from 400 nm to 8 µm and negligible nonlinear loss [181]. Meanwhile, the Si_3N_4 platform allows ultra-low propagation losses (<0.3 dB/cm), such as the buried waveguide [182, 183], box-shape waveguide [184, 185], single-stripe waveguide [185–187] and double-stripe waveguide [13, 99, 188, 189], as shown in Figure 2.21. The ultra-low propagation loss enables the fabrication of long circuits, which is prohibited in silicon nanowire, such as an unbalanced Mach-Zehnder interferometer with a 14 cm arm [13].

In Chapter 4, a double-stripe silicon nitride waveguide, as shown in Figure 2.21(d), is used to construct linear processing circuits and nonlinear photon pair source. These silicon nitride circuits are fabricated by LioniX. The double-stripe structure only allows the transmission of TE mode with 0.1 to 0.2 dB/cm propagation loss. Figure 2.22(a) shows the TE mode distribution in a double-stripe Si_3N_4 waveguide structure, with most of the energy confined in the two Si_3N_4 stripes, so that the photon pairs are mainly generated from the interaction between Si_3N_4 and pump pulses, rather than silica. Using Equation (2.45) and Equation (2.46), the estimated nonlinearity (γ) of the double-stripe Si_3N_4 waveguide is 0.233/W/m, with $n_2 = 2.5^{-15} cm^2/W$ [103, 182]. The β_2 of the double-stripe Si_3N_4 waveguide is estimated as 750 ps^2/km, which is referred to the dispersion value elucidated in Ref.[188]. In Chapter 4, the nonlinear property of the double-stripe structure is exploited in a 6.5 cm Si_3N_4 waveguide. Based on Equation (2.53), the effective length (L_{eff}) is 6.39 cm. The relatively low γ results in large pump power to generate time-correlated photon pairs, so that

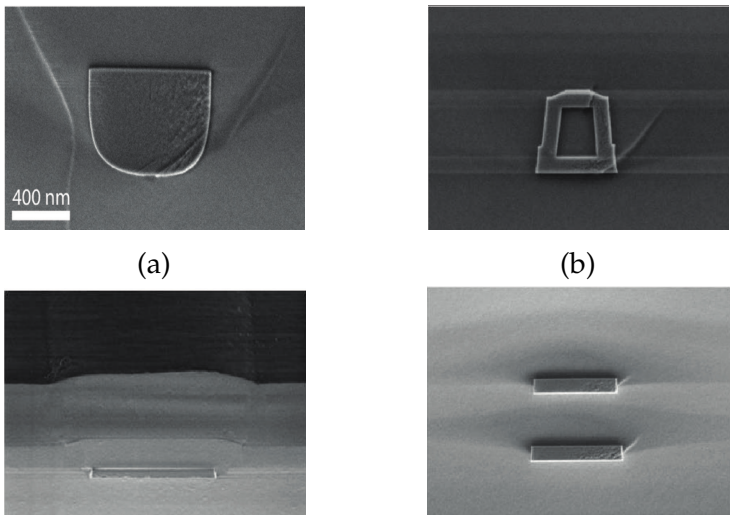

FIGURE 2.21: SEM images of silicon nitride waveguide [69, 189]. (a) Buried waveguide. (b) Box-shape waveguide. (c) Single-stripe waveguide. (d) Double-stripe waveguide.

$\gamma P_p L_{eff} \gg 1$. In this condition, the average photon-flux spectral density from SFWM is expressed as follows:

$$f_x(L,\Omega) = \frac{1}{2\pi}\frac{\gamma^2 P_p^2}{2g^2(\Omega)} e^{2g(\Omega)L_{eff}}, \tag{2.58}$$

where $g(\Omega) = \sqrt{(\gamma P_p)^2 - (2\gamma P_p - |\beta_2|\Omega^2)^2/4}$ [179]. The photon flux shown in Figure 2.22(b) indicates 2.4 THz FWHM of SFWM. The blue arrow in Figure 2.22(b) indicates the frequency detuning between the pump and signal/idler.

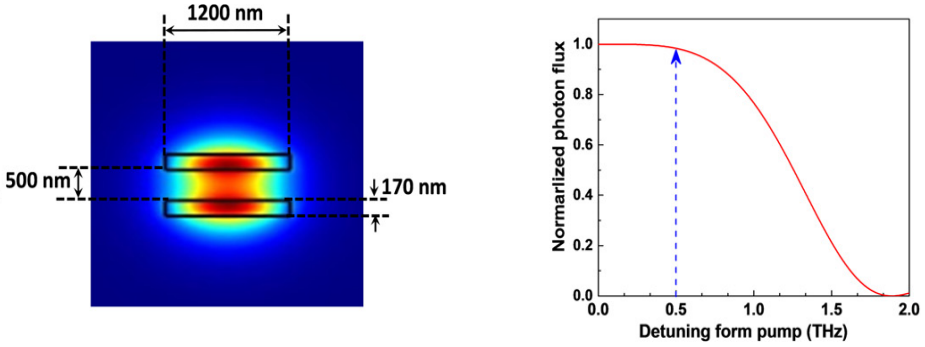

FIGURE 2.22: TE mode distribution and SFWM bandwidth in Si_3N_4 waveguide [99]. (a) TE mode distribution. (b) Bandwidth of SFWM. The blue arrow indicates the 500 MHz detuning.

Although efficient photon pair generation and ultra-low loss transmission have been demonstrated on Si_3N_4 platform, as an amorphous material, the SpRS is the intrinsic noise source that hinders the potential applications of Si_3N_4 platform. SpRS is explained in the next section.

Spontaneous Raman scattering

In contrast to an elastic scattering (Rayleigh scattering), Raman scattering is an inelastic scattering of photons. In Rayleigh scattering, the energy of the scattered photons is identical to the incident photons. However, in inelastic scattering (such as Raman scattering), the scattered photons have different energy from the incident photons. The physical image of Raman scattering is the interaction between the photons and phonons existing in a material. Phonons are the quanta of molecular vibrations. There are two types of Raman scattering: (I) Stokes scattering, which indicates that a photon lose energy to a phonon, and (II) anti-Stokes scattering, which gains energy from a phonon. Here, Stokes scattering and anti-Stokes scattering result in a red and blue shift to the incident photon, respectively.

In a high pump power regime, the occurrence of stimulated Raman scattering (SRS) results in an exponential nonlinear gain. However, in a low (or weak) pump power regime, SpRS plays an important role, instead of SRS. In SpRS, the number of Raman-scattered photons is proportional to the density of the phonon state in the material and the thermal occupation of the phonon bath, so that SpRS scales linearly with the effective length of the medium (L_{eff}) and the peak power of pump pulses (P_p).

As a crystalline material, silicon has a narrow Raman scattering peak at approximately 18 THz detuning away from the pump wavelength, so that SpRS plays a negligible role in a silicon-based nonlinear photon source. In contrast, as an amorphous material, SpRS in Si_3N_4 has a broadband spectrum that could overlap with the spectrum of SFWM with the same pump pulses [190]. With the presence of SpRS, the quality of a heralded single-photon source is degraded as uncorrelated photons are generated by SpRS. However, the SpRS will be mitigated in the future, since the entire system is most likely immersed into a cryogenic circumstance to achieve optimal single-photon detection [156]. The ultra-low temperature will significantly suppress SpRS because of the limited molecule vibrations [99, 191]. The SpRS photon-flux spectral density in either signal (or idler) channel can be calculated as [192–194]:

$$f_{SpRS}(L,\Omega) = P_p L_{eff} \left| g_R(\Omega/2\pi) \right| (n_{th}+1), \tag{2.59}$$

where $g_R(\Omega/2\pi)$ is the Raman gain spectrum of Si_3N_4 waveguide, defined as:

$$g_R(\Omega/2\pi) = 2\gamma f_R Im[h_R(\Omega/2\pi)]. \tag{2.60}$$

Here, f_R is the fractional contribution of the delayed Raman response, and n_{th} is the photon population at frequency Ω and temperature T, which is described by the Bose-Einstein distribution explained in Equation (2.6). The Bose-Einstein distribution indicates that the photon flux spectral density of SpRS in the signal/idler channel is affected by the temperature. If the Si_3N_4 waveguide is cooled down to the temperature of liquid nitrogen, the Raman noise is expected to be suppressed by 70.6%.

Chapter 3

Temporal multiplexing of heralded single-photon sources

Chapter 3 discusses three temporal multiplexing (TMUX) schemes to build a high-efficiency single-photon source for large-scale photonic quantum computing as well as the potential limitations of TMUX with high repetition rate.

Section 3.2 is written based on the following publication:
Chunle Xiong, Xiang Zhang, Matthew J. Collins, Andri Mahendra, Luke G. Helt, Michael J. Steel, Duk-Yong Choi, Chang Joon Chae, Philip H. W. Leong, and Benjamin J. Eggleton, "Active temporal multiplexing of indistinguishable heralded single photons," *Nature Communications* **7**, 10853 (2016).

Section 3.3 is written based on the following publications:
Xiang. Zhang, Iman Jizan, Jiakun He, Alex S. Clark, Duk-Yong Choi, Chang Joon Chae, Benjamin J. Eggleton, and Chunle Xiong, "Enhancing heralded single-photon rate from a silicon nanowire by time and wavelength division multiplexing pump pulses," *Optics Letters* **40**, 2489-2492 (2015).
Xiang Zhang, Runyu Jiang, Bryn A. Bell, Duk-Yong Choi, Chang Joon Chae, Chunle Xiong, and Benjamin J. Eggleton, "Interfering heralded single photons from two separate silicon nanowires pumped at different wavelengths," *Technologies* **4**, 25 (2016).

Section 3.4 is written based on the following publication:
Xiang Zhang, Yeehui Lee, Bryn A. Bell, Philip H. W. Leong, Terry Rudolph, Benjamin J. Eggleton, and Chunle Xiong, "Indistinguishable heralded single photon generation via relative temporal multiplexing of two sources," *Optics Express* **25**, 26067-26075 (2017).

Section 3.5 is written based on the following publication:
Xiang Zhang, Bryn A. Bell, Mark Pelusi, Jiakun He, Wei Geng, Yunchuan Kong, Philipp Zhang, Chunle Xiong, and Benjamin J. Eggleton, "High repetition rate correlated photon pair generation in integrated silicon nanowires," *Applied Optics* **56**, 8420-8424 (2017).

3.1 The concept of multiplexing

As explained in Section 2.2.5, the major hurdle that hindering the development of large-scale photonic quantum computing is the lack of a high-efficiency single-photon source. Compared with the single-photon emitter, heralded single-photon source is a more promising solution since single photons generated from separate sources are highly indistinguishable from one another. However, it is a formidable challenge to efficiently generate single photons from stochastic nonlinear processes, such as SPDC and SFWM. The theoretical analysis indicates that multiplexing (MUX) scheme is a potential way to build a high-efficiency single-photon source from a probabilistic nonlinear process [109, 110, 195]. MUX schemes have been proposed which use different degrees of freedom, such as spatial MUX [109], temporal MUX [110], and frequency MUX [8, 196]. Regardless of different degrees of freedom, these schemes are conceptually similar from one another. The core concept of MUX is operating numbers of probabilistic processes simultaneously and routing the successfully heralded single photons to a fixed mode via an active switching network so that the μ can be significantly enhanced.

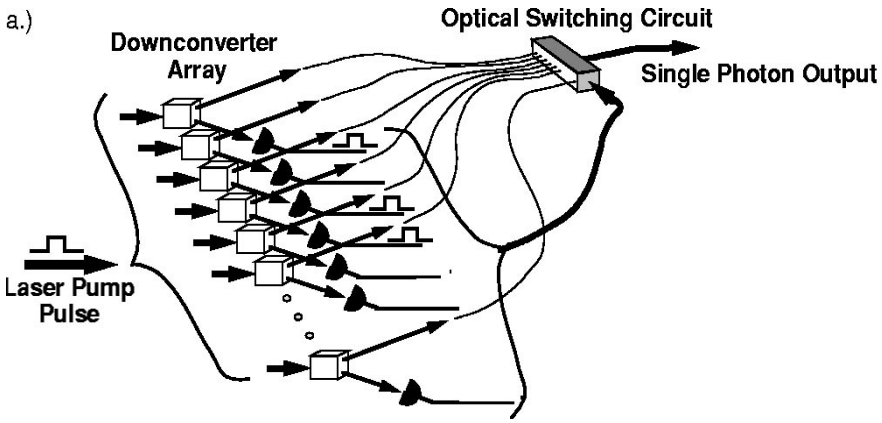

FIGURE 3.1: The principle of the SMUX [109]

As a typical example, SMUX has been first proposed by A. L. Migdall et al. in 2002 [109]. Figure 3.1 shows the principle that numbers of nonlinear medium arranged in an array are simultaneously pumped by synchronised laser pulses. The nonlinear optical process, such as SPDC, randomly generates a time-correlated single-photon pair in the array and the detection of a heralding photon indicates the existence of its partner—a heralded single photon. The heralding detection controls an optical switching circuit that routes the heralded single photon to the output mode. In this scheme, the heralded single-photon rate is linearly enhanced with the number of nonlinear medium after excluding the loss of the switching circuit. Meanwhile, the multi-photon noise remains fixed, because only one nonlinear medium is connected to the output at a time. In 2011 and 2013, X. Ma et al. and M. J. Collins et al. experimentally demonstrated the SMUX in β-barium borate and silicon-based photonic crystal waveguide [5, 105], respectively. The schematics and experimental results presented in Figure 3.2

demonstrate that the heralded single-photon rate is linearly enhanced with the number of the spatial mode.

Although in these proof-of-principle demonstrations, the photon generation probability has been significantly enhanced, it has not satisfied the threshold of 0.75, as explained in Section 2.2.5. Developing a high-efficiency single-photon source via SMUX requires large amounts of nonlinear sources, optical switches and single-photon detectors. Therefore, SMUX is an unfavourable scaling solution for large-scale photonic quantum computing as it suffers an overhead of physical resources.

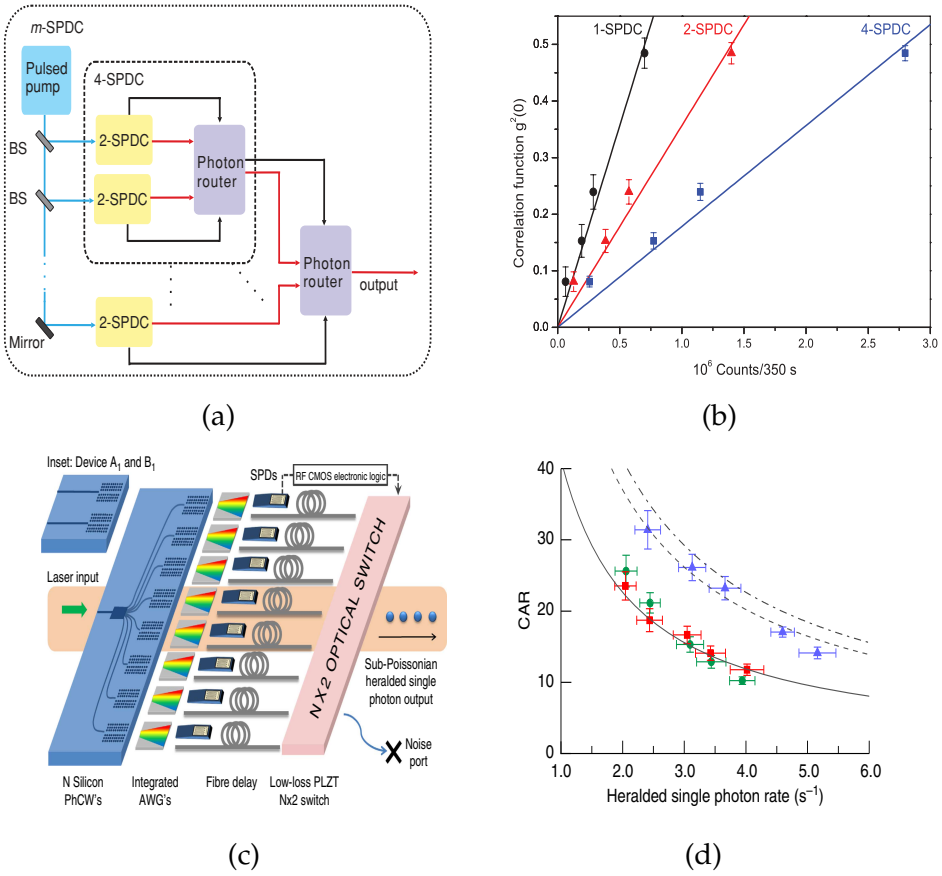

FIGURE 3.2: Schematics and measurement results of the SMUX [5, 105]. (a) The spatial modes are increased with the number of SPDC crystals. (b) The photon counts are linearly increased without sacrificing the $g^{(2)}(0)$ value. (c) The spatial modes are increased with the number of integrated waveguides. (d) The heralded single-photon rate is enhanced by 63.1% after subtracting the loss from an optical switch.

In 2011, J. Mower and D. Englund proposed a TMUX scheme to build a high-efficiency heralded single-photon source [110]. Figure 3.3 presents their proposal which includes three blocks: photon pair generation, heralding decision and variable delay circuits. Compared to SMUX, each output of TMUX requires only one nonlinear source for pair generation, one detector for heralding detection and the switch number is reduced to $\log_2 N + 1$ instead of $N - 1$ in SMUX, where N is a number of temporal (or spatial) mode. TMUX significantly reduces

the physical resource for each single-photon source and opens the possibility of large-scale photonic quantum computing which requires N-photon simultaneously to outperform classical computing. Numerous experimental demonstrations of TMUX show a significant enhancement of the single-photon generation probability [8, 66, 106, 175, 196–201]. Three TMUX schemes, active temporal multiplexing (ATM), time and wavelength division multiplexing (TWDM) and relative temporal multiplexing (RTM), are experimentally demonstrated in Section 3.2, 3.3 and 3.4, respectively.

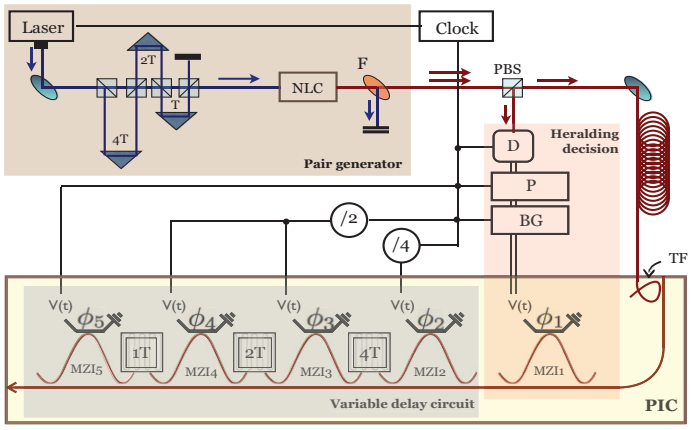

FIGURE 3.3: The proposal of the TMUX [110]

3.2 Active temporal multiplexing

This section explains an experimental demonstration of ATM. It is separated into three sections: principle, experimental methods and measurement results.

3.2.1 Principle

ATM scheme extends the mode number (N) in temporal domain instead of spatial domain, as shown in Figure 3.4. The identical green pulses with a period of T indicate the pump pulses with the same peak power and these pump pulses also define temporal modes (or time-bins). Due to the identical pump pulses, time-correlated single-photon pairs are randomly generated at any temporal modes with the same probability. The detection of a heralding photon (red) tells the temporal mode of a heralded single photon (blue) and a relative time delay between the detected mode and fixed mode, such as t_1. The logic signals generated from heralding detections control an active switching network to precisely shift heralded single photons to t_1. Compared with one pump pulse at period $4T$, a group of pump pulses at period T are approximately four times as likely to generate a photon pair in the given time frame of $4T$ due to the identical pump pulses. Although the random nature of the generation process within each time-bin remains the same, heralded single photons are constantly shifted to t_1 so that the heralded single-photon generation probability at the $4T$ clock period is enhanced.

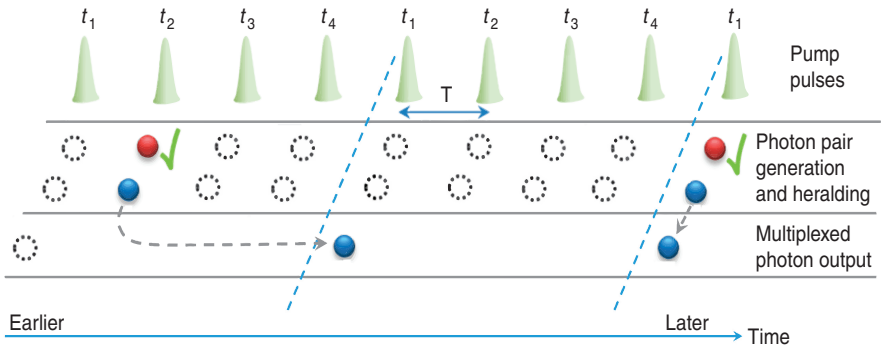

FIGURE 3.4: The principle of the TMUX.

3.2.2 Experimental method and setup

To implement the scheme shown in Figure 3.4, an experimental method is designed as shown in Figure 3.5. A mode-locked fibre laser with a repetition rate of 10 MHz (100 ns period) produces 10 ps width pump pulses centred at 1,550 nm. Each pulse is split into four pulses spaced by 25 ns using two 1-to-4 fibre couplers and three optical tunable delay lines. The four pulses then propagate along a 3 mm long nonlinear silicon nanowire as explained in Section 2.4.2, probabilistically generating time-correlated photon pairs via SFWM in the four time-bins. As a result of energy conservation and phase matching, photon pairs are generated at frequencies symmetrically around the pump over a 6 THz bandwidth. An array waveguide grating (AWG) (100 GHz channel spacing and 50 GHz channel bandwidth) is used to select the photon pairs generated at 1,545 and 1,555 nm, block the pump, and spatially separate the two photons of each pair. The 1,555 nm photons are detected by a fast and low-noise niobium nitride superconducting single-photon detector as the heralding signals. These signals contain the temporal information of the heralded photons (1,545 nm) and are sent to a field-programmable gate array (FPGA) for analysis and switch control.

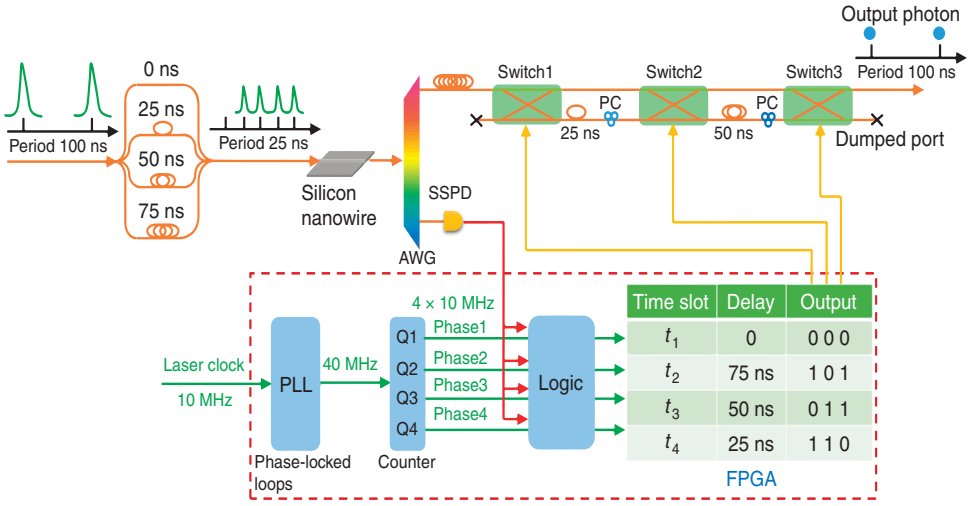

FIGURE 3.5: The experimental method

A phase-locked loop (PLL) in the FPGA is used to lock and multiply the laser's original 10 MHz clock to a 40 MHz clock. A finite state machine operating on the 40 MHz clock generates four non-overlapping clocks at four phases relative to the 10 MHz clock. A heralding photon detection signal from the superconducting single-photon detector (SSPD) is integrated with each clock phase and an appropriate three binary-digit output latches. The output is connected to the switching network so that the heralded photons (1,545 nm) are routed into the appropriate sequence of delay lines, as shown in Figure 3.5. To precisely shift the heralded single photons to the right temporal modes, such as t_1, three synchronisations are implemented in this work. Synchronisation (I): the 40 MHz clock of the FPGA and the heralding detection so that the FPGA could find out which time-bin the heralding photons are generated. Synchronisation (II): the switching electronic signals from the FPGA and the heralded photons arriving at the switches so that proper delays could be applied to the photons. Synchronisation (III): the relative optical delays in the four channels of the fibre couplers and in the switching network. The synchronisation process is explained in the Appendix A.1.1 with more details.

Beside the synchronisation process, the loss of the switching network is carefully managed. To receive any benefit from a four temporal mode MUX setup, the switching network must have a total loss below the four times (that is, 6 dB) maximum expected enhancement. The optical ceramic switches, made from ultra-low loss lead lanthanum zirconium titanate (PLZT), are fibre pigtailed and spliced with the fibre delay lines to minimise the loss of each path to around 2.8 dB, with $\pm$0.3 dB difference between different routes. Since this loss difference is much less than the overall loss in the experiment, its effect on output photon statistics is negligible. The experimental methods described so far ensures indistinguishability in the spectral and temporal degrees of freedom, but indistinguishable polarisation is also required. In Figure 3.5, the heralded photons from different time-bins have the same polarisation before they enter the switching network. However, they experience different optical paths to obtain the correct delays, and to minimise losses these components are not polarisation maintaining. This is addressed using two polarisation controllers with 0.1 dB loss applied to the two optical delay lines and the approach is explained in the Appendix A.1.2.

The full setup of the ATM experiment is illustrated in Figure 3.6. The top half of the diagram, excluding the 50:50 coupler before the two avalanche photodiodes (APDs: ID210, Id-Quantique), is for the CAR measurements of the source with four temporal-mode MUX. When doing the measurements for the source without MUX, only one of the four channels of the 1-to-4 fibre couplers is connected, and the switching network is removed. This arrangement allows the least change to the experimental conditions for the MUX and NO MUX measurements, and thus guarantees a fair comparison between them. Because the losses of the four channels of the fibre couplers are slightly different, one polarisation controller is used in each channel and an inline-polariser immediately after the fibre couplers to ensure the pulses in the four temporal modes after the inline-polariser have the same intensity. A fast optical sampling oscilloscope (OSC) is used to monitor the pulse intensities. The bottom half of Figure 3.6 is a second

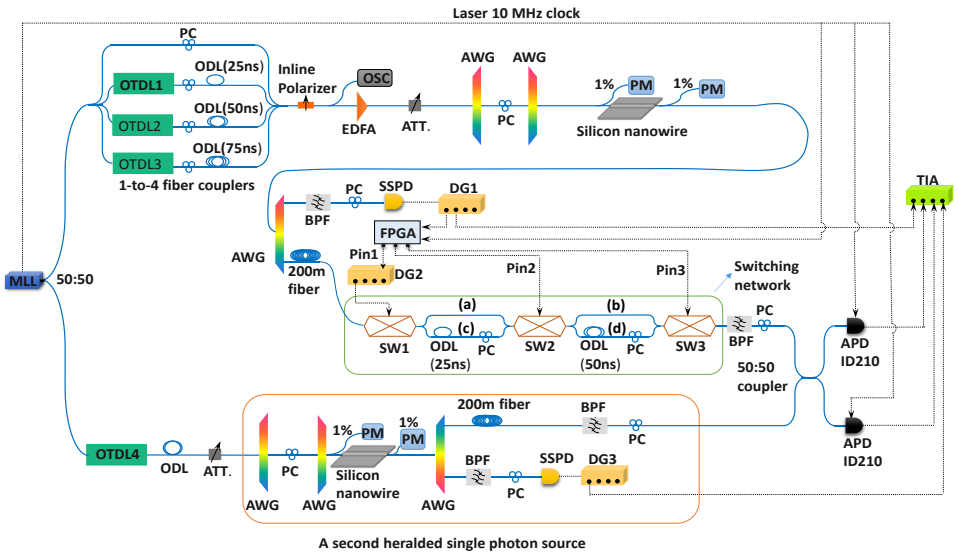

FIGURE 3.6: Full setup of the experiments. Solid and dashed lines represent optical fibres and electronic cables, respectively. MLL: mode-locked laser, OTDL: optical tunable delay line, ODL: optical delay line, PC: polarisation controller, ATT: attenuator, OSC: oscilloscope, AWG: arrayed waveguide grating, PM: power meter, SSPD: superconducting single-photon detector, DG: delay generator, FPGA: field-programmable gate array, SW: switch, BPF: bandpass filter, APD: avalanche photodiode, TIA: time interval analyser.

heralded single-photon source based on a silicon nanowire with the same specification to that used in the MUX experiments. This source is pumped by 10 MHz laser clock, and provided a reference for the indistinguishability verification of the multiplexed photons via the fourfold HOM quantum interference.

When we perform the CAR measurements for the NO MUX and MUX photon sources, the 50:50 coupler is took out of the setup and the heralded photon output is directly connected to one ID210 detector. In both cases, the heralded photon events detected by an ID210 triggered by the 10 MHz laser clock are used as the 'start', and the heralding photon events detected by a SSPD are used as the 'stop' for the time interval analyser (TIA) to construct the histograms: coincidences vs time delay between 'start' and 'stop'. This 'start' and 'stop' arrangement is different from the standard way of using heralding signals as the 'start' and heralded as the 'stop' just for our experimental convenience to adjust the delays, and it does not change the underlying principle. A suitable electronic delay is applied to the heralding detection signals so that the delay in the histogram is always within the 0–250 ns time window.

3.2.3 Experimental results and discussions

The key to verifying the enhancement of the ATM scheme is to compare the heralded single-photon output probability per 100 ns clock period (that is, the original 10 MHz clock) at the same multi-photon noise level for sources with and without the MUX switching network. These two quantities are characterised by

CAR measurements. Figure 3.7 shows histograms for the NO MUX and MUX sources in CAR measurements. For the NO MUX source (Figure 3.7(a)), all counts in the coincidence peak and the accidental peak closest to the coincidence peak are summed up as C and A, respectively. The time interval between the peaks is the pump laser period. The ratio between C and A gives CAR. For the MUX source (Figure 3.7(b)), depending on in which time-bin the heralded photons are generated, they experience different optical delays to be multiplexed to the 10 MHz clock; however the heralding photons are still on the 40 MHz clock, so there are four coincidence peaks (the signature of successful MUX). These peaks look slightly different from one another because photons generated in different time-bins experience slightly different losses when propagating through different optical paths. Each coincidence peak should have their corresponding accidental peak. Two accidental peaks nearly disappear because the photons that are generated in time bins t_2 and t_4 require logic '1' be applied to switch (SW1) (see Figure 3.5 and Figure 3.6). This switching operation on SW1 only allows heralded photons to arrive at the detector when there are heralding detections, and therefore switches away all other events that may give rise to coincidences in the accidental peak. To calculate the CAR for the MUX source, the counts in all four coincidence peaks are summed up as C; and the overall counts in the two visible accidental peaks are multiplied by two as A. This process is considered to be fair because: first, the sources pumped by each individual temporal mode have been tested to have the same performance; second, corresponding to the loss differences between the different paths, the accidentals for t_3 should be higher than those for t_2, while the accidentals for t_1 should be lower than those for t_4, and the total accidentals for t_1 and t_3 can approximately represent those for t_2 and t_4.

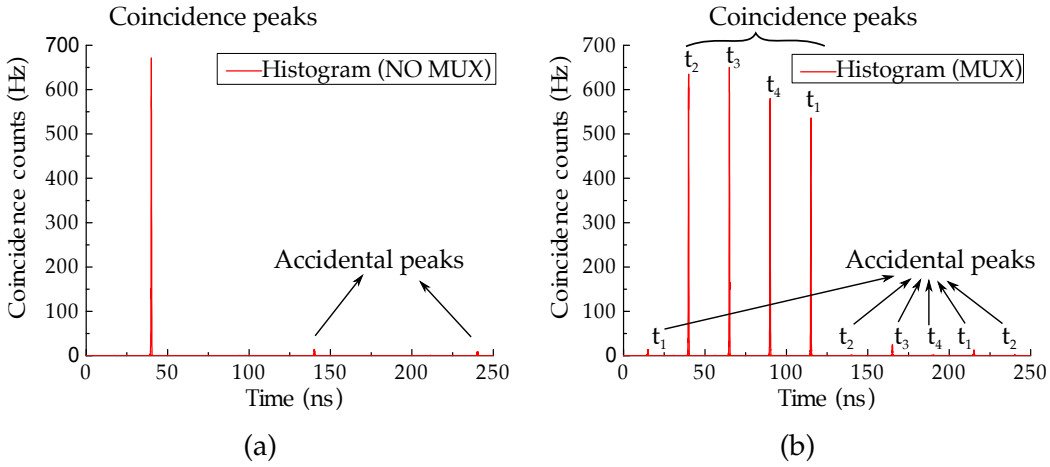

FIGURE 3.7: The histogram without MUX (a) and with MUX (b)

The measured CAR as a function of the coincidence rate without MUX (NO MUX, that is, pumping at 10 MHz) is plotted in Figure 3.8, indicated by blue diamonds. The CAR decreases with the increased coincidence rate due to multi-pair noise. For comparison, the CAR measurement is performed at the same pump peak powers for the multiplexed source (MUX, that is, pumping at 40 MHz and adding the switching network to the setup). The results are plotted as red triangles in Figure 3.8. The CAR still decreases with the increased coincidence

rate because the original NO MUX sources have this feature. However, when compared with the NO MUX source, at the same CAR, that is, the same multi-pair noise level, the coincidence rates are nearly doubled. At the highest power level in the experiment, the detected coincidence rate has been increased from $\sim$ 300 Hz for the source without MUX to nearly 600 Hz after performing MUX. The analytic plots presented in Figure 3.8 are derived by Equation (2.38) with the experimental conditions, such as the collection efficiency and the dark counts. As simply doubling the number of pump pulses per period (that is, keeping the same peak power and without an active switching circuit) can lead to similar results in Figure 3.8, the improvement is expressed as an enhancement factor of MUX/NO MUX heralded single-photon output probability per 100 ns at the same CAR level, as explained in the following paragraphs.

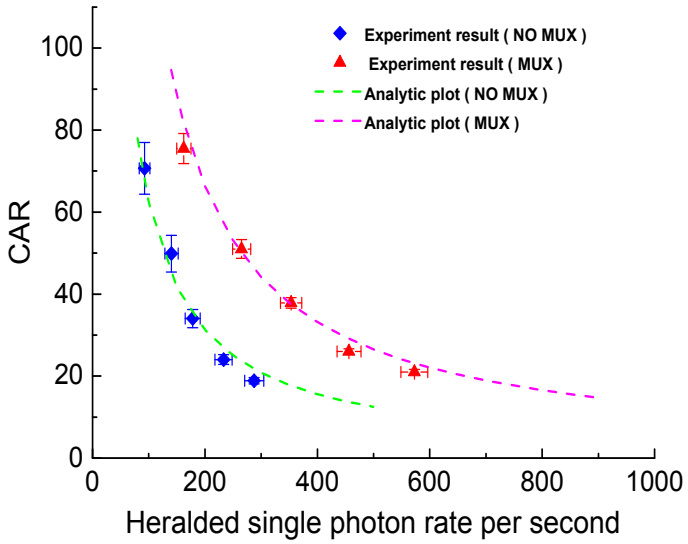

FIGURE 3.8: CAR as a function of coincidence rates. Poisson error bars are used for plot, see Equation (2.36).

The enhancement is due to the fact that in the NO MUX case, there is a single pump pulse per 100 ns, while in the MUX case, there are four pump pulses per 100 ns; and the ratio between single- and multi-pair probabilities remains the same when the pulses have the same peak power. Since heralded single photons are detected by a threshold photon detector instead of a photon number-resolving detector, the heralded single-photon output probability cannot be measured directly. It is inferred from the coincidences measured by the threshold detector. Taking into account the losses of waveguide-fibre coupling, spectral filters and the efficiency of detectors, the average number of photon pairs per 100 ns clock period is estimated from the measured coincidence rate at each CAR level, and then the heralded single-photon output probabilities is inferred by using a thermal distribution function for both NO MUX and MUX sources. It is appropriate to use the thermal distribution to describe the photon statistics in this work, because both the generated photons and the pump are filtered by array waveguide gratings with the same channel bandwidth of 50 GHz in the experimental setup (see Figure 3.6). The heralded single-photon generation probability per 100 ns

clock period is inferred by $P_1 = \mu/(1+\mu)^2$. μ is the average number of the generated pairs per 100 ns clock period calculated by the measured coincidences (C) and the overall collection efficiency (η) in the heralding and heralded photon arms, as explained in Section 2.2.7. The enhancement factor of MUX is analysed by comparing $P_1\eta$ with MUX and without MUX since $P_1\eta$ represents the heralded single-photon output probability. The analysis value at each CAR level is plotted in Figure 3.9 as circles, showing that the four temporal mode MUX nearly enhances the heralded single-photon output probability by 100% (that is, 3 dB). The enhancement is less than the ideal factor of 4 (that is, 6 dB) because of the 3 dB loss of the switching network.

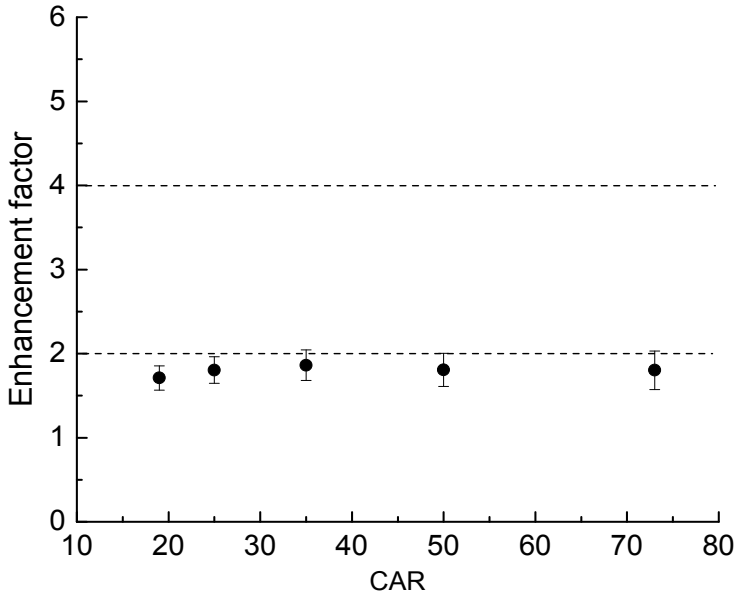

FIGURE 3.9: The inferred enhancement factor to the heralded single-photon output probability at each CAR level. Poisson error bars are used for plot, see Equation (2.36).

For the multiplexed source to be useful, the multiplexed heralded single photons must be indistinguishable from one another. This is tested by HOM quantum interference [202]. Another heralded single-photon source based on a second 3 mm long silicon nanowire is pumped by the same 10 MHz laser, but without MUX. The photons generated from this second source are in a certain spatial-temporal state, that is, in an identical polarisation state and at the accurate 100 ns clock cycle of the laser, and so they provide a reference to check if the multiplexed photons are indistinguishable. Note that as the array waveguide grating channels used to filter the generated photons have a slightly larger bandwidth (50 GHz) than the pump (10 ps transform limited pulses corresponding to 44 GHz), the photons to be interfered have some chance to be in different spectral modes. This may slightly reduce the HOM interference visibility [203].

As the photons to be interfered at a 50:50 beam splitter must be heralded by their corresponding partner photons, the HOM interference here actually involves fourfold (or four photons) coincidence measurements (see Figure 3.6). Because the fourfold coincidence rate from two separate sources is very low due

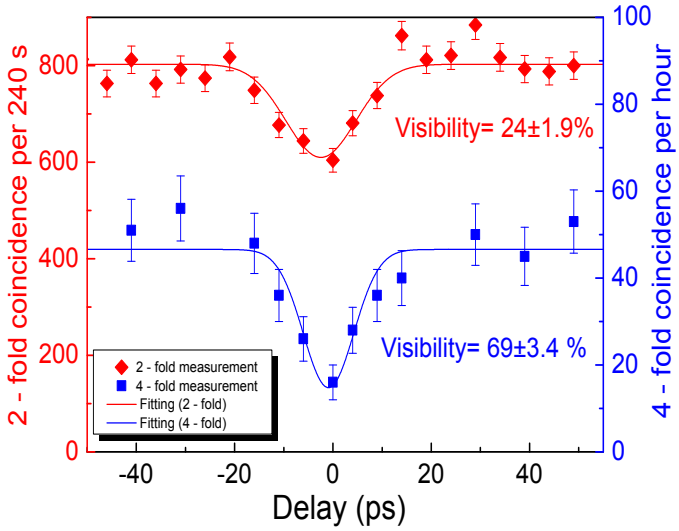

FIGURE 3.10: The results of twofold (2-fold) and fourfold (4-fold) quantum interference. Poisson error bars are used for plot, see Equation (2.36). Solid lines are Gaussian fits according the spectral filtering shape in the experiment.

to the low photon collection efficiency, a standard twofold interference measurement (that is, without heralding information) is first performed to find the appropriate delay between photons from the two sources [204]. In this measurement, the pump powers are set at a level of CAR=18 for both. The twofold dip shows a raw visibility of 24±1.9% (diamonds in Figure 3.10). After the twofold measurements, the fourfold HOM interference measurement is taken, but at higher pump powers for both sources in order to have sufficient coincidence counts to make the statistics meaningful in a reasonable amount of measurement time (for example, 50 coincidences in one hour) with low-efficiency detectors. The cost is that the CAR drops to 7, and more multi-photon noise is generated and reduces the visibility of the HOM dip. After adjusting the time delay explained in Appendix A.1.3, a fourfold HOM dip with raw visibility of 69±3.4% (squares in Figure 3.10) is observed in the measurement, indicating that non-classical interference occurred between the multiplexed photons and the photons from the second source. To check that the residual photon distinguishability is not because of MUX but due to multi-photon noise at high pump powers and the detector dark count. The noise contribution of the dark count and the multi-photons from each source are measured separately [8]. The multi-photon noise from the MUX source and the dark counts is quantified as C_{n1} in a fourfold coincidence measurement after disconnecting the fibre link between one input of 50:50 coupler and the second source. Vice versa, the multi-photon noise from the second source and the dark counts is obtained as C_{n2}. Subtracting C_{n1} and C_{n2} from the raw data (C_{raw}) does not give the net fourfold coincidences, because the noise due to the detector dark counts has been subtracted twice. The fourfold coincidences (C_d) by disconnecting both sources from the 50:50 coupler is also measured, and added C_d

induced fourfold counts back to obtain the net fourfold coincidences. To understand this process, here is an example: a raw fourfold coincidence counts C_{raw} at a particular delay δt is measured first. The multi-pair noise contribution from two sources and the detector dark counts contribution to C_{raw} at delay δt are measured separately and counted as C_{n1}, C_{n2} and C_d, respectively. The corrected net fourfold coincidence equals to $C_{raw} - C_{n1} - C_{n2} + C_d$. The correction is implemented for all delays shown in Figure 3.10. The corrected fourfold coincidence measurements show a visibility of 91±8% indicated by a Gaussian fit, as shown in Figure 3.11. It clearly demonstrates that the multiplexed photons are highly indistinguishable. This non-100% visibility is due to the photons' spectral distinguishability introduced by the slightly broader band filtering of the photons mentioned earlier.

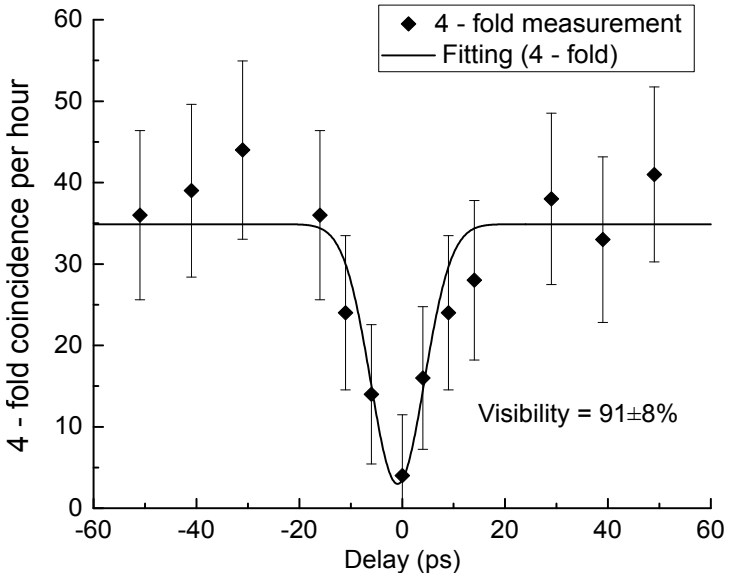

FIGURE 3.11: Fourfold quantum interference after subtracting multi-photon noise. Poisson error bars are used for plot, see Equation (2.36). Solid lines are Gaussian fits according the spectral filtering shape in the experiment.

The proof-of-principle results show TMUX is a promising strategy to significantly boost the generation efficiency of a heralded single-photon source. Thus, the remaining challenge is improving the source efficiency to at least 0.75 as explained in Section 2.2.5. If the generation efficiency is started from 0.015 (arbitrarily chosen to be $\ll 1$ to suppress multi-pair generation), using the first-order approximation (more rigorous and detailed analysis can be found in Ref. [205] and [110]), at least $N = 0.75/0.015 = 50$ time-bins are needed to be multiplexed if the switch circuit has negligible losses. The required number of switches is an integer no less than $\log_2 N + 1$, which is 7. Using seven switches, the number of multiplexed time-bins is $2^{(7-1)} = 64$. As this number is larger than the required $N = 50$, and the probability of generating more than one pair in 64 time-bins is low since $0.015 < 1/64$, it is possible to achieve the required generation efficiency ($\mu \geq 0.75$). The major challenge is to reduce the losses of switches. Recent development of stress-optic effect based switches has the potential to bring the

switching losses down to the desired level [206]. This type of switch has a 2 µm thick lead zirconate titanate (PZT) film on the top of a very low loss (as low as 0.0005 dB/cm) Si_3N_4 waveguide [206]. The applied stress has nearly no impact on the loss and thus the switch can be practically lossless if the switches and delay lines are integrated on the same chip to avoid waveguide-fibre coupling.

The other challenge involved in developing high performance heralded single-photon sources is to have pure heralded single-photon sources before MUX so that the photons after MUX are highly indistinguishable. In this proof-of-principle demonstration, the interplay between pump bandwidth and phase matching dictates that purity is maximised with sufficiently narrow filter bandwidths. In the future, heralded photon purity can be enhanced by either engineering the dispersion of the photon pair source or employing micro-ring resonators as the nonlinear device [104, 106, 207, 208].

3.2.4 Conclusion

This proof-of-principle demonstration provides a road map for creating high-efficiency heralded single-photon sources using a resource efficient and thus scalable TMUX scheme. With nearly unity efficiency detectors, 90% transmission filters and low-loss switches, ATM scheme provides a potential solution to build a high-efficiency single-photon source required for large-scale photonic quantum computing.

Contribution

Dr. Chunle Xiong proposed this project. Dr. Chunle Xiong, Dr. Matthew J. Collins, Prof. Philip H. W. Leong, and Prof. Benjamin J. Eggleton discussed the feasibility. Dr. Chunle Xiong designed the experiment, with the assistance from Dr. Matthew J. Collins who proposed the switching architecture. I set up the experiment, took the data, and analysed the data under Dr. Chunle Xiong and Prof. Benjamin J. Eggleton's supervision. Prof. Zhenyu Liu, Dr. Andri Mahendra, and Prof. Philip H. W. Leong designed the FPGA circuits and interface with other components. Dr. Duk-Yong Choi and Dr. Chang Joon Chae provided the silicon nanowire. Dr. Luke G. Helt. and Prof. Michael J. Steel provided theory insight of the measurements.

3.3 Time and wavelength division multiplexing

This section explains an alternative TMUX scheme that involves time and wavelength simultaneously. Three parts are included in this section.

3.3.1 Motivation and principle

Compared with SMUX scheme, TMUX scheme can significantly reduce the number of nonlinear mediums, optical switches and only requires one single-photon detector for heralding decision. This scheme relies on the heralding detector not

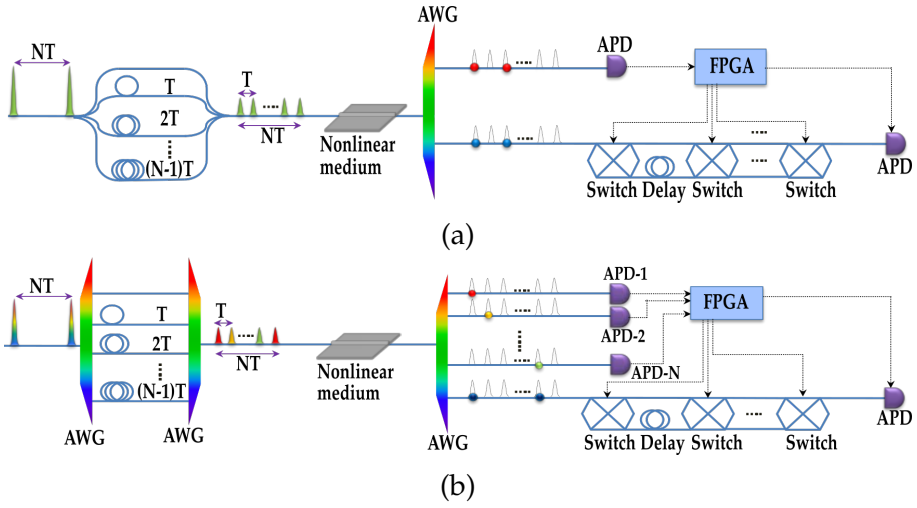

FIGURE 3.12: The schematic of ATM(a) and TWDM(b). (a) Green pulses are pump pulses; AWG: array waveguide grating; APD: avalanche photodiode; FPGA: field-programmable gate array. (b) Colourful pulses indicate broadband spectrum of pump pulses.

being saturated by the high rate of generated photons. Once the heralding detector is saturated, it is impossible to obtain the correct temporal information of each heralding photon which is the key to implement TMUX. Benefit from superconducting technologies, the saturation rate of superconducting single-photon detector has been extended to more than hundreds of megahertz so that the heralding channel has a large saturation margin [209]. However, the cryogenic condition requires a complicated system which is not always available in a practical circumstance. In this situation, avalanche photodiode is another cost-efficient solution for the heralding detection, but, the heralding channel can be easily saturated due to the long deadtime in avalanche photodiode that severely limits the saturation rate. To overcome this practical challenge, TWDM is proposed as an alternative scheme that instead of reusing one avalanche photodiode, the heralding photons are equally generated in multiple-wavelength so that the saturation rate is linearly extended with the number of heralding channels.

The schematic of ATM and TWDM are illustrated in Figure 3.12(a) and Figure 3.12(b), respectively. In Figure 3.12(a), the light green pulses are pump pulses with narrow spectrum and have a period of NT. Using two 1-to-N couplers and optical delay lines with a delay of $0, T, 2T, \ldots, (N-1)T$, the period of the pump pulses becomes T, and the repetition rate R is increased by N times. If the μ of each pump pulse is the same, the heralded single-photon rate will increase by N times with a lossless switching network. After the nonlinear medium, correlated photon pairs are randomly generated in any pump pulses and the heralding photons (red) are detected by an avalanche photodiode (APD). A field-programmable gate array (FPGA) controls the switching network to shift heralded photons (blue) based on the temporal information of heralding photons. However, only one APD is used for the heralding detection and it can easily be saturated if a large amount of temporal modes are multiplexed. Figure 3.12(b)

presents the differences between ATM and TWDM, colourful pump pulses indicate a broadband spectrum and N wavelengths are filtered and selected by two array waveguide gratings (AWGs). The optical delay lines between two AWGs increase the pump rate to N as in the ATM scheme. After the nonlinear medium, correlated photon pairs are spatially separated and filtered into multiple channels by an AWG. Since each pump pulse is centred at different wavelengths and the frequency of heralded photons is fixed by a well-defined AWG channel, the heralding photons (red, yellow and green) are generated at different frequencies due to the phase matching and energy conservation. N APDs are used to detect the distributed heralding photons, so that the saturation rate is linearly extended by the number of heralding channels in this scheme.

3.3.2 Coincidence measurements

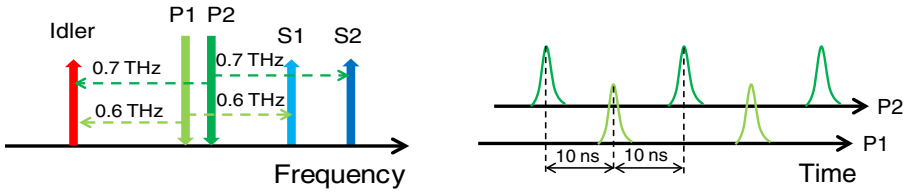

(a) (b)

FIGURE 3.13: (a) Wavelength division multiplexing of two pumps separated by 0.1 THz. (b) Time division multiplexing of two pumps: the original period of both pumps is 20 ns, and P1 is delayed by 10 ns from P2.

To experimentally demonstrate the feasibility of the TWDM scheme, a proof-of-principle demonstration is set up for $N = 2$ as illustrated in Figure 3.14. The nonlinear medium is pumped with two time division multiplexed pulses, spectrally separated by 0.1 THz, as shown in Figure 3.13(a), Pump 1 (P1, lower frequency) and Pump 2 (P2, higher frequency), which are able to generate spectrally overlapped photons (Idler). In the experiment, the generated photon pairs from P1 are post-selected at 0.6 THz detuning from P1, and those photon pairs generated from P2 are post-selected at 0.7 THz detuning from P2. The idler photons generated from the two pumps are therefore at the same frequency. Each individual pump have a pulse period of 20 ns, and one is delayed by 10 ns to the other to form a time division multiplexed pulse train, as shown in Figure 3.13(b), so that the idler photons from each pump are heralded by their corresponding signal photons. Compared with the experiment using only one pump with 20 ns period, this scheme is equivalent to doubling the pump repetition rate and will therefore enhance the heralded single-photon rate without reducing the CAR.

The experimental setup is shown in Figure 3.14. Two external cavity diode lasers (ECDLs) are used to emit two pumps separated by 0.1 THz (1,550.12 nm and 1,550.92 nm respectively). After going through polarisation controller (PC), they are combined by a 50:50 fibre coupler (FC) and modulated by a single lithium

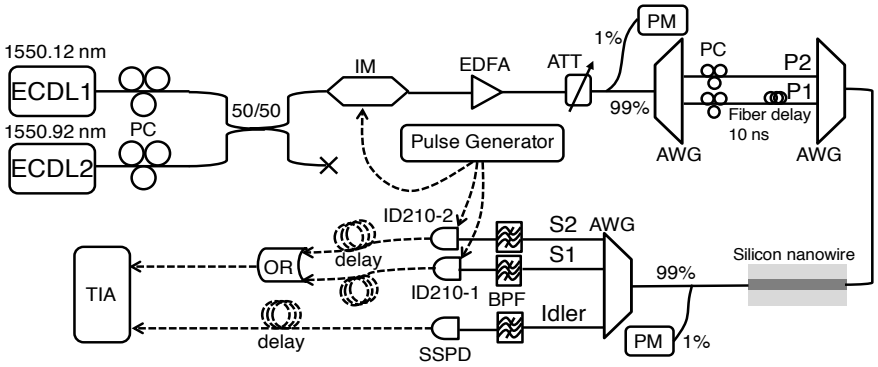

FIGURE 3.14: Experimental setup. ECDL: external cavity diode laser, PC: polarisation controller, IM: intensity modulator, EDFA: erbium doped fibre amplifier, ATT: attenuator, PM: power meter, AWG: arrayed waveguide grating, BPF: band pass filter, SSPD: superconducting single-photon detector, and TIA: time interval analyser. Solid and dashed lines represent fibre and electronic connections, respectively.

niobate intensity modulator (IM). The IM is driven by a pulse generator that produces 250 ps wide Gaussian pulses at 50 MHz repetition rate. The two pumps are then amplified by an erbium doped fibre amplifier (EDFA). They are separated using an array waveguide grating (AWG) from JDS Uniphase (100 GHz channel spacing and 50 GHz channel bandwidth). P1 is subsequently delayed by 10 ns, corresponding to half of the modulation period. After being recombined using another AWG, two pumps are injected into a 3 mm silicon nanowire. As explained in Section 2.4.2, the TE mode in the silicon nanowire not only allows 3 dB/cm propagation loss, but also exhibits anomalous dispersion in the telecom band. The total insertion loss of the nanowire is as low as 5 dB for the TE mode because of the use of inversed tapers and lensed fibres. PCs are placed in the two pump channels between the two AWGs to adjust the pump polarisation independently so that both pumps are TE polarised in the nanowire. The two AWGs also play the role of filters to get rid of amplified spontaneous emission (ASE) noise from the EDFA as well as any possible SpRS noise from the connection fibres before them. A tunable attenuator (ATT), 1:99 FCs and power meter are used along the optical circuit to control and monitor the pump power. At the output of the nanowire S1 (generated by P1), S2 (generated by P2), and idler photons are separated using the third AWG and further filtered by band pass filter (BPF). The total loss of the AWG and the BPF is approximately 4.5 dB. The two channels carrying S1 and S2 photons are sent to InGaAs avalanche photodiodes (APDs: ID210, ID-Quantique, 25% efficiency, 1 ns effective gate width, 20 µs deadtime, gated at 50 MHz by the pulse generator, 1 kHz dark counts), and the idler photons are sent to a superconducting single-photon detector (SSPD: Single Quantum, 10% efficiency with 100 Hz dark counts). In this configuration, the detection of the signal photons generated from both pumps could herald the arrival of an idler photon. The detection signals from the two ID210 detectors are sent to an OR gate. The output of the OR gate and the detection signal of the SSPD are both sent to a time interval analyser (TIA) for coincidence measurements. The internal

tunable trigger delay of the ID210 is used to align the gate pulses and the optical pulses. Tunable electronic delays after detection are used to shift the coincidence peak in the histogram away from zero delay to avoid any loss of counts.

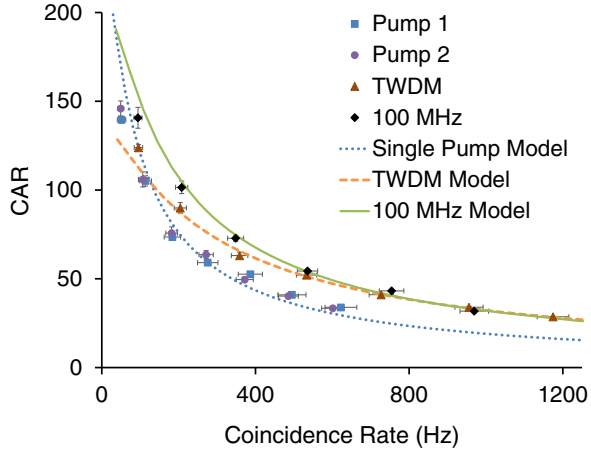

FIGURE 3.15: Measured CAR as a function of true coincidence rate. Blue squares and purple circles represent the results with only P1 or P2 turned on, respectively; brown triangles represent the TWDM results. Measurements with only one pump at 100 MHz are shown for comparison (black diamonds). The measurement beyond 950 Hz coincidence rate for the 100 MHz pump could not be done because of the detector saturation. The dotted blue, dashed orange, and solid green lines represent analytical models based on experimental parameters for a single pump, TWDM, and 100 MHz pump, respectively. Poissonian error bars are included, see Equation (2.36).

To show the enhancement of TWDM scheme, the CAR and coincidence rate are measured at different input power levels. As a reference, the CAR and coincidence rate are collected with only P1 or P2 turned on, each operating at 50 MHz. TWDM scheme is measured at the same conditions. The results are plotted in Figure 3.15 as brown triangles, which show a coincidence rate (i.e., heralded single-photon rate) improvement of $90 \pm 5\%$, with a decrease of $14 \pm 2\%$ in CAR. In the single pump measurements (blue squares and purple circles), increasing the coincidence rate by the same amount would typically reduce the CAR by 40%, as the result of multi-pair generation with increased pump power.

To compare the performance of this TWDM scheme with that of simply doubling the repetition rate of a single pump wavelength, a single pump experiment operating at 100 MHz is performed. The results are plotted in Figure 3.15 as black diamonds. The two sets of experimental results almost overlap at high power, showing that the TWDM source offers a similar performance in this power range. However, the CAR in the TWDM experiment is lower than that in the single pump experiment at low power. This part of deviation is attributed to the cross-talk between the photons generated from two pumps and different dark count rates for these two measurements due to the inherent differences in triggering the ID210 detectors.

Ideally, this TWDM source should offer 100% enhancement to the heralded single-photon rate without reducing the CAR, because the two pumps are not

temporally overlapped and should behave like pumping the nanowire independently. In reality, however, the ID210 detectors used to detect signal photons are gated by their pumps, and the effective gate pulse width has to be no less than 1 ns to get reasonable counts. Even though the 1 ns gate width is much less than the 10 ns separation between the multiplexed pulses, the detector synchronised to one pump could capture signal photons generated from the other pump. For example, when only external cavity diode laser1 (ECDL1) is switched on, the detector ID210-2 is not meant to have any counts beyond dark count. However, because P1 could also generate photons at the S2 wavelength and the gate pulses for ID210-2 are measured to have a small hump that is temporally overlapped with P1, some photon counts beyond dark counts is observed. These counts are collected by the TIA through the OR gate and contribute to accidentals because the S2 photons generated by P1 would not be correlated with the idler photons generated by P1. Similar noise increases when only ECDL2 is switched on. Therefore, when both lasers are switched on for the TWDM source, the two pump channels are not completely independent, but have cross-talk through the detectors because of a charge persistence effect introduced through imperfect gating [210]. When a large amount of photons are illuminated on an APD while the gate is OFF, there is still a probability to generate electrons in the active area of the APD because the gate pulse voltage is not actually zero. Once the gate is switched ON in a few ns, these electrons will generate electrical pulses and give some counts. In the low power regime, because the true photon rate is low and therefore is very sensitive to noise, the cross-talk noise affects the CAR more significantly than in the high power regime. This explains why the two plots overlap at high power, but diverge at low power.

The benefit of this TWDM scheme is to avoid the APD saturation introduced by the detector deadtime. As the deadtime of the detectors in this experiment is set to 20 µs to reduce the afterpulsing noise, the maximum count rate allowed by this deadtime is 50 kHz. The maximum measurable coincidence rate is limited to 950 Hz when using a single pump with 100 MHz repetition rate (see Figure 3.15). The ratio of $950/50,000$ corresponded to the 17 dB loss in the heralded (idler) channel. In contrast, the coincidence rate of TWDM is nearly 1,200 Hz (see Figure 3.15), breaking the limit by distributing the heralding photons to multiple wavelength channels. The detector for the idler channel in the experiment is a SSPD with a deadtime of only tens of nanoseconds and thus do not have a saturation problem. The reason of using the SSPD here for the idler channel is because only two APDs are available at the moment. In the case that an APD is used for the idler channel, one can use the output of the OR gate from the heralding channels to trigger the APD and avoid saturation, as shown in Figure 3.12(b).

As an alternative approach of ATM, this TWDM scheme for silicon nanowire based heralded photon sources can be scaled up once the imperfect gating issue is solved. One solution is to make the gate pulse voltage as close to zero as possible when the gate is OFF. To make full use of the SFWM bandwidth, AWGs with 50 GHz channel spacing and 25 GHz channel bandwidth will be required to multiplex more wavelength channels. Such AWGs are commercially available, and for telecom C-band wavelengths, there are 80 channels. This allows for scaling

the TWDM scheme up to 14 pumps before the pumps are too close to the photon channels and will cause contamination. The SFWM bandwidth required for MUX 14 pumps is only 2 THz, well within the bandwidth of SFWM provided by the silicon nanowire, as explained in Section 2.4.2.

In this work, $90 \pm 5\%$ photon statistic enhancement of the TWDM is experimentally demonstrated at the cost of only $14 \pm 2\%$ reduction to CAR. The drop in CAR at low power is due to the cross-talk between the two pumps when using them to trigger the APDs. This cross-talk is caused by imperfect detector gating, which is not an intrinsic problem to this TWDM scheme. Most importantly, as heralding photons generated by different pumps are detected with separate APDs, the heralded single-photon rate will be linearly enhanced with the number of pump wavelengths. To build a useful single-photon source, enhancing single-photon generation efficiency is not sufficient since its potential applications require high-efficiency and indistinguishability simultaneously. Thereby, the indistinguishability of heralded single photons generated from different pump wavelengths are verified in Section 3.3.3.

3.3.3 Indistinguishability verification

The enhanced heralded single-photon rate demonstrated in previous section does not necessarily indicate that these single photons are indistinguishable from one another. A rigorous verification, such as HOM quantum interference, is required to prove the indistinguishability of heralded photons generated from different pump wavelengths. To implement this verification, two nominally identical silicon nanowires are pumped at different wavelengths and HOM interference is implemented between the heralded photons from each source. An alternative choice is pumping one silicon nanowire with different pump wavelength and verifying the indistinguihability of heralded photons generated from different pump pulses and at different times. This would require splitting the heralded photon channel into two and relying on post-selection to overlap them in time for the HOM interference, so here two silicon nanowires are used in the measurement. The TWDM scheme requires the source have broadband SFWM so that the probability of creating heralded photons at a particular wavelength is similar for different pump wavelengths. Two silicon nanowires used in this work have been explained in Section 2.4.2. The TE mode of silicon nanowires exhibits 12 THz FWHM of SFWM, potentially allowing for a large number of wavelength channels using standard telecom components.

The experimental setup is shown in Figure 3.16. The pump wavelengths of source A and B are selected at 1,554.94 nm and 1,555.74 nm, respectively. A standard telecommunication Gaussian-shaped array waveguide grating (AWG) and tunable band pass filters (BPFs) with a bandwidth of 0.4 nm and 0.8 nm, respectively, are used to separate two pump wavelengths from the same 50 MHz mode-locked laser (MLL) (original bandwidth 8 nm), then the pump wavelengths are recombined and amplified in the same erbium doped fibre amplifier (EDFA). The pump wavelengths are separated again with an AWG and sent to the two silicon nanowires, with optical delay lines (ODLs) to control the arrival times of the generated photons. Lensed fibres are used to couple to the silicon nanowires,

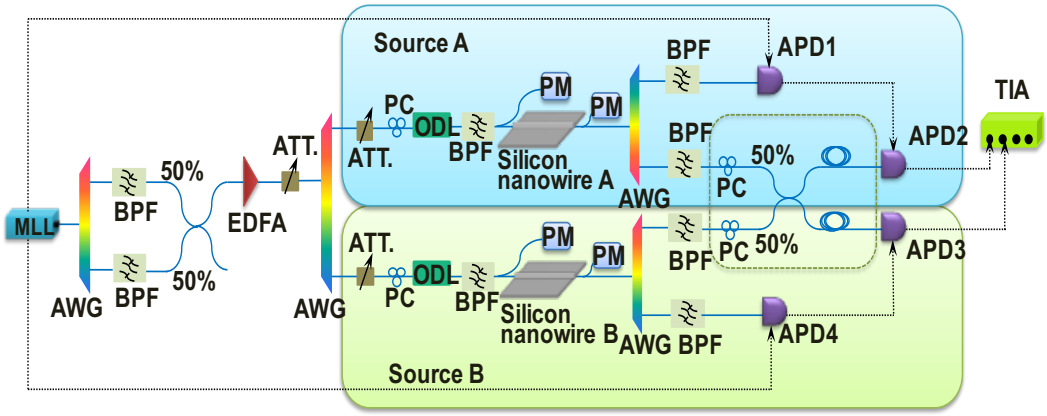

FIGURE 3.16: Experimental setup. MLL: mode-locked laser; BPF: band pass filter; EDFA: erbium doped fibre amplifier; ATT: attenuator; AWG: array waveguide grating; ODL: optical delay line; PM: power meter. APD: avalanche photodiode; TIA: time interval analyser; PC: polarisation controller; The PC, 50:50 coupler and additional fibre before APD2 and APD3 are only for the HOM quantum interference, and are removed for the initial characterisation of the sources.

which have inverse tapers on each end to further reduce the mode area mismatch between the fibre and nanowire. The average coupling loss of each facet is 2.5-3 dB. Polarisation controllers (PCs) before the nanowire are used to adjust the mode of pump wavelength. Correlated photon pairs from each nanowire are split into signal and idler channels by a Gaussian shaped AWG and filtered by a BPF with 3 and 2 dB insertion loss, respectively. The signal and idler wavelengths from source A are 1,549.32 nm and 1,560.60 nm, respectively. In source B, the wavelengths of signal and idler are 1,550.92 nm and 1,560.60 nm, respectively. The signal photons (1,549.32 nm) generated in source A are detected by avalanche photodiode (APD1) and the signal photons (1,550.92 nm) generated in source B are detected by APD4. The idler photon (1,560.60 nm) generated from sources A and B are detected by APD2 and APD3. The additional fibres before APD2 and APD3 behave as buffers, guaranteeing the heralded photons arrive at the detectors at the time when it is triggered by the heralding signals. The APDs are Id Quantique InGaAs ID210, with the detection efficiencies set to 25%, the deadtime set to 10 µs, and the effective gate width equals to 1 ns. The total loss in each channel is around 15 dB, or 3.2% overall efficiency for each photon.

Before implementing HOM interference, both sources are characterised in terms of the CAR as the pump power is varied. For the CAR measurement, idler photons from each source are sent directly to the APDs without the 50:50 coupler shown in Figure 3.16. Here, all four APDs are triggered by the electronic output of MLL, and a time interval analyser (TIA) is used to record the coincidence rate and the accidental rate for each source. The CAR measurement results are plotted in Figure 3.17. The data points of source A and B are very close to each other, which indicates the two sources are well balanced in brightness and CAR. They are both in good agreement with analytical results using Equation (2.38), shown

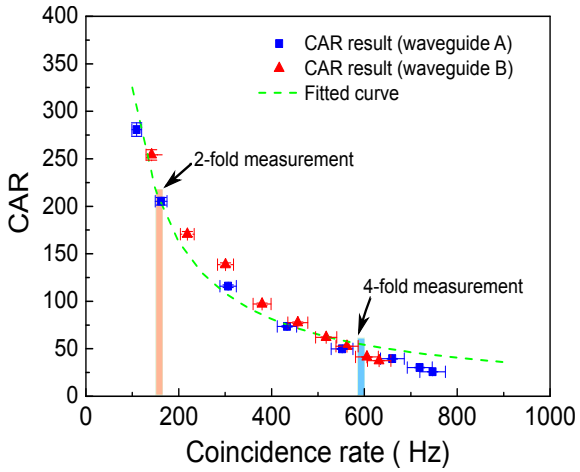

FIGURE 3.17: CAR vs coincidence rate. Blue rectangles: CAR measurement results in waveguide A; red triangles: CAR measurement results in waveguide B; green dashed line: analytical plot. Light red bar shows the experimental condition of twofold (2-fold) HOM dip measurement, and light blue bar points the experimental condition of the fourfold (4-fold) HOM dip measurement. Poisson error bars are used for plot, see Equation (2.36).

by the green dashed line. The analytical curve is higher than the experimental results when the coincidence rate is more than 600 Hz, which is caused by the 10 µs deadtime of the APDs at high count rates. As the detected photon rate increases, there is more chance that a photon will arrive during the deadtime created by a previous detection. This effectively leads to a drop in detector efficiency.

After characterising these two sources, twofold and fourfold HOM quantum interference measurements are implemented. In the HOM dip measurements, idler photon are transmitted into a single 50:50 coupler via polarisation controllers (PCs), which are used to match their polarisation. In the twofold HOM dip measurement, only two detectors (APD2 and APD3) are used, and are triggered by the MLL clock. The average power is set at 100 µW so that the coincidence rate is 156 Hz and CAR is 205, as indicated by the red bar in Figure 3.17. Coincidences are accumulated for 4 minutes per data point, and the relative delay is varied using the ODL connected in source A. Based on a Gaussian function, the twofold fitted curve in Figure 3.18 shows $33 \pm 4\%$ visibility, close to the theoretical limit of one third [74]. In the fourfold experiment, the count rate is much lower than in the twofold case, because of the transmission loss and detector efficiency. Hence, the pump power of each source is doubled in order to increase the counts rate to around 600 Hz, as indicated by the blue bar in Figure 3.17. The measurement time per data point is also increased to 105 minutes. In the fourfold HOM dip measurement, all four detectors are used, with APD2 and APD3 triggered by heralding photon detection from APD1 and APD4. The experiment results for the fourfold HOM dip are shown in the Figure 3.18 with a Gaussian fitted curve of $88 \pm 8\%$ visibility, without subtracting any noises. Here, the ideal maximum visibility should be 100% if there is no any noises.

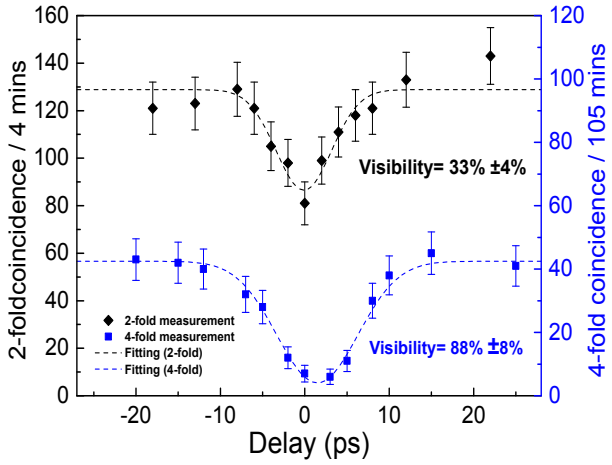

FIGURE 3.18: Twofold (2-fold) and fourfold (4-fold) HOM dip experimental results. Black diamonds: twofold experimental result; black dash line: fitted curve using a Gaussian function. Blue rectangles: fourfold experimental results; blue dash line: fitted curve using a Gaussian function.

The twofold HOM dip is a coincidence measurement between the interfering modes, but without heralding information. In this case, coincidence events arise from three cases: a single photon from each of source A and B; two photons generated in source A; and two photons generated in source B. When the two sources are well balanced in their average number of photon pairs per pulse (μ), the probabilities of the three cases all scale with μ^2, making the total coincidence events scale with $3\mu^2$. Only the case with one photon coming from each source can show HOM interference. Hence, the theoretical predication of the twofold HOM visibility is one third:

$$\frac{C_{Max} - C_{Min}}{C_{Max}} = \frac{3\mu^2 - 2\mu^2}{3\mu^2}, \tag{3.1}$$

where C_{Max} is the maximum coincidence rate which is seen away from the dip, and C_{Min} is the minimum coincidence rate, seen at the centre of the dip. The twofold HOM dip is a convenient method to find the exact delay at which the dip is positioned, because it can be carried out faster than the fourfold measurement. Here, the visibility is so close to the theoretical maximum that it gives us a good indication that the idler photons generated by different pump wavelengths are highly indistinguishable. However, fourfold HOM quantum interference requires that the heralding detectors be used, so that a single photon generated in each channel is identified for every coincidence. Hence, the fourfold experiment is a more rigorous demonstration of the quality of the sources.

For the fourfold measurement, only the cases with at least one photon from each channel remain, because of the heralding information. This includes the case with a single photon from each source, scaling with μ^2, which interfere perfectly.

The multi-photon contributions, which scale with μ^n(n$\geq$3), will degrade the visibility of HOM dip. Including only the terms of order μ^3, the theoretical visibility is expressed as [204]:

$$V = \frac{1+8\mu}{1+12\mu}. \tag{3.2}$$

This gives a theoretical value of HOM dip visibility $V = 94\%$ for the inferred $\mu = 0.02$ in the fourfold measurement. The $n \geq 3$ contributions are expected to be negligible. Another potential error source comes from residual spectral correlations between the signal and idler of a pair (which can reduce the visibility), but these should be avoided by the use of narrow spectral filtering on all of channels in the experiment. The experimental visibility of $88 \pm 8\%$ is within the error of this theoretical value (the error is based on the Poissonian statistic of the count rates, see Equation (2.36)). This result demonstrates that non-classical single-photon interference indeed takes place between two heralded single photons generated from different pump wavelengths, as the HOM dip visibility far exceeds the classical limit of 50%.

3.3.4 Conclusion

In this section, TWDM scheme is proposed as an alternative ATM scheme to overcome the potential saturation in the heralding channel if superconducting single-photon detector is not available in practical circumstance. The coincidence measurements show $90 \pm 5\%$ photon rate enhancement at the cost of only $14 \pm 2\%$ reduction to CAR. The drop in CAR is mainly attributed to the cross-talk between pump pulses which is resulted from a non-zero gating rather than an intrinsic barrier. $88 \pm 8\%$ visibility of HOM quantum interference indicates the indistinguishability of heralded single photons generated via TWDM scheme. These experimental results demonstrate that TWDM is another potential solution to build a high-efficiency single-photon source for large-scale photonic quantum computing

Contribution

I set up the experiment, took the data, and analysed the data under Dr. Chunle Xiong, Dr. Bryn A. Bell and Prof. Benjamin J. Eggleton's supervision. Mr. Runyu Jiang, Mr. Iman Jizan and Dr. Jiakun He offered technical support. Dr. Alex S. Clark provided theory insight of the measurements. Dr. Duk-Yong Choi and Dr. Chang Joon Chae provided the silicon nanowire.

3.4 Relative temporal multiplexing

This section explains the principle of RTM scheme as well as a proof-of-principle demonstration at two-photon level.

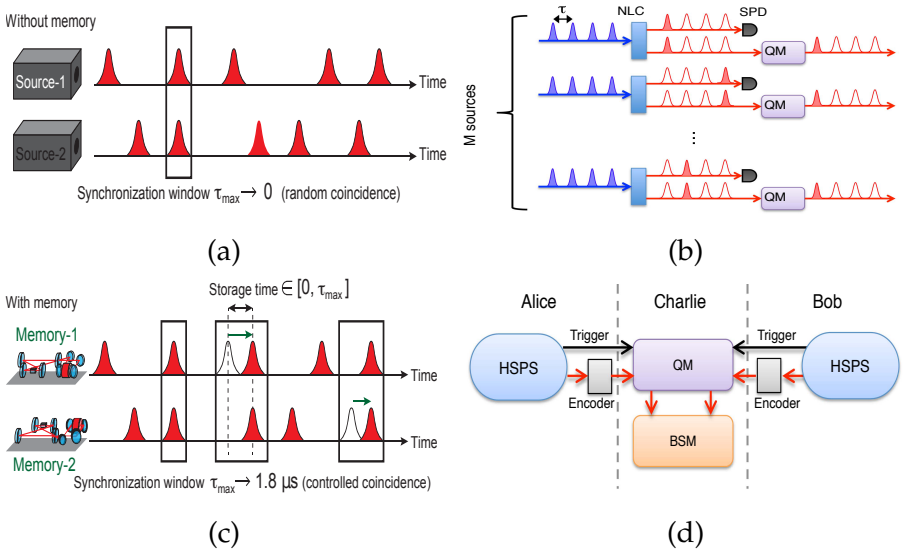

FIGURE 3.19: Experimental schemes of joint synchronisation using free space cavities as quantum memories [211, 212]. Photon synchronisation between two separate sources without (a) and with (c) cavity units [211]. Schematic of photon synchronisation between M sources (b) and quantum information processing harnesses quantum memory (d) [212].

3.4.1 Motivation

As explained in Section 2.2, N-photon is the basic requirement of large-scale photonic quantum computing. However, generating N-photon simultaneously from N non-deterministic single-photon sources is a formidable challenge, as the generation probability of N-photon being present simultaneously decreases exponentially with increasing photon number [89]. There are two strategies, independent and joint synchronisation, to generate N-photon from heralded single-photon sources. TMUX and TWDM explained in Section 3.2 and Section 3.3, respectively, are the instances of independent synchronisation strategy that builds a high-efficiency single-photon source first and then integrates N single-photon sources so that N-photon are passively appeared. The proof-of-principle demonstrations of TMUX and TWDM indicate these independent MUX (or standard temporal multiplexing (STM)) schemes are viable approaches to break the intrinsic limitation of nonlinear single-photon source. However, experimental efforts to date are still far from the deterministic regime, due to technical challenges, such as the loss incurred in delay lines and active switches. Compared with the independent strategy, the joint strategy directly generates N-photon by a joint synchronisation. Numbers of pioneer works that harness quantum memory or cold atomic ensembles demonstrate that the joint strategy can significantly enhance the N-photon generation efficiency [211–214], as partially shown in Figure 3.19. However, low-loss free-space cavities and cold atomic ensembles are not the optimal choices in terms of scalability and robustness. In a near future, photonic quantum computing will move out of the laboratory for practical applications. Using robust components, such as optical switches and fibres, to implement joint

synchronisation is a practical and cost-efficient approach.

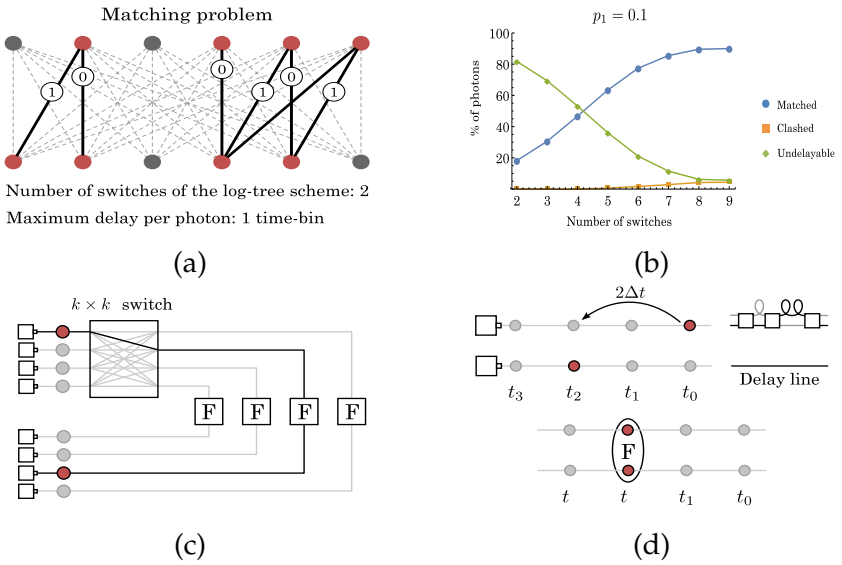

FIGURE 3.20: (a) Matching problem; Red circles are single photons; the dashed and solid lines are the virtual and available delays, respective. (b) Photon efficiency in RMUX scheme. (c) The schematic of RMUX in spatial domain. (d) The schematic of RMUX in time domain [215].

In 2017, M. Gimeno-Segovia et al. proposed a RMUX scheme which considers N-photon generation as a matching problem. In RMUX, heralded single photons are jointly synchronised via optical switches and delay fibres [111]. Figure 3.20(a) illustrates the synchronisation of two photon sources with one time-bin delay. The red circles, dashed and solid lines represent the single photons, virtual and available delays, respectively. The theoretical analysis of RMUX shown in Figure 3.20(b) clearly indicates its advantages that 10% generation efficiency only costs 6 optical switches to achieve more than 80% photon pairs synchronisation. The schematic of RMUX in spatial and temporal domain are presented in Figure 3.20(c) and Figure 3.20(d), respectively. Although the experimental implementations of spatial and temporal RMUX have distinct differences, they are conceptually similar with each other from a theoretical point of view. Both schemes operate numbers of non-deterministic process simultaneously and jointly synchronise heralded photons via an active switching network which is controlled by heralding information. The theoretical analysis of RTM is explained in Section 3.4.2.

3.4.2 Principle and analysis

To clearly illustrate the advantages of RTM over STM, the principle of STM scheme is firstly explained. In this scheme, N heralded single-photon sources are pumped by synchronised laser pulses separated by a period of T, which are grouped into time windows containing M laser pulses or time-bins. Figure 3.21(a) illustrates the principle of the scheme for the number of sources $N = 2$ (photon sources A and B) and time-bins $M = 4$ (time-bins are labelled as t_1 to t_4). Heralding

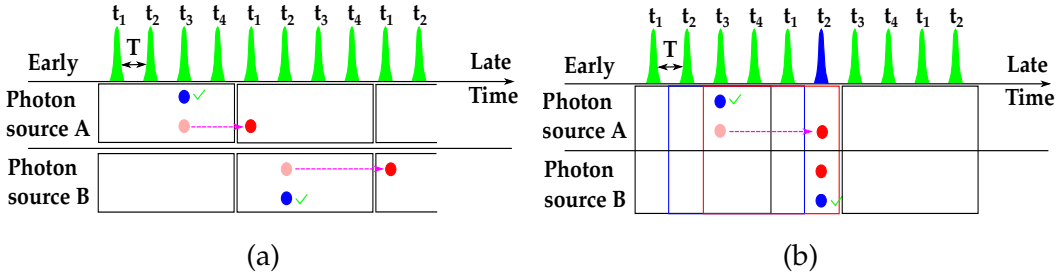

FIGURE 3.21: (a) The principle of the STM scheme. Laser pulses (green) define the time-bins with a period of T. The rectangles represent the time windows, each containing four time-bins. The blue circles are the heralding photons. The light red and red circles are the heralded photons before and after shifting, respectively. (b) The principle of the RTM1 scheme. The rectangles of different colours indicate the time windows being slid by T per step. The blue pulse indicates the time-bin of the output heralded photon pair.

photons (blue) are detected and their time-bin information is used to delay the heralded photons (red) to t_1 by actively configuring a delay line. The probability of generating single photons from one source per time window can be expressed as:

$$P_{source/window} = 1 - (1 - \mu)^M, \tag{3.3}$$

where μ is the probability of one source generating a heralded single photon in one time-bin. To avoid multi-photon noise, μ is limited to a trivial value in the experimental demonstration, $\mu \ll 1$. Thereby, Equation (3.3) can be expressed as:

$$P_{source/window} = M\mu. \tag{3.4}$$

Based on Equation (3.4), the probability of generating N-photon from N source per time window is:

$$P_{STM/window} = M^N \mu^N, \tag{3.5}$$

with a further assumption, $M\mu \ll 1$. Since each time window contains M time-bins, the probability of generating N-photon per time-bin can be expressed as:

$$P_{STM/time-bin} = M^N \mu^N / M = M^{N-1} \mu^N. \tag{3.6}$$

Multiplying this probability by the laser repetition rate (R) gives the N-photon generation rate in STM scheme.

Figure 3.21(b) depicts the principle of the RTM scheme using $N = 2$ photon sources and $M = 4$ time-bins. The time window (rectangle) is translated to begin at each time-bin. If all N-heralding photons (blue) are detected within one time window, the heralded photons (red) are delayed to align with the latest one; otherwise they are abandoned. The heralded photons are equally likely to appear in any time-bin and the sliding window includes additional opportunities to generating N-photon, which would be otherwise ignored in the STM scheme

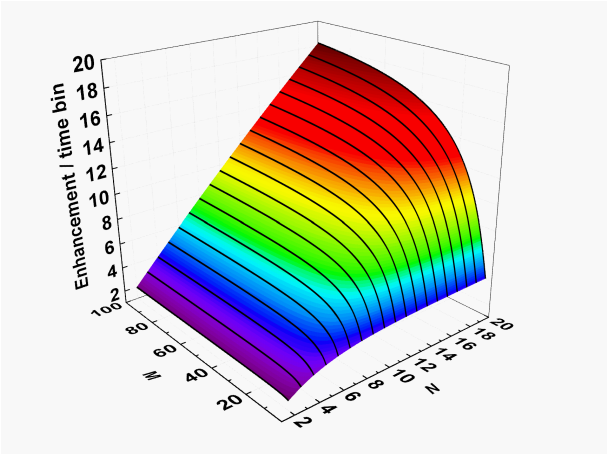

FIGURE 3.22: Enhancement between RTM1 and STM. M is the number of time-bins per time window and N is the number of photon sources included in the scheme

where heralded photons belong to different windows. With the same assumption, $M\mu \ll 1$, the probability of generating N-photon within one time window in RTM is given by Equation (3.5). To correctly find the probability per time-bin, the events of N-photon where no single photon originates from the latest time-bin of the time window should be excluded from Equation (3.5), since these events already have been synchronised by an earlier window. The events to exclude are the ones where N-photon occur in the first $M-1$ time-bins of a time window, which occur with the probability of $(M-1)^N\mu^N$. This probability holds in the limit of small $M\mu$ and this part should be subtracted from the total probability per time window to give the probability of generating N-photon per time-bin in RTM

$$P_{RTM1/time-bin} = M^N\mu^N - (M-1)^N\mu^N. \tag{3.7}$$

Moreover, less demand is placed on the speed of the switches, as they are only triggered by the detection of N-heralding photons within one time window, rather than for every single heralding photon. Here, RTM1 represents the first of two strategies for RTM in this proof-of-concept demonstration. Another strategy, RTM2, is explained in the following section. The enhancement ratio between RTM1 and STM can be expressed as

$$P_{RTM1/time-bin}/P_{STM/time-bin} = (M^N - (M-1)^N)/M^{N-1}. \tag{3.8}$$

and a plot of Equation (3.8) for different values of M and N is shown in Figure 3.22. The maximum value of additional enhancement increases with N, so this scheme could be highly beneficial in large-scale photonic quantum computing.

3.4.3 Experimental setup

Figure 3.23 illustrates the experimental setup. 10 ps optical pulses (green pulses) are emitted from a 10 MHz mode-locked laser (MLL) at a central wavelength

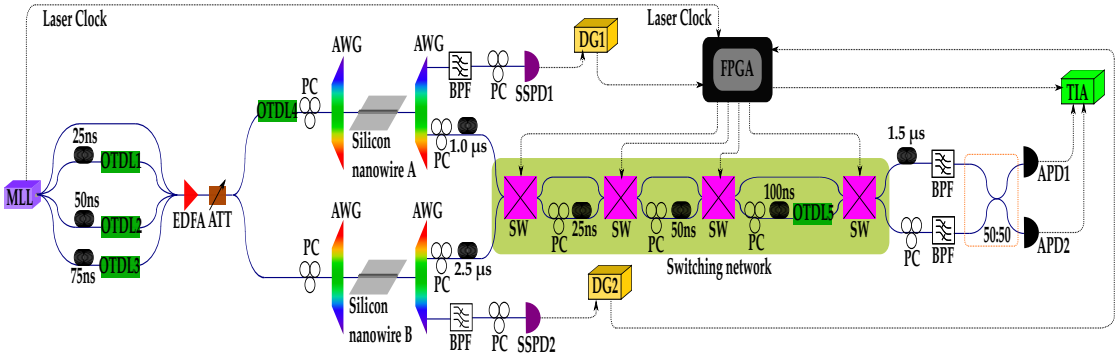

FIGURE 3.23: Experimental setup. MLL: mode-locked laser, PC: polarisation controller, OTDL: optical tunable delay line, EDFA: erbium-doped fibre amplifier. ATT: attenuator, AWG: array waveguide grating, BPF: band pass filter, DG: delay generator, SSPD: superconducting single-photon detector, APD: avalanche photodiode, TIA: time interval analyser. SW: switch, Solid and dashed lines represent optical fibres and electronic cables, respectively.

of 1,555.7 nm. The period is reduced from 100 ns to 25 ns by splitting the pulse into four paths; with separate delay fibres and optical tunable delay lines (OTDLs) between recombining the paths at a 1-to-4 directional coupler. The erbium doped fibre amplifier (EDFA) amplifies the 40 MHz pump pulses and the average pump power applied on two nominally identical silicon nanowires are controlled by the attenuator (ATT) before the array waveguide grating (AWG). Two silicon nanowires (3 mm long) explained in Section 2.4.2 are simultaneously pumped to generate correlated photon pairs in random time-bins via SFWM. The insertion loss of each silicon nanowire is around 6 dB. Two Gaussian shaped AWGs with 0.4 nm bandwidth and 3 dB insertion loss are used to spatially separate photon pairs generated at 1,550.9 nm and 1,560.5 nm and to block the pump laser. The pump photons are further suppressed by a band pass filter (BPF) with 0.5 nm bandwidth and 2 dB insertion loss. A polarisation controllers (PC) with 1 dB insertion loss is connected before superconducting single-photon detector (SSPD) to maximise the detection efficiency. After being detected by a SSPD with around 20% detection efficiency, the detection signals are shifted by a delay generator (DG: DG645 Stanford Research System) and their time-bin information is recognised by a field programmable gate array (FPGA). If heralding photons from both sources appear within one time window, the FPGA actively controls the switching network to synchronise these two heralded photons. Meanwhile, it sends a heralding signal at the time-bin of the heralded photon pair to the time interval analyser (TIA).

The switching network contains four ceramic switches and it is shared by the two sources, using additional fibres before the first switch to introduce 1 µs and 2.5 µs delay for source A and B, respectively. Each ceramic switch has 1-2 dB insertion loss and the additional delay fibre introduces 2-3 dB loss, mainly due to connector losses, since it is built from separate fibres. These buffer fibres guarantee the heralded photons from two sources are well separated when they pass through the switches. Thus, the switches can be configured independently for

heralded photons from different sources. A 1.5 µs delay (2-3 dB loss) after the switching network compensates the difference in time delay between the two heralded channels. The OTDL in the switching network adds 2 dB loss into the heralded channels. The 50:50 coupler is only used for a HOM quantum interference measurement. Heralded photons are finally detected by two avalanche photodiodes (APDs: ID210, Id-Quantique). The detection efficiency of each detector is set to 25%. The heralding signals from the FPGA and the detection of the heralded photon pair from APDs are collected by the TIA as the start and stop signal of fourfold coincidences, respectively. The overall collection efficiencies of heralding and heralded channel are around 17 and 28 dB, respectively. Nevertheless, the collection efficiency can be significantly improved with low loss components and high-efficiency detectors. Using separate switching networks for each source would also allow the additional delay fibres to be removed.

3.4.4 Experimental results and discussions

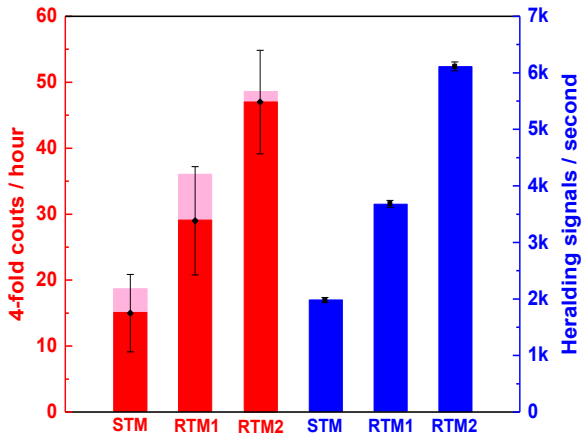

FIGURE 3.24: The pink and the red bars represent the raw and net fourfold (4-fold) coincidence counts in one hour, respectively. The blue bars represent the average heralding signal rate during the same measurement time. The error is based on the Poissonian statistics of the count rates, see Equation (2.36).

To experimentally demonstrate the additional enhancement of RTM, a fourfold coincidence measurement is implemented and the fourfold counts between the STM and RTM1 schemes are compared. Figure 3.24 summarises the measurement results in each scheme. With the same average pump power (0.52 mW), the fourfold coincidence counts of STM and RTM1 in one hour are 19 and 37, respectively, shown as pink bars in Figure 3.24. After subtracting uncorrelated noise, the net fourfold coincidence counts of STM and RTM1 are 15 and 29, respectively. The uncorrelated noise counts in RTM1 are higher than STM, because the heralded photon pairs are actively synchronised at any time-bin in RTM1 rather than a fixed time-bin (t_1) in STM so the APD must be triggered at 40 MHz rather than at 10 MHz. The enhancement ratio between STM and RTM1 is 1.95 ± 0.5, which is higher than, but within an error-bar of, the expected value of 1.75 calculated from

Equation (3.8). The large error margin results from the Poissonian statistics of the low count. In the future, the count rate can be improved by using high-efficiency single-photon detectors and low loss components [216]. Meanwhile, the heralding signal rate is also monitored during the measurement, shown as blue bars in Figure 3.24. The ratio between these two schemes, 1.86 ± 0.05, further confirms the additional enhancement in RTM, as the heralding signal rate is proportional to the generation rate of heralded photon pairs.

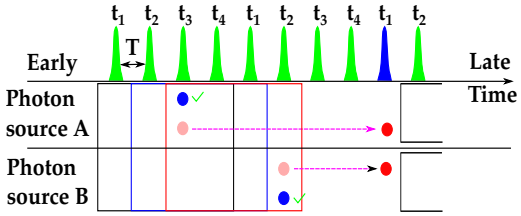

FIGURE 3.25: The principle of the RTM2. Laser pulses (green) define the time-bins with a period of T. The rectangles represent the time windows, each containing four time-bins. The blue circles are the heralding photons. The light red and red circles are the heralded photons before and after shifting, respectively. The blue pulse indicates the time-bin of the output heralded photon pair.

The indistinguishability of heralded photons is a crucial requirement for photonic quantum interference. It requires two heralded photons be synchronised to within a coherence length after the switching network, regardless of which time-bin they originate from. This is usually verified by HOM quantum interference [9]. The delay lines in the switching network are manually cut, making it challenging to control them with picosecond accuracy. In STM, such as ATM, the tiny deviation in these delay lines can be compensated by adjusting the timing of the pump pulses using the OTDLs before the sources, avoiding the additional loss of tunable delay lines in the single photon channels. However, the strategy of unevenly spaced pump pulses cannot result in perfectly synchronised photons in RTM since heralded photons can be shifted to any time-bin instead of a fixed one. This problem could be solved in integrated photonic circuits [13], where waveguides can be fabricated to provide precise delays. Here, a hybrid strategy of RTM is adopted that combines STM and RTM1 to verify the indistinguishability. In this hybrid strategy, heralded photons are first precisely shifted to the next t_1 time-bin, as in STM. Then RTM is applied between adjacent t_1 time-bins using the 100 ns delay in the switching network, as shown in Figure 3.25. The 100 ns delay in the switching network contains an OTDL so that the shifted photons remain indistinguishable, as shown in Figure 3.23. In the hybrid strategy (RTM2), the maximum time window has been extended from 75 ns to 175 ns so that additional heralded photon pairs can be synchronised in RTM2. The generation probability of N-photon state can be enhanced to three-fold compared with the STM scheme. Because it contains three combinations: the heralded photons appear within the same time window, a heralded photon from source A appears in the time window following one from source B, or a heralded photon from source B appears in the time window following one from source A. In a more

general scenario with N-photon sources, the probability of generating N-photon per MUX window is approximately expressed as:

$$P_{RTM2/window} = M^N \mu^N (2^N - 1). \tag{3.9}$$

Equation (3.9) also holds the same assumption, $M\mu \ll 1$. The probability per time-bin can be expressed as:

$$P_{RTM2/time-bin} = [M^N \mu^N (2^N - 1)]/M = M^{N-1} \mu^N (2^N - 1). \tag{3.10}$$

The additional enhancement between RTM2 and STM is expressed as:

$$P_{RTM2/time-bin} / P_{STM/time-bin} = (2^N - 1). \tag{3.11}$$

The net (raw) 4-fold coincidence counts in one hour is 47 (48) and the heralding signal rate is around 6 kHz, shown as RTM2 in Figure 3.24. The three-fold enhancement compared to STM is in good agreement with Equation (3.11).

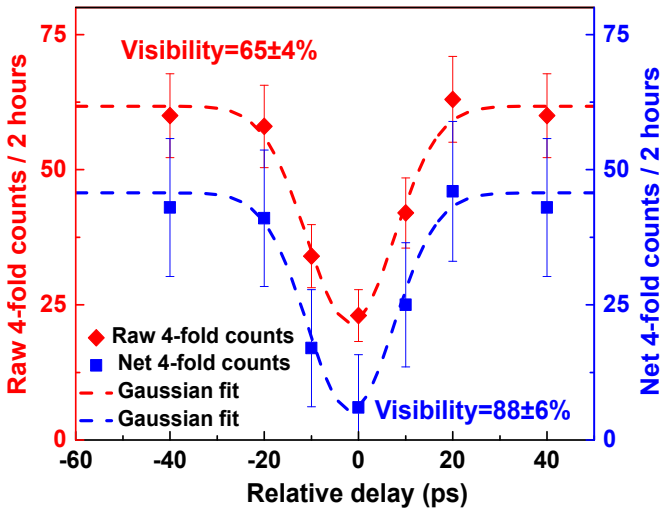

FIGURE 3.26: HOM quantum interference results. The red diamonds are the fourfold (4-fold) coincidence counts with noise, represented by the raw fourfold counts. The blue rectangles are the fourfold (4-fold) coincidence counts after subtracting noise counts, represented by the net fourfold counts. The dash line is Gaussian fit. Poisson error bar is used for plot, see Equation (2.36).

After matching the polarisations and precisely synchronising the heralded photons, as explained Appendix A.1.1 and A.1.2, respectively, a HOM quantum interference measurement is implemented. When the relative delay (t_R) between two heralded single photons is larger than the coherence time (10 ps), the fourfold coincidence count (red diamonds) measured in two hours is around 60. This value reduces to 23 when t_R is negligible. t_R is precisely controlled by the OTDL without changing the polarisation. In Figure 3.26, a $65 \pm 4\%$ interference visibility is estimated by a Gaussian fit to the fourfold coincidence measurement (red). Here, the visibility is relatively low due to the high multi-photon emission probability from each source. It is necessary to use high power in the experiment to

boost the counts rate because of the high losses. A lower pump power can be applied to reduce multi-photon noise if low loss components become available or even photon number resolving detectors can be used to discard multi-photons. The multi-photon noise from each source is experimentally measured with the method explained in Section 3.2.3. After subtracting this background, the HOM visibility is $88 \pm 6\%$, indicated by the Gaussian fit. This demonstrates that the heralded single photons are highly indistinguishable from each other, as it is far above the classical threshold of 50% and comparable to the HOM visibility when MUX is not used [217].

3.4.5 Conclusions

In this section, a RTM scheme is experimentally demonstrated and systematically analysed its benefits. The fourfold coincidence measurement and the quantum interference demonstrate that the RTM scheme can generate indistinguishable single photons with additional enhancement over STM without increasing the complexity, and the theoretical analysis indicates the additional enhancement will increase with the number of single-photon sources being multiplexed together. The fourfold count rate is low due to the high collection, filtering and detection losses of the single-photon sources, but this proof-of-principle demonstration clearly demonstrates the benefit of RTM over STM. The overall enhancement of RTM is also intrinsically determined by the number of switches and the loss of each switch [195, 199]. RTM greatly relaxes the speed requirement of the switches, which are only triggered for heralded N-photon instead of for each heralded single photon. This feature is a crucial advantage when μ is increased and large numbers of temporal modes are included in the time window, since fast, low-loss and low-noise switches are unavailable. Besides the additional enhancement and the relaxed switching requirement illustrated in the RTM scheme, the heralding signal can be used to further synchronise N-photon states generated from RTM. Future improvements, including the use of high-efficiency detectors or even photon-number-resolving detectors and the development of low-loss filters, are possible to much more efficiently produce N-photon states for large-scale photonic quantum computing.

Contribution

I set up the experiment, took the data, and analysed the data under Dr. Chunle Xiong, Dr. Bryn A. Bell and Prof. Benjamin J. Eggleton's supervision. Dr. Yeehui Lee and Prof. Philip H. W. Leong designed the FPGA circuits and interface with other components. Dr. Bryn A. Bell and Prof. Terry Rudolph provided theory insight of the measurements. Dr. Duk-Yong Choi and Dr. Chang Joon Chae provided the silicon nanowire.

3.5 High repetition rate limitation

This section considers potential limitations of TMUX with high repetition rate. The proof-of-principle demonstration shows the limitations and indicates the future improvements.

3.5.1 Motivation and analysis

As explained at the beginning of Section 3.1, TMUX is one of resource-efficient schemes to build a high-efficiency single-photon source over the SMUX, since only one nonlinear source and less optical switches are required for each single-photon output. Numbers of pioneer works indicate that TMUX is a viable approach to break the intrinsic limitations of the spontaneous nonlinear processes, such as SPDC and SFWM, so that each heralded single-photon source can efficiently generate indistinguishable single photons [66, 106, 197–199, 218]. Meanwhile, increasing the pump repetition rate applied in the TMUX scheme is a straightforward method to boost the single-photon rate linearly. Compared with <200 MHz pump source used in the proof-of-principle demonstrations [66, 106, 197–199, 218], the heralded single-photon rate could be enhanced 500-fold if a 100 GHz pump source is used in the experiment. A fundamental requirement of TMUX is correctly resolving the temporal information of heralded single photon which is predefined by the pump repetition rate. To date, it is not a challenge to correctly recognise the temporal information of each heralding single photon as the timing-jitter of the detection system is much smaller than 5 ns, the time interval of 200 MHz pump source. However, when the timing-jitter is comparable with or even larger than the time interval of pump pulses, the temporal information of each heralded photon cannot be correctly identified. In that case, it is infeasible to build a high-efficiency single-photon source via TMUX, since the heralded single photons are shifted to an incorrect time-bin instead of a fixed one, such as t_1. It is worthwhile to identify the potential limitations of TMUX with high repetition rate and an optimal repetition rate to build a high-efficiency single-photon source.

Instead of building a complicated TMUX system, the aforementioned potential limitations are explored by a series of coincidence measurement with a variable repetition rate. The details are explained in the following parts. Before the experimental investigations, a systematic analysis is implemented to predict the variation of correlated photon pair generation. C_{true} indicates the number of heralded single photons detected per second, excluding the level of accidental coincidences which would be present without any correlation. It can be calculated by:

$$C_{true} = \mu \eta_s \eta_i R, \tag{3.12}$$

where η_s and η_i are the collection efficiencies of signal and idler channels, respectively. Here, $\mu \propto (\gamma P_p L_{eff})^2$, with γ, P_p and L_{eff} the effective nonlinear coefficient, the peak power of the pump pulses and the effective length of silicon nanowire, respectively. Thereby, C_{true} is determined by P_p according to:

$$C_{true} \propto (\gamma P_p L_{eff})^2 \eta_s \eta_i R. \tag{3.13}$$

Equation (3.13) indicates that C_{true} quadratically increases with P_p and linearly increases with R. The CAR is effectively a SNR and in the absence of any background it can be expressed as:

$$CAR = 1/\mu, \tag{3.14}$$

as explained in Equation (2.39). In this case, CAR depends on P_p as:

$$CAR \propto 1/(\gamma P_p L_{eff})^2. \tag{3.15}$$

Equation (3.15) indicates that CAR is constant if the same P_p is applied to the nonlinear medium, regardless of R. After combining Equation (3.13) and Equation (3.15), the CAR can be expressed as:

$$CAR \propto \eta_s \eta_i R / C_{true}. \tag{3.16}$$

Equation (3.16) indicates C_{true} linearly increases with R without sacrificing CAR.

3.5.2 Experimental setup

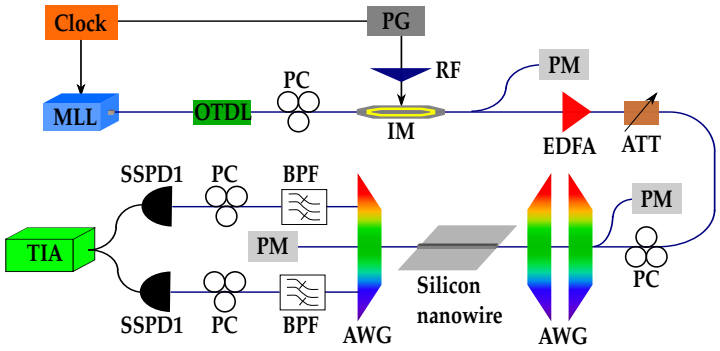

FIGURE 3.27: Experimental setup. MLL: mode-locked laser. Clock generates triggering signals. PG: pattern generator. RF: radio frequency amplifier. OTDL: optical tunable delay line. IM: intensity modulator. PM: power meter. EDFA: erbium doped fibre amplifier. ATT: tunable attenuator. PC: polarisation controller. AWG: arrayed waveguide grating. BPF: band pass filter. SSPD: super-conducting single-photon detector. TIA: time interval analyser. The blue and black lines are the optical fibres and the electronic cables, respectively.

Figure 3.27 is the experimental setup used in this work. An active mode-locked laser (MLL) is externally triggered at 10 GHz by a clock signal generator (Clock), and emits 10 ps pump pulses centred at 1,552.5 nm. The 10 GHz clock is also chopped by a pattern generator (PG) that adjusts R between 10 GHz and 156.25 MHz. The chopped clock signals control an intensity modulator (IM) after being amplified by a radio frequency (RF) amplifier. An optical tunable delay line

(OTDL) is used to align the pump pulses with the clock signal in the IM. A polarisation controller (PC) before the IM adjusts the polarisation of pump pulses to maximise the output power which is monitored by the power meter. The pump pulses are amplified by the erbium doped fibre amplifier (EDFA) and then the power is controlled by a tunable attenuator (ATT). The amplified spontaneous emission (ASE) noise originating from the EDFA is removed by two Gaussian shaped array waveguide grating (AWG), which have 0.4 nm FWHM and 0.8 dB insertion loss. The input power is monitored by another power meter via a 1:99 fibre coupler (FC) before the two AWGs. The length of the silicon nanowire is 3 mm, with a propagation loss of 3 dB/cm, resulting in an effective length 2.8 mm. The cross-section of this silicon nanowire is 220 × 460 nm. The insertion loss of this integrated silicon nanowire is 6 dB and it has 12 THz FWHM of SFWM for the TE mode, as explained in Section 2.4.2. The input polarisation is adjusted by a PC between the ATT and the two AWGs. Correlated photon pairs are randomly generated in the nanowire via SFWM. Signal and idler photons centred at 1,544.5 nm and 1,560.5 nm are spatially separated into two channels by another AWG. The spectrum of the signal and idler photons are further purified by band pass filters (BPFs) with a FWHM of 0.3 nm and 0.5 dB propagation loss, and then they are detected by a superconducting single-photon detector (SSPD) with 10% detection efficiency. The detector outputs are sent to a time interval analyser (TIA) for a coincidence analysis. The timing resolution of the TIA (PicoQuant, Hydraharp 400) used in the measurement is 1 ps.

3.5.3 Experimental results and discussions

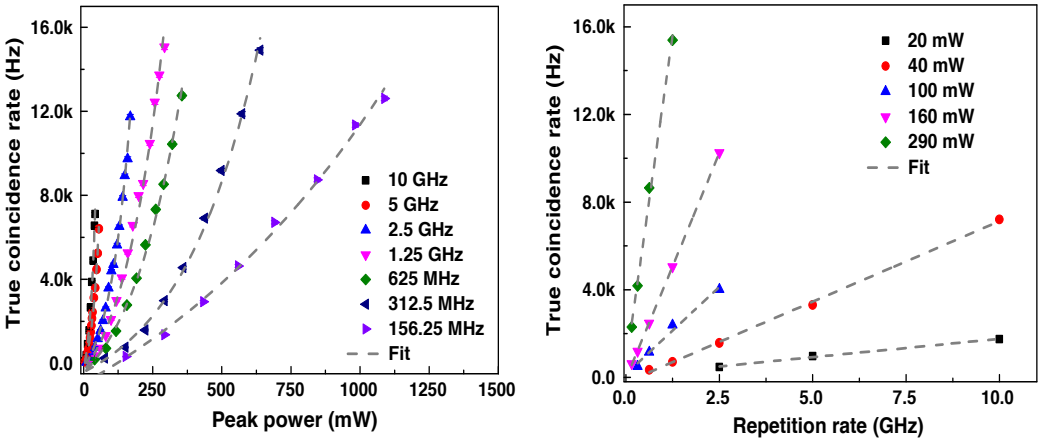

(a) (b)

FIGURE 3.28: Experimental results. (a) Summary of true coincidence rate at each R with quadratic fit lines. (b) The true coincidence rate as a function of R with fixed peak powers of pump pulses. The dashed lines are linear fits.

To systematically demonstrate the benefits and limitations of increasing R, seven different rates are created using the PG: 156.25 MHz, 312.5 MHz, 625 MHz, 1.25 GHz, 2.5 GHz, 5 GHz and 10 GHz. Figure 3.28(a) plots the C_{true} of each R as

a function of P_p. C_{true} is quadratically increasing with P_p and the highest C_{true} in Figure 3.28(a) is around 16 kHz when P_p of 1.25 GHz applied on the silicon nanowire approaches 0.29 W. This measurement result indicates that more than 20 MHz of correlated photon pairs are being generated in the nanowire, as described in Equation (3.12). The photon pair generation rate can be significantly enhanced by the ring resonator structure, and the optimal output can be obtained after overcoming coherent back scattering [219, 220] and dynamic thermal effect [221]. The detected photon rate is limited by the saturation rate of SSPDs. The saturation limit of SSPD can be elevated by splitting photons between multiple detectors. Figure 3.28(b) shows that C_{true} depends linearly on R, consistent with Equation (3.13). The linear variation confirms that C_{true} can be significantly enhanced by simply increasing R.

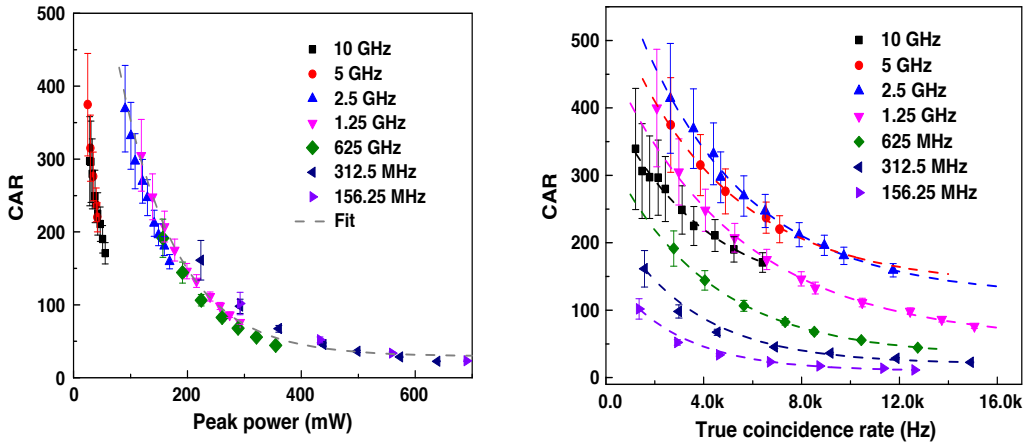

(a) (b)

FIGURE 3.29: Experimental results. (a) CAR as a function of P_p. The grey dashed line is a fitted curve. (b) The CAR measurement results between 156.25 MHz and 10 GHz. The dashed lines are fitted curves.

Figure 3.29 presents the experimental measurements of CAR at different R. Figure 3.29(a) plots the CAR as a function of P_p at each R. The measurement results of each R are consistent with one another with the exception of 5 GHz and 10 GHz, results measured at these two repetition rates show reduced CAR because the timing-jitter of the detectors are longer than the time between adjacent pulses, as discussed below. The dashed line is a fitted curve according to the relation between CAR and P_p. Figure 3.29(b) plots the CAR as a function of C_{true} at each R. The maximum and minimum CARs in Figure 3.29(b) are around 400 and 30, respectively. The dashed lines are the fitted curves that show the variation of CAR with C_{true} and these curves are calculated based on [5]:

$$CAR = \frac{C_{true}}{(C_{true}/\eta_i + d_s)(C_{true}/\eta_s + d_i)}. \tag{3.17}$$

Here, d_s and d_i represent the uncorrelated counts from the noise sources in the measurement. Figure 3.30 plot the C_{true} as a function of R for a fixed CAR. The C_{true} linearly increases with R before 5 GHz and then it is saturated and decreased

at 5 GHz and 10 GHz, respectively. The deviation in Figure 3.29(a) and the saturation in Figure 3.30 indicate that the benefit of increasing R is diminished at 5 GHz and the optimal R of current setup is around 2.5 GHz.

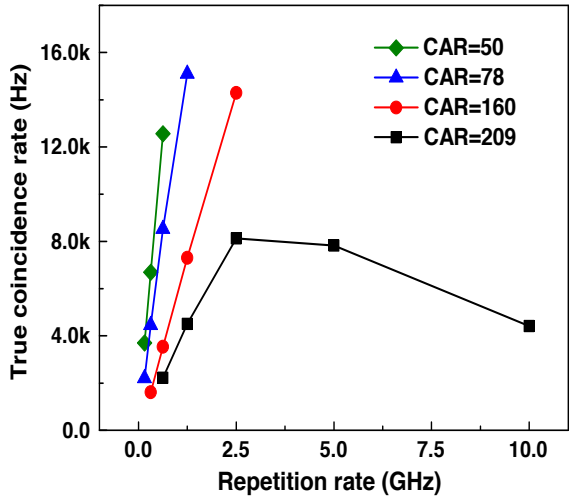

FIGURE 3.30: C_{true} against R at fixed CAR.

In Figure 3.28(a), C_{true} quadratically increases with P_p without deviation. The quadratic variation indicates that intrinsic nonlinear losses, such as TPA and FCA, has negligible impact at these combinations of pump and generation rate. Rather, the discrepancy between Equation (3.16) and the measurement results in Figure 3.30 indicates additional noise sources are included in the measurement, as CAR$= C_{true}/A$, where A represents the uncorrelated accidental coincidences. Potential noise sources in the experimental setup include the dark counts of the detectors (<100 Hz), pump leakage through imperfect spectral filtering and SpRS. Raman noise from silicon is negligible, because the 800 GHz frequency detuning between pump and idler (signal) photon is far from the narrow Raman peak of silicon [222]. Raman noise from the silica fibres surrounding the silicon nanowire is a potential noise source. The data indicates that the discrepancy is mainly due to the timing-jitter of the detection system. Figure 3.31 shows the zoomed histogram of three coincidence measurements with the same C_{true}, around 5,600 Hz, at different R, 2.5 GHz, 5 GHz and 10 GHz. The main coincidence peak extends between 12 ns and 12.3 ns, and the coincidence counts contributed by the noise sources are seen in the histogram as accidental peaks. The duration of the coincidence window (green rectangle) used in the coincidence measurement is set to 300 ps, according to the temporal width of the main coincidence peak. Hence, when the pump repetition rate is smaller than 5 GHz, only one accidental peak is included within the window, such as 2.5 GHz shown in Figure 3.31. However, when R increases to 5 GHz, the accidental peaks start to overlap with one another, because 200 ps time interval is insufficient to clearly separate two accidental peaks with 300 ps width. The accidental peaks merge together completely when R is further increased to 10 GHz. Hence, when the repetition rate is higher than 5 GHz, the detection system used in this work cannot tell the correct time information of each heralded single photon. And more than one accidental peaks

are included in the coincidence window, whereas Equations (3.12) to (3.16) assumed there is only one accidental peak taken into account. Therefore, the CAR is degraded at 5 GHz and 10 GHz. The temporal widths of the coincidence peaks are mainly determined by the timing-jitter of the SSPDs [223, 224], which is significantly larger than the timing-resolution of the TIA. Each SSPD has a timing-jitter of around 120 ps, so that the coincidence peak is around 170 ps FWHM, accounting for both detector jitters. The coincidence window is set to 300 ps so as to include about 95% of the counts in the coincidence peak. SSPDs with timing-jitter 15 ps have been demonstrated [225], will be able to correctly tell the time-bin information of heralded single photons when the pump rate is increased into 10 GHz or even 20 GHz. Beside the timing-jitter, the reset time of SSPD is another potential reason as the single photons might arrive the detector when it is not recovered from previous detections.

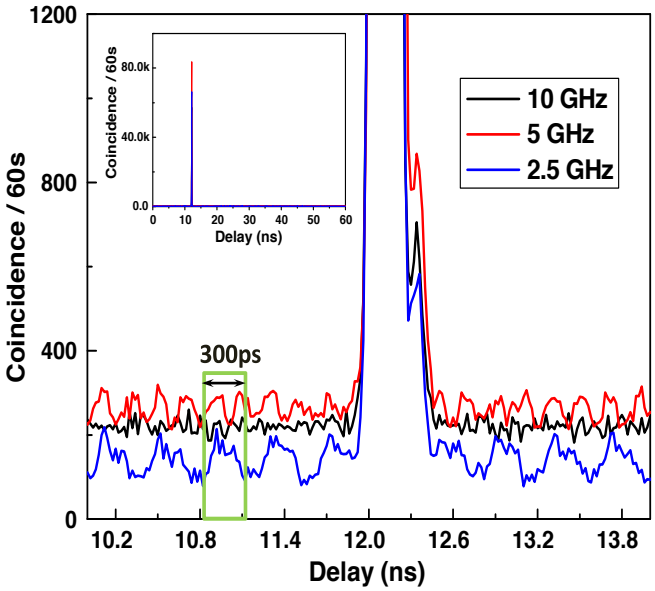

FIGURE 3.31: The zoomed histogram of coincidence measurement. The inset is the original histogram. The green rectangle shows the coincidence window in the measurement.

The coincidence rate here compares well to previous experiments at lower repetition rates in silicon nanowire [11], and to those at relatively high rates in silica fibers [226]. Ultimately, the goal is to build a high-efficiency photon source in an integrated platform, by combing photon pair sources with TMUX. In TMUX schemes, μ is enhanced by shifting heralded single photons from different temporal modes to one fixed temporal mode via a reconfigurable delay line [106, 110, 196–199], once the detection system correctly tells the temporal information of the heralded single photon. Meanwhile, the loss of the delay line can be significantly reduced if higher repetition rate pump pulses are used. In this case, the length of the required delay line will be reduced accordingly. However, the experimental results clearly point out that the most beneficial pump repetition rate is determined by the timing-resolution of the single-photon detection systems rather than intrinsic nonlinear losses, because resolving the correct temporal information for each heralded single photon is a fundamental requirement of TMUX.

3.5.4 Conclusions

In this section, the advantage of increasing R has been systematically demonstrated via the measurements of coincidence rate against CAR. The experimental results show that the single-photon rate is linearly enhanced with increasing R until the time interval becomes comparable to the resolution of the single-photon detecting system, at which point the CAR is adversely affected. The resolution of the photon detecting system is mainly determined by its timing-jitter and reset time. The detection system is the main obstacle to increasing repetition rate of a heralded single-photon source instead of any intrinsic issues with silicon waveguide. These results are a step toward demonstrating a high-efficiency single-photon source for large-scale photonic quantum computing.

Contribution

I set up the experiment, took the data, and analysed the data under Dr. Chunle Xiong, Dr. Bryn A. Bell and Prof. Benjamin J. Eggleton's supervision. Dr. Mark Pelusi setup the pump rate control system. Dr. Jiakun He, Dr. Wei Geng Dr. Yunchuan Kong and Dr. Philipp Zhang offered technical support. Dr. Duk-Yong Choi and Dr. Chang Joon Chae provided the silicon nanowire.

Chapter 4

Entanglement generation and processing in silicon nitride circuits

Chapter 4 discusses a compact and reconfigurable silicon nitride chip that can generate, manipulate and analyse time-bin entangled photons. Linear analysis circuits, nonlinear photon sources and integrated time-bin entanglement chip are sequentially explained in this chapter.

Section 4.2 is written based on the following publication:
Chunle Xiong, Xiang Zhang, Andri Mahendra, Jiakun He, Duk-Yong Choi, Chang Joon Chae, David Marpaung, Arne Leinse, René G. Heideman, Marcel Hoekman, Chris Roeloffzen, Ruud Oldenbeuving, Paul W. L. van Dijk, Caterina Taddei, Philip H. W. Leong, and Benjamin J. Eggleton, "Compact and reconfigurable silicon nitride time-bin entanglement circuit," *Optica* **8**, 724-727 (2015).

Section 4.3 is written based on the following publication:
Xiang Zhang, Yanbing Zhang, Chunle Xiong, and Benjamin J. Eggleton, "Correlated photon pair generation in low-loss double-stripe silicon nitride waveguides," *Journal of Optics* **18**, 074016 (2016).

Section 4.4 is written based on the following publication:
Xiang Zhang, Bryn A. Bell, Andri Mahendra, Chunle Xiong, Philip H. W. Leong, and Benjamin J. Eggleton, "Integrated silicon nitride time-bin entanglement circuits," *Optics Letters*, **15**, 3469-3472 (2018).

4.1 Time-bin entanglement

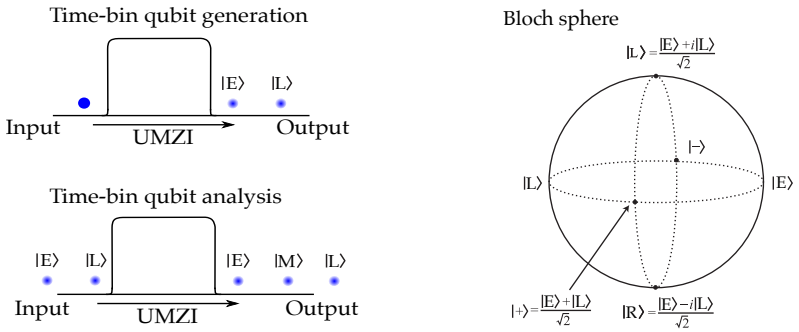

(a) (b)

FIGURE 4.1: Illustration of time-bin qubits. (a) Time-bin qubit generation and analysis; UMZI: unbalanced Mach Zehnder interferometer; the black arrow represents the propagation direction; the solid and blurred circles represent photons before and after time-bin encoding, respectively; $|E\rangle$, $|M\rangle$ and $|L\rangle$ represent the early, middle and late time-bin, respectively. (b) The Bloch sphere of a time-bin qubit; $|+\rangle$,$|-\rangle$, $|R\rangle$ and $|L\rangle$ represent four superposition states [15].

As explained in Section 2.3.3, the ultimate (or long-term) target of photonic quantum communication is a global-scale quantum network that can distribute entangled photons between remote users via free-space and optical fibre link. In practical circumstances, the optimal entanglement scheme is varied from one channel to another due to their distinct properties. Polarisation entanglement is a promising solution for free-space link since this channel has negligible polarisation mode dispersion and ultra-low propagation loss [135, 136, 138, 146, 150]. However, in a fibre-based link, the unpredictable stress and temperature fluctuation will adversely affect polarisation entanglement states. To perfectly address these practical issues, a robust entanglement scheme is the first prerequisite. Time-bin entangled photons are one of the most promising solutions, where qubits are encoded onto a photon which can exist in either an early or a late arrival time [227]. Since the quantum state is encoded in a time domain, the time-bin qubit is highly robust compared to using the polarisation or paths qubits [125, 180, 228], in terms of stress and temperature fluctuation in fibre. Figure 4.1(a) presents a time-bin qubit generation and analysis, both relies on an unbalanced Mach-Zehnder interferometer (UMZI). Due to an imbalanced path and reconfigurable couplers in an UMZI, the time-bin encoded photon (blurring circle) exists in early (E) and late (L) time-bin simultaneously with the same probability. The qubit analysis also requires an UMZI with identical delay [15], so that the photon interference occurs in the middle (M) time-bin. The Bloch sphere of a time-bin qubit with four distinct superposition states, such as $|+\rangle$, $|-\rangle$, $|R\rangle$ and $|L\rangle$, is shown in Figure 4.1(b).

Beside the robust entanglement scheme, another key element to address practical challenges is integrated photonic circuits with reconfigurable elements, such

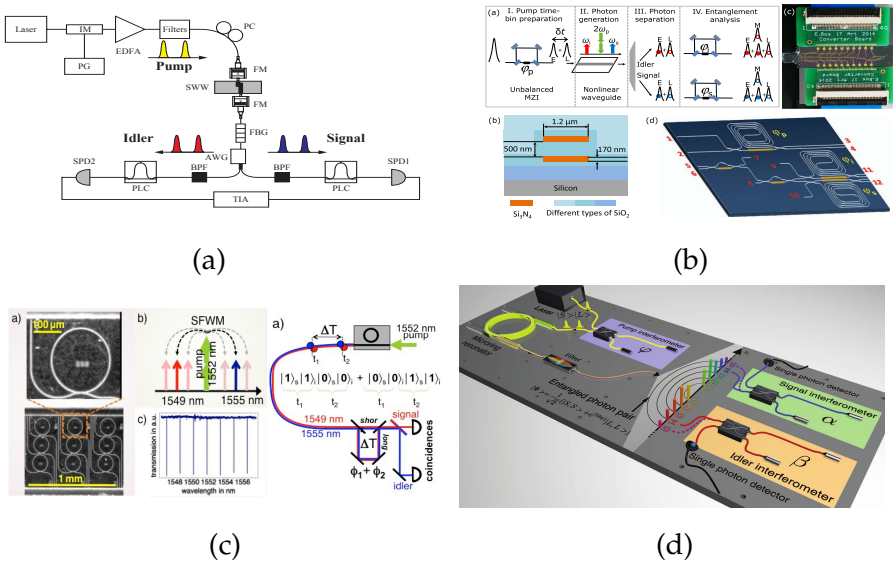

FIGURE 4.2: Time-bin entanglement demonstrations on different platforms. (a) Silicon wire waveguide (SWW): photon source; integrated silica circuits: analysis components [229]. (b) Silicon nanowire: photon source; integrated silicon nitride circuits: analysis components [13]. (c) Silicon nitride ring resonator: photon source; fibre interferometers: analysis components [181]. (d) Hydex ring resonator: photon source; fibre interferometers: analysis components [12].

as thermal phase shifters and tunable wavelength filters, as it offers intrinsic stability to generate and analyse entangled photon as well as practical benefits of repeatable fabrication. The generation and manipulation of time-bin entangled qubits generally require an UMZI with a time-delay in one path, as shown in Figure 4.1(a), where instabilities in fibre again become problematic [230]. This problem can be perfectly addressed using integrated photonics circuits that offer precisely chosen time delays, without the fine-tuning usually required in fibre. Meanwhile, the integrated solution imposes stringent requirements on the integration platform. For instance, although the silicon-on-insulator platform has excellent nonlinearity, its propagation loss (3 dB/cm) prohibits the construction of long delay lines [13, 99]. There have been numerous experiments demonstrating the generation of time-bin entangled photons using integrated nonlinear elements and analysing entanglement states by the UMZI either implemented in fibre or on a separate linear chip [12, 13, 181, 229], as shown in Figure 4.2. For a time-bin entanglement to be useful in the real world, the on-chip integration of the entire entanglement system is essential. The high performance of the entanglement system not only relies on photon generation, but also hinges on the compactness, scalability, and reconfigurability of the photonic circuits, which can prepare time-bins, suppress noise photons, demultiplex photons, and analyse entanglement states. Here, a single chip combining the nonlinear generation step with the linear processing and analysis of time-bin entangled states is explained in this chapter. In the following sections, linear analysis circuits, integrated nonlinear photon source and integrated time-bin entanglement chip are explained in

Section 4.2, 4.3 and 4.4, respectively.

4.2 Time-bin entanglement analysis circuits

This section explains integrated linear circuits designed and used for the entanglement state manipulation and analysis. This section includes four parts.

4.2.1 Motivation and principle

Since time-bin entangled photons are encoded in two temporal modes (early and late) simultaneously, it requires an unbalanced Mach-Zehnder interferometer (UMZI) to prepare, manipulate and analyse the entanglement states. If an UMZI is built by optical fibres, a feedback control system is required to maintain precise time delay. Otherwise, the generation and analysis processes will be adversely affected by external fluctuations, such as stress and temperature variations. Such a complicated and sensitive system is not an optimal solution for practical applications. Due to the intrinsic stability and repeatability, integrated UMZI would be an optimal solution. Here, low-loss double-stripe silicon nitride circuits are utilised to built three UMZIs and one wavelength division multiplexer (WDM) in a single photonic chip to manipulate and analyse entanglement state, the principle and experimental results are explained in the following sections.

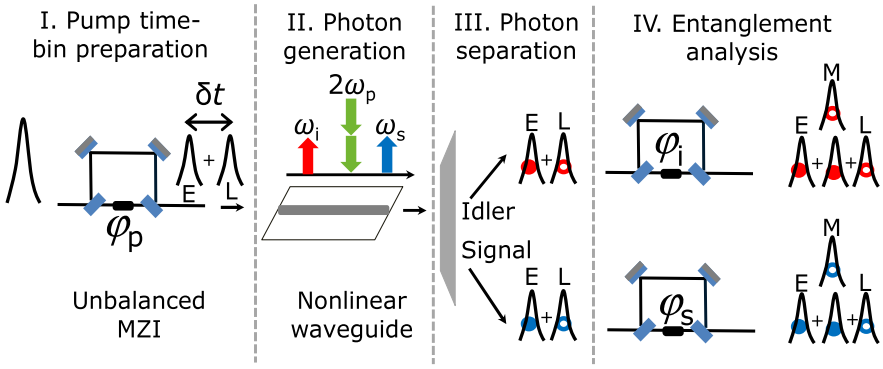

FIGURE 4.3: Principle of time-bin entanglement generation and analysis. E: early time-bin; M: middle time-bin; L: late time-bin; $\varphi_{p,s,i}$:relative phase difference in pump (p), signal (s) and idler (i). $\omega_{p,s,i}$:frequency of pump (p), signal (s) and idler (i).

Figure 4.3 presents the principle of time-bin entanglement generation and analysis which involving four steps: (I): using an UMZI to generate pump early (E) and late (L) time-bins with a relative delay of δt and phase difference of φ_p, (II) using a nonlinear waveguide to generate correlated photon pairs, called signal and idler, via a nonlinear process such as SFWM, (III): using a WDM to remove pump and separate photon pairs, and (IV): using another two UMZIs identical to the first one for entanglement analysis. In step (II) the pump power is controlled so that photon pair can only be generated either in the early or

late time-bin, both with a probability of 50%. This forms a superposition state $1/\sqrt{2}(|E\rangle_s |E\rangle_i + e^{j2\varphi_p} |L\rangle_s |L\rangle_i)$, namely, time-bin entanglement. In step (IV), when the early photon pass through the longer path and the late photon pass through the shorter one, nonclassical photon interference will occur in the middle (M) time-bin, because the early and late photons are indistinguishable.

To generate high-quality time-bin entangled photons and achieve high visibility interference, three requirements must be met. First, the relative delay between the two time-bins must be longer than the minimum of the pump pulse width, photon coherence time, and resolution of the detection system. This arrangement can avoid single-photon interference and ensures that the detection system can distinguish different time-bins. On the other hand, a long delay will reduce the bit rate for quantum information processing and can also introduce additional propagation loss. The second requirement is that the relative phase difference $\varphi_{p,s,i}$ between the longer and shorter paths must be stable, and the path length difference of the three UMZIs must be almost equal (errors within the coherent time of laser pulses); otherwise, interference will not occur. The third requirement is that the probability of photons appearing in each time-bin must be equal to 50% to maximise the interference fringe's visibility. Integrated photonic circuits can meet all of these requirements.

4.2.2 Chip layout and experimental setup

In this work, step (I), (III) and (IV) are integrated on a single photonic chip (28 mm × 8 mm) to achieve the phase stability, path length accuracy, and exact 50% probability of generating photons in each time-bin. The circuit is made using the low-loss double-stripe Si_3N_4 waveguide and its dimension, effective index and propagation loss have been explained in Section 2.4.3. In this photonic chip, spot-size converters are used at both ends of the waveguides to reduce the waveguide to SMF28 fibre coupling loss to around 1 dB per facet. The photograph and the schematic layout of the chip are shown in Figure 4.4(a) and Figure 4.4(b), respectively.

In Figure 4.4(b), the longer arm of the UMZIs is approximately 14 cm long and made in a spiral fashion, benefiting from the small bending radius offered by Si_3N_4. This gives a 795 ps delay relative to the shorter arm. The demultiplexers consisted of two slightly unbalanced Mach-Zehnder interferometers (MZIs) (length difference are 73.1 and 146.2 µm): the first rejects the pump by varying phase φ_{f1}, and the second separated signal and idler photon by adjusting phase φ_{f2}.

All MZIs and UMZIs incorporate tunable couplers for input and output. Each tunable coupler is a balanced MZI having two directional couplers with a fixed ratio close to 50:50 and a phase shifter in one arm to achieve an arbitrarily tunable splitting ratio. Tunablility is critical for generating and analysing photons in two time-bins with equal probabilities, and for achieving lossless demultiplexing. All phases are controlled through resistive heaters that are wire bonded (yellow line in Figure 4.4(a)) to standard electronic printed circuits boards (PCBs). Independent 16-bit digital-to-analog converters provided high-resolution control of 15 heaters on the chip. When a voltage (U) is applied, the temperature of the

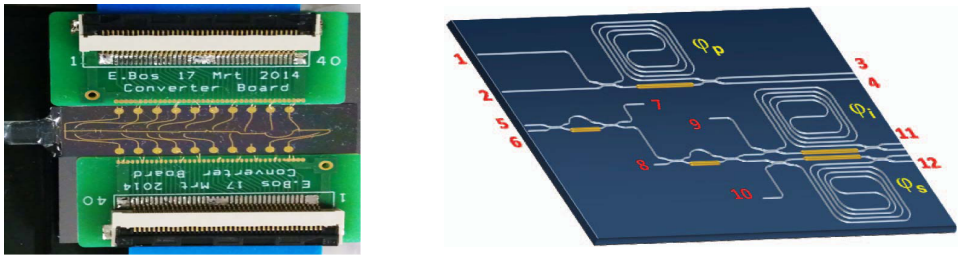

(a) (b)

FIGURE 4.4: Photograph and schematic of time-bin circuits. (a) A photograph of the Si_3N_4-based time-bin entanglement chip. The yellow parts are wire bonds for heaters, and the green parts are PCBs for providing voltage to the heaters. On the left-hand side is the pigtailed fibre array. (b) The schematic structure of the photonic circuit on the chip. The white lines represent the Si_3N_4 waveguides, and the yellow lines are resistive heaters. Only heaters for pump, signal and idler phase shift, and wavelength division multiplexer (WDM) are shown. Each tunable coupler consists of a balanced MZI with a heater in one arm (not shown). In total there 15 heaters on the chip. The numbers label the ports.

waveguide under the heater will exponentially increase to a maximum value determined by the power dissipated in the heater. Accordingly, the refractive index of the waveguide will increase, and this will introduce a phase shift. This thermo-optic phase shift changes quadratically with U. All waveguides, except the longer arm of the UMZIs, are a few millimeters long so that heaters could be constructed on top to achieve any phase shift up to 2π while maintaining low loss and keeping within the dissipation limits of the heaters. All optical input and output ports of the chip are arranged to align with a waveguide array with a spacing of 127 µm and pigtailed to a polarisation-maintaining fibre array (not shown in Figure 4.4). A straight reference waveguide is included for alignment and coupling loss measurement during pigtailing process. The total insertion loss of the 6.5 cm long reference waveguide is measured to be 4.3 dB.

Prior to the quantum entanglement experiment, the integrated circuits are characterised in the classical regime to ensure that the couplers and demultiplexers are set correctly. For the UMZI that is used to generate two pump time-bins (Figure 4.4(b)), labelled by φ_p, a pulse train with a pulse width of 10 ps centred at 1,555.7 nm is injected into input port 2 and monitored it from the two output ports 3 and 4 using a fast oscilloscope (OSC). Because of the delay in the longer arm, double pulses separated by 795 ps are observed at each output. The early pulses from both outputs are from the shorter arm, and the late ones are from the longer arm. By adjusting the voltage applied to the heater for the output coupler, the amplitudes of the early pulses become equal, as do the late pulses when the output splitting ratio is exactly 50:50. This is independent of the input splitting ratio. As the pulses from the longer arm experience higher loss, the input splitting ratio deviates from 50:50. By adjusting the voltage applied to the heater for the input coupler, the early pulses become equal to the late pulses in amplitude

when the effective input splitting ratio is 50:50 after taking into account the longer arm loss.

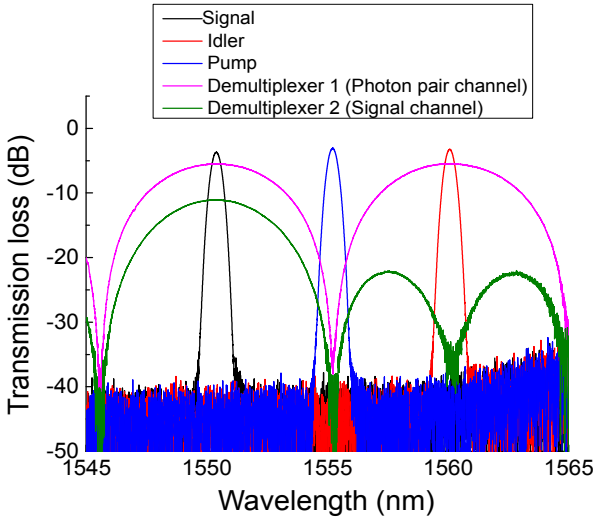

FIGURE 4.5: Characterisation of the wavelength demultiplexers. The black, blue and red traces are the transmissions spectra of three 0.5 nm band pass filter (BPF), indicating the signal, pump, and idler wavelengths used in the experiments. The pink trace shows the rejection of pump at the photon pair channel from demultiplexer 1 and the green trace show the signal channel from demultiplexer 2.

For demultiplexer 1 (labelled by φ_{f1}), which is used to reject the pump, the two outputs cannot be measured because one output is connected to demultiplexer 2 (labelled by φ_{f2}) on the chip. To characterise it, a broadband amplified spontaneous emission (ASE) source is injected into port 7 and monitored the spectra at ports 5 and 6 using an optical spectrum analyser (OSA). By adjusting the voltages applied to the three heaters for the MZI, the spectra measured from ports 5 and 6 are complementary to each other, and the loss between ports 7 and 5 is 5 dB at the transmission bands (pink trace, Figure 4.5) when the heaters are optimised. The loss is mainly due to waveguide-coupling and fan-out waveguide propagation losses, indicating nearly zero loss of the demultiplexer. The isolation to the pump is at least 25 dB. Due to symmetry of a MZI, when the pump, signal, and idler are injected to port 6 in the quantum experiment, the input from demultiplexer 1 to 2 keep the signal and idler photons and rejects the pump.

Because both outputs of demultiplexer 2 are connected to UMZIs on-chip, these outputs (labelled φ_i and φ_s) are characterised by the approach for setting up the pump UMZI before optimising demultiplexer 2. For characterising demultiplexer 2, ASE source is injected to port 6 and monitored the spectra from ports 11 and 12. When all heaters for demultiplexer 2 are set correctly, the spectra from ports 11 and 12 showed a dip at the pump wavelength and are complementary at the signal and idler wavelengths. The green trace in Figure 4.5 shows the spectrum taken from port 12, indicating very good separation of signal and idler channels. This loss spectrum shows that the total loss at the transmission windows of the whole circuit is approximately 11 dB, which comprised fibre–waveguide coupling loss, propagation loss in the longer arm, and a 3 dB

loss in the UMZI output coupler. It should be noted from Figure 4.5 that the MZI-based demultiplexers cannot do narrow-band filtering, but can separate pump, signal, and idler very well. This is sufficient for performing quantum operations on signal and idler photons on-chip with off-chip narrow-band filters placed before single-photon detectors (SPDs). Once the SPDs are on-chip, narrow-band filtering on-chip is required, and this is possible with the TriPlex technology [69].

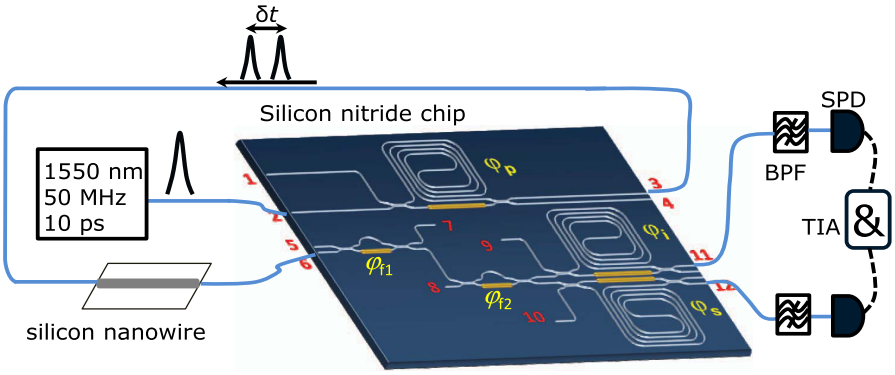

FIGURE 4.6: Experimental setup. Blue solid lines are optical fibres, and black dashed lines are electric cables. BPF: band pass filter; TIA: time interval analyser; SPD: single-photon detector.

After all the heaters are set in place, the time-bin entanglement experiments are performed. The setup is illustrated in Figure 4.6. The pump is a mode-locked fibre laser emitting 10 ps pulses centred at 1,555.7 nm with a repetition rate of 50 MHz. The pulses are injected into the first UMZI from port 2 for pump time-bin preparation. The output from port 3 of the UMZI is coupled to a 3 mm long, 220 nm high, and 460 nm wide silicon nanowire on another chip for photon pair generation. The linear and nonlinear properties of the silicon nanowire have been explained in Section 2.4.2. The output of the nanowire is sent back to port 6 of the on-chip demultiplexers, which rejects the pump and separate the signal (1,550.9 nm) and idler (1,560.6 nm) photons. Both outputs of demultiplexer 2 are connected to the UMZIs on-chip for entanglement analysis.

The signal and idler photons are coupled to off-chip band pass filters (BPFs) through ports 12 and 11 to further remove the pump and be post-selected in the 0.5 nm bandwidth shown in Figure 4.5, before being detected by two InGaAs avalanche SPDs (ID210 from ID Quantique). The SPDs are gated by the 50 MHz laser clock, and the gates are aligned with the middle time-bin. The effective gate width is 1 ns. The SPD configuration is used to avoid the detection of photons from other time bins. To minimise the dark counts and after-pulsing probability, the detection efficiency is set at 10% and the dead time is set at 20 µs. The coincidences are analysed by a time interval analyser (TIA).

4.2.3 Experimental results and discussions

The coincidences are a function of $\cos(\varphi_s + \varphi_i + 2\varphi_p)$ [231, 232]. At the coupled peak power of 0.45 W (into the silicon nanowire), when φ_p and φ_i are fixed (no voltage applied) and φ_s is varied by adjusting the voltage (U) applied to the

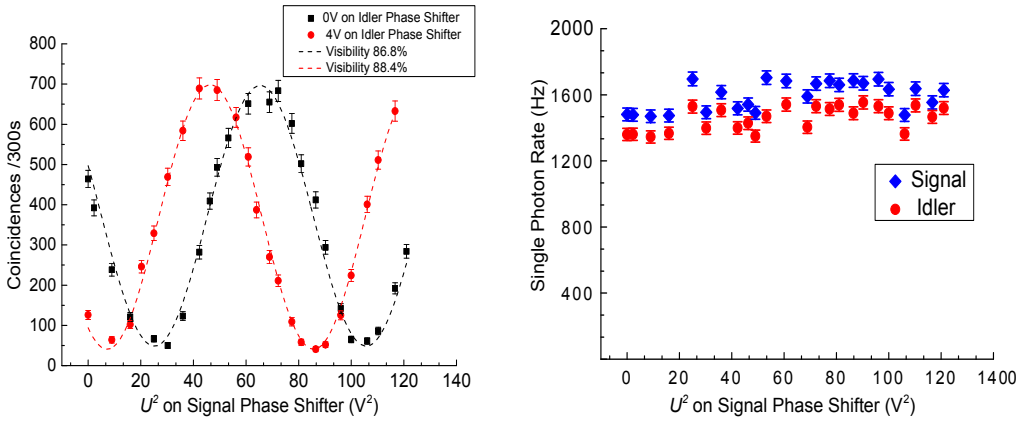

(a) (b)

FIGURE 4.7: Coincidence results. (a) Coincidences as a function of the square of the applied voltage to the heater of the UMZI in the signal photon channel. Black squares and red dots represents two nonorthogonal measurements when the voltage applied to the heater of the UMZI in the idler channel is set at 0 and 4 V, respectively. The dashed lines are cosine fits. Poisson error bars are used, see Equation (2.36). (b) Measured singles for the signal (blue diamonds) and idler (red dots) channels at different applied voltages to the signal channel heater. Poisson error bars are used, see Equation (2.36).

heater, an 86.8% visibility fringe is observed, without subtracting any noise (Figure 4.7(a), black squares). To confirm the entanglement, high-visibility fringes must be observed in two nonorthogonal measurement bases [231, 232]. thus φ_i is slightly changed by applying 4 V to its heater and again varied φ_s, which results in an 88.4% visibility fringe (red dots) being observed. Both fringes exhibit high visibilities beyond the classical limit of 70.7% [233], clearly indicating that high-quality time-bin entanglement is achieved. While recording the coincidence measurements, the single count at each detector is also monitored and they are insensitive to $\varphi_{s;i}$ (as shown in Figure 4.7(b)), further evidence that the interference fringe is due to two-photon entanglement.

The visibility of an ideal photon interference fringe should be 100%. This demonstration shows a maximum 88.4% visibility because of accidental coincidences from a few noise sources. One is the dark count of the detectors. The second is due to the small probability of producing multiple pairs. The third one is the thermal cross-talk between each phase shifter. Finally, the last one is due to the so-called charge persistence effect of the SPDs [234]. This effect means when SPDs work at the gated mode, the photons that arrive at the SPDs will interact with the detector even though the gate is OFF. The interaction will trap electrons and produce a detection pulse once the gate is back ON in a few nanoseconds. In measurements, an extra small coincidence peak is observed in addition to the main peak in the histogram, indicating the capture of photons from the early time-bin even though the detectors are expected to only detect the photons from the middle time-bin.

Although this demonstration does not integrate the nonlinear waveguide for photon pair generation on the same chip, recent progress has shown that it is possible to use Si_3N_4 nonlinear devices for photon pair generation [181, 188], and such nonlinear devices can be made using the TriPlex technology [183]. In addition, a compatible Si_3N_4 platform exhibits a fast stress-optic effect at >1 MHz [206], indicating the potential of the Si_3N_4 circuit used in this work for operating at a much higher speed in the future for quantum information transmission and processing. This demonstration clearly establishes that Si_3N_4 photonic circuits incorporating all four steps illustrated in Figure 4.3 for time-bin entanglement are feasible. Once this technology is available, taking advantage of the reconfigurability of the circuit, on-chip time-bin entangled photons can be tested as demonstrated in this work, and then switched to port 7 for long-distance entanglement distribution by simply controlling the phase φ_{f1}. On the other hand, taking advantage of the compactness of the circuit, multiple time-bin entanglement sources and Bell measurement devices can be made on a single chip for on-chip time-bin qubit teleportation.

4.2.4 Conclusion

The high-performance time-bin entanglement analysis circuits based on low-loss double-stripe Si_3N_4 waveguide have been demonstrated in this section. This is a significant step toward the ultimate goal of completely integrating all components to realise an integrated time-bin entanglement chip for large-scale quantum network.

Contribution

Dr. Chunle Xiong proposed this project. I set up the experiment, took the data, and analysed the data under Dr. Chunle Xiong and Prof. Benjamin J. Eggleton's supervision. Dr. Andri Mahendra, and Prof. Philip H. W. Leong designed the FPGA circuits and interface with other components. Dr. Duk-Yong Choi and Dr. Chang Joon Chae provided the silicon nanowire. Dr. David Marpaung, Dr. Arne Leise, Dr. Rene G. Heideman, Dr. Marcel Hoekman, Dr. Chris G. H. Roeloffzen, Dr. Ruud M. Oldenbeuving, Dr. Paulus W. L. van. Dijk, Dr. Caterina Taddei fabricated the circuits. Dr. Jiakun He offered technical support.

4.3 Integrated nonlinear light source

In this section, the nonlinearity of low-loss double-stripe silicon nitride circuits are characterised by coincidence measurements. Four parts are included in this section.

4.3.1 Motivation

In Section 4.2, the low-loss double-stripe silicon nitride circuits are used to build three unbalanced Mach-Zehnder interferometers (UMZIs) and one wavelength division multiplexer (WDM) on a single chip. More than 86% fringe visibility

without subtracting noise indicates highly entangled photon are generated, manipulated and analysed in that work. However, the correlated photon pairs are generated in a silicon nanowire instead of a double-stripe Si_3N_4 circuit, since the silicon nanowire has much higher nonlinearity than the Si_3N_4 circuit. For practical applications, a highly integrated time-bin entanglement chip that includes entangled photon generation, manipulation and analysis is an optimal solution to develop a robust and scalable quantum network. If this double-stripe Si_3N_4 waveguide structure has sufficient nonlinearity for photon pair generation, both nonlinear photon sources and linear processing circuits can be integrated on a single chip without a fibre coupling between separate chips. The classical four-wave mixing (FWM) demonstrated on a double-stripe Si_3N_4 ring resonator indicates that such a waveguide structure can be used for photon pair generation [188]. Around 2 THz FWHM of SFWM has been estimated in the double-stripe Si_3N_4 waveguide, as explained in Section 2.4.3. An experimental demonstration of photon pair generation in a double-stripe Si_3N_4 waveguide is explained in the following sections

4.3.2 Experimental setup

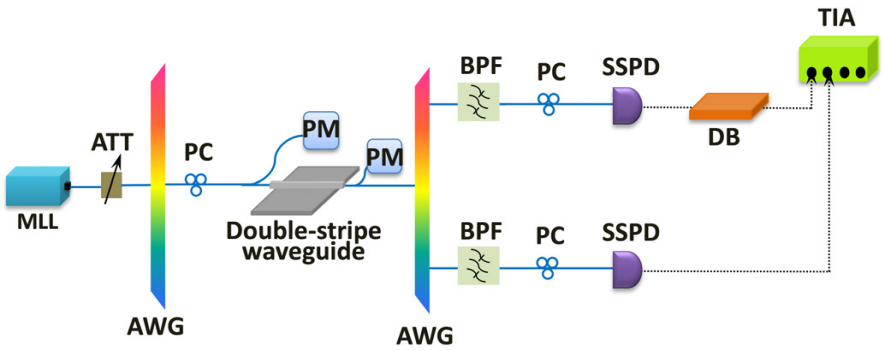

FIGURE 4.8: Experimental setup. MLL: mode-locked laser; ATT: attenuator; PC: polarisation controller; AWG: arrayed waveguide grating; PM:power meter; BPF: band pass filter; DB: delay box; SSPD: super-conducting single-photon detector and TIA: time interval analyser.

Figure 4.8 shows the experimental setup. Optical pump pulses at 10 ps width are generated from a 50 MHz mode-locked laser (MLL) at the central wavelength of 1,555.74 nm. The input power is controlled by a tunable attenuator (ATT). Amplified spontaneous emission (ASE) noise companioned with pump pulses is eliminated by an array waveguide grating (AWG) which has a channel bandwidth of 50 GHz. Since the double-stripe Si_3N_4 waveguide has the lowest propagation loss at TE mode, a polarisation controller (PC) adjusts the pump to be TE polarised before entering the Si_3N_4 waveguide. The waveguide is fibre-pigtailed with polarisation-maintaining fibres at both ends. The polarisation of pump pulses is precisely adjusted to TE mode when the output power is maximised. The total insertion losses are 4.3 dB including the waveguide-fibre coupling loss

(3 dB) and propagation loss (1.3 dB). The signal and idler photons are separated by an AWG with an insertion loss of 3 dB before being filtered by a tunable band pass filter (BPF). The BPF has an insertion loss of 2 dB and its bandwidth is 100 GHz. Before being detected by superconducting single-photon detectors (SSPDs), the polarisation of generated photons in each channel are adjusted by a PC with an insertion loss of 1 dB, as the SSPDs are polarisation dependent. The detection efficiency of SSPDs is set to 60% and the dark count rate is around 500 Hz at this efficiency. After maximising single counts in each channel, the time information of each photon is finally collected by a time interval analyser (TIA). Any polarisation mismatch, fluctuation and cross-talk can be detected instantaneously based on a noticeable fluctuation of single counts in each channel. The collection efficiency from the output of the waveguide to the detector in each channel is 10.5 dB. An electronic delay box in the idler channel is used to shift the coincidence peak to a positive delay in the histogram of coincidence measurement to avoid the loss of coincidence counts. The resolution of the TIA is 27 ps.

4.3.3 Experimental results and discussions

Figure 4.9(a) shows a typical histogram of coincidence measurements. The main peak located at 48 ns represents coincidences, which record the simultaneous detection of signal and idler photons that are generated from the same pump pulses. It indicates the generation of time-correlated photon pairs. The coincidence counts contained in the main peak is described by the raw coincidence rate (C_{raw}). Other smaller side peaks with a time interval of 20 ns records the simultaneous detection of photons from different pump pulses, and the count rate obtained from these side peaks represents the accidental rate (A). The true coincidence rate $C_{true} = C_{raw} - A$ suggests the brightness of a correlated photon pair source, and CAR indicates the strength of photon pair correlations. These two parameters are usually used to characterise the performance of a correlated photon pair source, as explained in Section 2.2.7. Figure 4.9(b) illustrates the dependency of C_{true} and CAR on average pump power. The true coincidence rate (diamonds) increases with power, because the efficiency of SFWM scales quadratically with the pump power. The measured true coincidence rate is 1.6 kHz at the pump power of 3.2 mW. Taking into account the collection efficiency, the 1.6 kHz true coincidence rate corresponds to a correlated photon pair generation rate of 185 kHz in the waveguide. CAR (squares) reduced from 16 to 10.6 with the increase of the power due to the generation of multi-pair via SFWM. When the power is less than 3.2 mW, a CAR over 10 is achieved. This suggests the correlated photon pair source can be used for QKD system with 5% error rate [94].

The CAR is analysed without other noise except multi-pairs and the overall value of CAR in Figure 4.9(b) is far below the expectation based on the assumption of including the multi-pair noise only and CAR$\approx 1/\mu$. Here, $\mu = C_{true}/(\eta_i \eta_s R)$ is average number of photon pairs per pulse, η_i and η_s are the collection efficiencies of idler and signal photons respectively, and R is the laser repetition rate. Using the measured true coincidence rate at the input power of 3.2 mW, the CAR should be over 270. However, in Figure 4.9(b), CAR is far

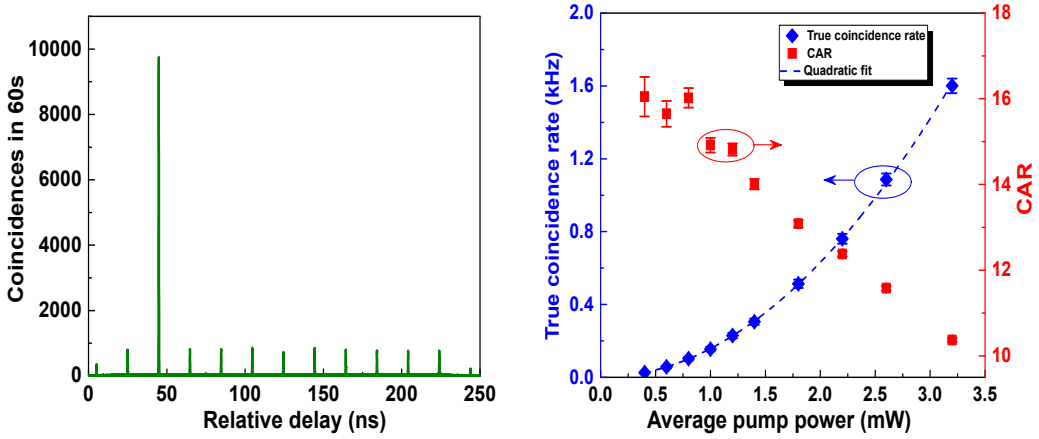

(a) (b)

FIGURE 4.9: Coincidence results. (a) A typical histogram of coincidence measurements at the input average pump power of 3.2 mW. (b) True coincidence rate (diamonds) and CAR (squares) as a function of average pump power; dashed line is quadratic fit. Error bars are calculated by Poissonian distribution, see Equation (2.36).

below this expectation. This significant discrepancy suggests that there are other noise sources contribute to this entire reduction, such as pump leakage and SpRS, which will be discussed in the following paragraphs.

The pump leakage is first investigated via coincidence measurements at different pump-idler/signal frequency detunings (Ω). The pump leakage results from the spectrum overlap between the pump channel and the selected signal/idler channel. If pump leakage contributes to the majority part of noise photons, the accidental peaks should be similar to the main peak, since the correlation between the detections in signal and idler channel is mainly determined by pump photons rather than correlated photon pairs. The spectrum overlap decreases significantly with the increase of Ω. Figure 4.10(a) shows the histogram of coincidence measurements with three different Ω at the same average pump power of 3.2 mW. To discriminate the difference between the main peak and the side peaks at each Ω, different delays at each Ω are intentionally introduced via the delay box. When $\Omega = 400$ GHz, the accidental peaks are similar to the main peak located at 40 ns. In the case of $\Omega = 500$ GHz (600 GHz), the accidental peaks are quite trivial compared with the main peak, located at 48 ns (52 ns). Note the decrease of the main peak at $\Omega = 600$ GHz compared to $\Omega = 500$ GHz comes from the phase mismatch of SFWM (see Figure 2.22(b)). Therefore, to minimise the pump leakage without sacrificing too much photon pair generation efficiency, $\Omega = 500$ GHz is chosen for the following inspections.

The noise induced by SpRS is investigated after excluding the first possible noise sources. There are two direct ways to confirm this. One is to directly measure the Raman spectrum to show if it overlaps with the frequency range used in the measurement. Previous measurement has shown that Si_3N_4 has a broadband Raman spectrum that indeed covers the frequency range used in this work [190]. The other is to compare the noise level at room temperature and a cooler condition since Raman is temperature dependent [191]. As the Si_3N_4 waveguide

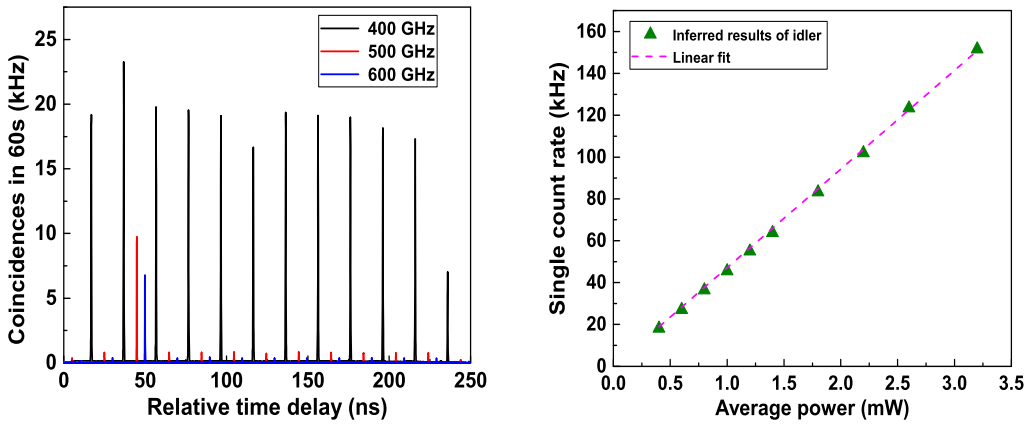

(a) (b)

FIGURE 4.10: Measurement results. (a) Histogram of coincidence measurements at three different Ω. (b) Inferred single count rate generated from SpRS. Triangles are the inferred single counts rate of idler. Dashed line is a linear fit.

is fabricated on the same chip with other delicate circuits that might be damaged by cooling. Therefore, a relatively indirect investigation is adopted as explained below.

The noise contribution of SpRS is analysed both in signal and idler channels. Single counts detected by SSPD include photons generated from SFWM and SpRS. The photon generation via SFWM scales quadratically with the pump power while SpRS scales linearly. The coincidence analysis in Figure 4.9(b) has already confirmed the quadratic dependence. Here, the idler counts is used to explain the SpRS-induced noise, since the signal channel has similar single counts. The inferred single counts ($C_{i_{SpRS}}$) from SpRS is calculated by $C_{i_{SpRS}} = C_{i_{total}} - C_{i_{SFWM}} - D$. Here, $C_{i_{total}}$ is the total counts detected in the idler channel, $C_{i_{SFWM}}$ is the single counts generated from SFWM and D represents the dark counts. $C_{i_{SFWM}}$ is analysed by $\mu\eta_i R$. Figure 4.10(b) illustrates the inferred results of idler (triangles) as a function of the input pump power. The linear fit (dashed line) indicates that the noise photons are most likely contributed by SpRS, as SpRS is linearly dependent on the pump power. Since only pump pulses propagate in the waveguide and the power is relatively low, it is unlikely to have SRS.

As shown in Figure 4.8, the Si_3N_4 waveguide (6.5 cm long) is connected with silica fibres (6 m long). The silica fibres might also play non-trivial part in the correlated photon pair generation. Additional measurements are implemented to further confirm that correlated photon pairs are generated in the Si_3N_4 waveguide rather than in the silica fibres. The double-stripe Si_3N_4 waveguide and the pigtailed polarisation-maintaining fibres are replaced by a tunable attenuator and two fibres with similar length to repeat the measurement. The total loss of the replacements has been adjusted to 4.3 dB to simulate the waveguide loss. At the same average pump power, the true coincidence rate in silica fibres is less than 4% of the true coincidence rate in the double-stripe silicon nitride waveguide. This confirms that correlated photon pairs are indeed generated in the silicon

nitride waveguide.

In the future, both the source brightness and CAR can be further improved. For example, a ring resonator can be designed as an ultra-compact nonlinear source component. The enhancement is briefly estimated as follows. Taking the calculated effective mode index ($n_{eff} = 1.72$) of the structure and the pump wavelength (1,555.74 nm) and using the equation about free spectral range (FSR) of rings:

$$FSR = \Delta\lambda = \lambda^2/(2\pi n_{eff} r), \tag{4.1}$$

The ring radius is calculated to be 55 and 111.9 µm for the FSR of 500 and 250 GHz, respectively. These FSR are chosen because the Ω between pump and signal/idler in the experiment is 500 GHz and it should be the integral multiple times of FSR. To maintain low losses, the minimum bending radius of the double-stripe silicon nitride waveguide is 70 µm [235]. So a radius of 111.9 µm is a more preferable option than 55 µm. The circumference of the ring resonator is $L = 2\pi r = 702.7$ µm. The loss per round trip is 0.014 dB. To be realistic, the Q factor in Ref.[188] is adopted: $Q = 7 \times 10^5$. Using the known Q factor, the effective mode index n_{eff}, and the circumference L of the ring, the finesse (F) by is calculated:

$$F = Q\lambda/(n_{eff}L) = 900. \tag{4.2}$$

As the round trip loss is negligible, the intensity enhancement is

$$B \approx F/\pi = 286.6. \tag{4.3}$$

Since SFWM process scales quadratically with the pump intensity while SpRS scales linearly, compared with the straight waveguide pumped at the same intensity, the ring resonator will not only generate photon pairs more efficiently, but will also increase the ratio between SFWM photons and SpRS noise and thus improve the CAR. Furthermore, the required bandwidth of an on-chip filter is not stringent due to the extremely narrow line width of the ring resonator which has already guaranteed the purity of correlated photon pairs. On the other hand, the noise photons from SpRS could be reduced significantly by cooling. More specifically, the Raman noise could be reduced by 70.6%, if the sample is cooled down to the temperature of liquid nitrogen, as explained in Section 2.4.3.

4.3.4 Conclusion

In this section, correlated photon pair generation has been experimentally demonstrated in a low-loss double-stripe Si_3N_4 waveguide via SFWM. The CAR achieves over 10 when the average pump power is less than 3.2 mW. The CAR is mainly limited by SpRS which could potentially be mitigated by cooling. This work implies that the low-loss double-stripe Si_3N_4 waveguide is a promising structure for integrating both nonlinear photon sources and linear processing circuits in a monolithic photonic chip for various applications. It takes us a step further towards integrated time-bin entanglement circuits for practical applications.

Contribution

I set up the experiment, took the data, and analysed the data under Dr. Chunle Xiong and Prof. Benjamin J. Eggleton's supervision. Dr. Yanbin Zhang provided theory insight of the measurements.

4.4 Integrated time-bin entanglement chip

An integrated time-bin entanglement chip that includes nonlinear photon sources and linear processing components, such as filter, wavelength division multiplexer and unbalanced Mach-Zehnder interferometer, is demonstrated in this section. The entanglement states are characterised by quantum state tomography (QST). The repeatability of this CMOS compatible platform is also verified via another identical circuits on the same chip. Four parts are included in this section.

4.4.1 Motivation

As explained in Section 4.1, an integrated time-bin entanglement photonic chip that can generate, manipulate and analyse entanglement states is an optimal solution to build a robust, scalable and cost-efficient quantum network. However, such integrated time-bin entanglement circuits have not yet been experimentally demonstrated. Section 4.2 demonstrates that the double-stripe Si_3N_4 waveguide is a promising structure to build linear circuits for entanglement manipulation and analysis. Section 4.3 demonstrates such a double-stripe Si_3N_4 waveguide is a viable structure for nonlinear photon pair generation. These two sections clearly indicate both nonlinear and linear components can be fabricated by one waveguide structure which guarantees repeatability and cost-effectiveness simultaneously. The experimental methods and results are sequentially explained in the following parts.

4.4.2 Experimental setup and chip layout

Figure 4.11 shows the experimental setup used in this work. A 50 MHz mode-locked laser (MLL) generates 10 ps pump pulses (green) centred at 1,552.5 nm. Amplified spontaneous emission (ASE) noise from an internal erbium doped fibre amplifier (EDFA) is filtered by a band pass filter (BPF) with 0.3 nm FWHM. Pump power and polarisation are adjusted by an attenuator (ATT) and a polarisation controller (PC) respectively, prior to input to the Si_3N_4 chip.

The chip utilises low-loss double-stripe Si_3N_4 waveguides that only support the TE mode with 0.2 dB/cm propagation loss [13, 99]. Less than 0.1 dB/cm propagation loss should be achievable with an optimised fabrication process [69]. Its cross-sectional structure and dimensions are shown as an inset in Figure 4.11. The schematic of the photonic chip is also illustrated in Figure 4.11. First, the unbalanced Mach-Zehnder interferometer (UMZI1), with 800 ps time delay between short and long paths, splits each pump pulse into two identical pulses which define two time-bins (early and late). The additional loss (3 dB) introduced by the long arm (14 cm) of UMZI1 is compensated by adjusting the coupling ratio of the

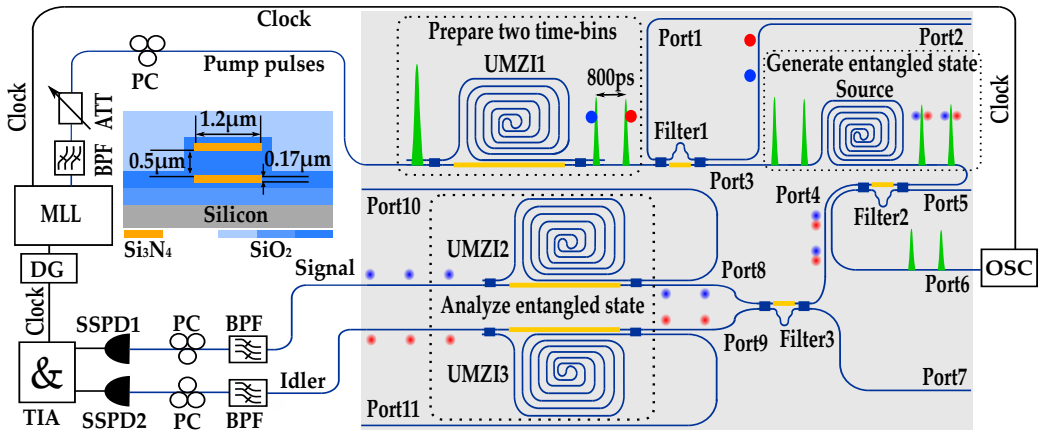

FIGURE 4.11: Experimental setup. MLL: mode-locked laser; BPF: band pass filter; ATT: attenuator; PC: polarisation controller; UMZI: unbalanced Mach-Zehnder interferometer; DG: delay generator; OSC: oscilloscope; SSPD: super-conducting single-photon detector; TIA: time interval analyser. Black and blue lines are electronic and optical circuits, respectively. Solid circles are noise photons; Blurred circles are entangled photons; Gold rectangles are thermal phase shifters.

input and output coupler so that there is equal power transmitted through each arm [13], and similar for UMZI2 and 3. A thermal phase-shifter (gold) in UMZI1 is used to tune the relative phase between early and late pump pulses, φ_p. In the long arm of UMZI1, the strong pump pulse will create noise photons (blue and red circles) by SFWM and SpRS. A Mach-Zehnder interferometer (MZI) with a small imbalanced length of 176 μm between paths is used to create a filter (Filter1) which transmits the pump pulses but rejects noise at the wavelengths which will be used for the entangled photons. After tuning the phase shifter, the spectrum of Filter1 is shown as the magenta line in Figure 4.12(a) and it indicates the spectrum of the signal and idler where the entangled photons will be created (centred at 1,548.5 nm and 1,556.5 nm). Comparing with the input spectrum of amplified spontaneous emission (ASE) noise (black), the transmission loss at pump wavelength is around 7 dB. Considering the coupling loss to fibre of 3 dB per facet, this suggests Filter1 has a 1 dB insertion loss. Then a 6.5 cm spiral waveguide is used to generate correlated signal and idler photon pairs via SFWM, a $\chi^{(3)}$ nonlinear process with quadratic dependence on the peak power of the pump pulses. A characterisation of photon pair generation in this source is given in Section 4.3. The photon pairs are created in a coherent superposition state between each time-bin, so their state can be expressed as:

$$(|E\rangle_s |E\rangle_i + e^{2i\varphi_p} |L\rangle_s |L\rangle_i)/\sqrt{2}, \tag{4.4}$$

where $|E\rangle_x$ and $|L\rangle_x$ represent a photon in the early or late time-bin, respectively, and $x = s, i$ indicates signal and idler wavelengths.

After photon-pair generation, Filter2 with 176 μm length difference is used to separate the pump pulses from the entangled photon pairs. Filter2's spectrum is shown as the grey line in Figure 4.12(a) and its insertion loss at signal and idler

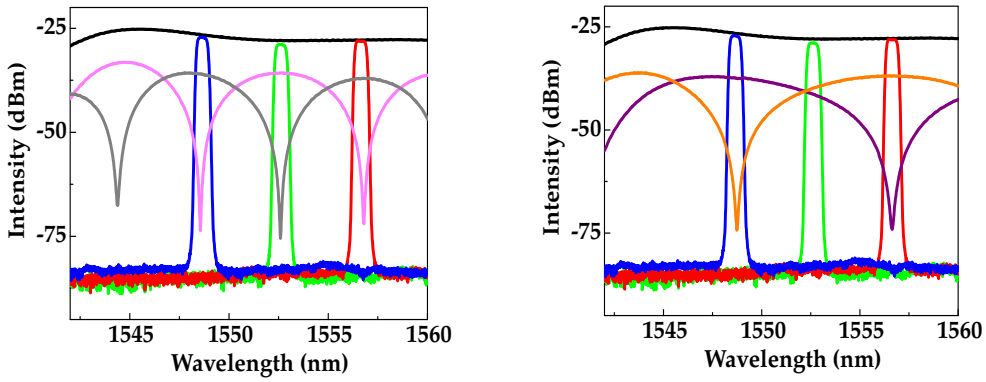

FIGURE 4.12: Spectra of Filter1-3. Blue, green and red lines represent the signal, pump and idler spectra respectively. (a) Spectra of Filter1 (magenta) which transmits the pump pulses but rejects noise at the signal and idler wavelengths; and Filter2 (gray), which rejects the pump pulses but transmits the generated signal and idler photons. (b) Spectrum of Filter3, which divides the signal and idler photons into separate ports; purple and orange lines represent the signal and idler outputs, respectively. All filters exhibit 30 dB extinction ratios.

are 1 and 2 dB respectively. Pump pulses are sent to an output port (Port6) and monitored by an oscilloscope (OSC). The pump power inside the spiral circuits is estimated by temporarily replacing OSC with a power meter. The measured power of 0.8 mW indicates the average pump power and the peak power inside the spiral are 2.1 mW and 4.2 W, respectively, due to the coupling loss (3 dB) and the propagation loss (1.3 dB). The experimental results in Section 4.3 show that at least 100 dB isolation is required to suppress pump noise. Filter3 with 86 µm length difference is used to divide the entangled signal and idler photons, with the spectra of the two output ports shown in Figure 4.12(b). The insertion loss of Filter3 is around 2 dB. In the measurement, signal and idler are then sent to two separate UMZIs (UMZI2 and 3) with time-delays which match UMZI1. These are used to measure and analyse the time-bin qubits. A photon originally in one of two time-bins can arrive at one of three times after passing through an UMZI. A photon previously in the $|E\rangle$ ($|L\rangle$) state can never be detected at the latest (earliest) of the three arrival times. Hence detecting a photon at the earliest or latest time makes a projective measurement onto the $|E\rangle$ or $|L\rangle$ state. However a photon detected in the middle arrival time could have originated from either time-bin, and so makes a projective measurement onto a superposition state:

$$(|E\rangle_x + e^{i\varphi_x}|L\rangle_x)/\sqrt{2}. \tag{4.5}$$

Here, φ_x is the relative phase between the arms of the UMZI. Each relative phase is controlled by a thermal phase-shifter in the corresponding UMZI. The ability to project time-bin qubits onto coherent superposition states makes it possible to verify that they are entangled and to carry out QST.

The photons are coupled off-chip and residual noise from the pump laser is removed by high isolation (≥60 dB) and low loss (2 dB) band pass filters (BPFs) with 0.3 nm FWHM. The polarisations are adjusted by PCs to maximise the detection efficiency of superconducting single-photon detectors (SSPDs) to around 50%. The dark counts and timing-jitter in SSPDs are around 200 Hz and <50 ps, respectively. A time interval analyser (TIA) (ID800) with 81 ps time-resolution is connected to three inputs: signal and idler SSPDs, and the laser clock, which is used for synchronisation. The repetition rate of the clock signal is down-converted by a delay generator to 1 MHz since the original 50 MHz clock would saturate the TIA. The photonic chip before and after bonding are shown in Figure 4.13(a) and Figure 4.13(b), respectively.

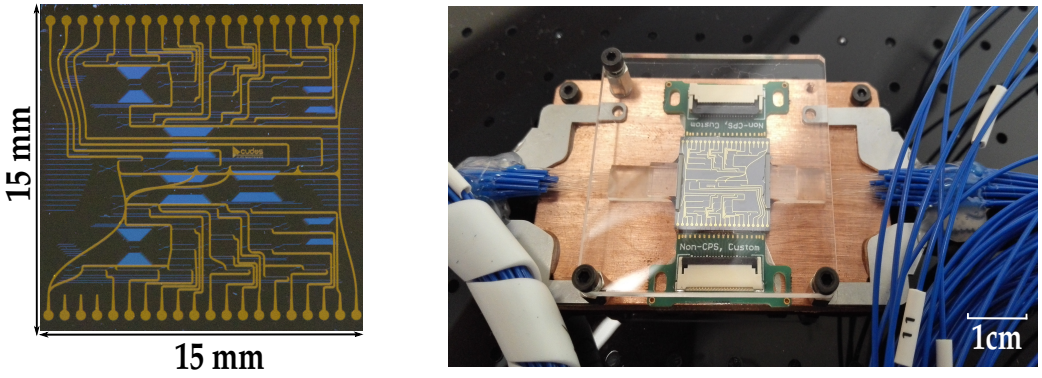

(a) (b)

FIGURE 4.13: (a) Photo of the bare photonic chip. Yellow lines are electronic connections and blue lines are the underlying silicon nitride waveguides. (b) The chip after packaging with printed circuits boards and arrays of polarisation maintaining fibres.

4.4.3 Experimental methods and results

The difference between signal and idler detection times is used to identify photons which originated from the same laser pulse and so constitute an entangled pair; the down-converted clock is sufficient to identify which of the three possible arrival times a given photon was detected in, relative to the original laser clock. An example histogram is given in Figure 4.14, showing the relative arrival times. Three peaks are visible for both signal and idler detections. The width of the peaks is due to the combined timing jitter of the SSPDs, the TIA, and the down-converted clock. It can be seen that this jitter is small enough compared to the 800 ps time separation to allow each of the three peaks to be clearly distinguished. It is expected that the signal and idler photons taken individually will appear to be in an incoherent mixture of the $|E\rangle_x$ or $|L\rangle_x$ states, and following classical statistics after the UMZI they are twice as likely to appear in the middle peak as in the earliest or latest peaks.

First, photon interference is used to calibrate the pump phase φ_p, which is varied whilst keeping φ_s and φ_i fixed. Figure 4.15 shows the interference fringe in the two photon counts, post-selected on both signal and idler arriving in their

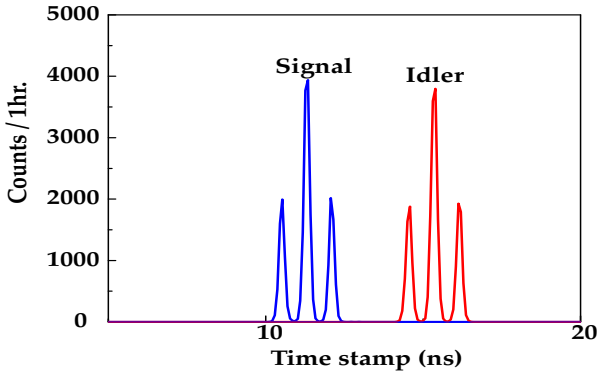

FIGURE 4.14: Histogram of signal and idler arrival times, relative to the laser clock.

central histogram peak. A visibility of 88% is obtained from a sinusoidal fit (the dashed line). At a maxima in this count rate, $2\varphi_p = \varphi_s + \varphi_i$. Hence the pump phase is fixed at the first maxima, where $U^2 = 64$, and QST is carried out by varying φ_s and φ_i, following the method of Ref.[15]. The selected phase of φ_s and φ_i are $\pi/2$ and $-\pi/2$ respectively, in addition to 0 for both phases.

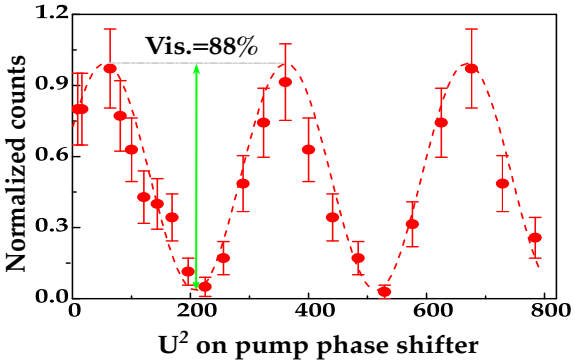

FIGURE 4.15: Photon interference with 88% visibility (Vis.); Red dots represent the results after post-selecting and count normalisation; the dashed line is a sinusoidal fit. Poisson error bars are used, see Equation (2.36)

QST generally requires a qubit be projected onto four different basis states, and for two-qubit QST all sixteen possible combinations of the basis states must be measured [14]. Here, the method of Ref.[15] is implemented for QST of time-bin qubits-only two phase-setting are used for each output UMZI, making four phase combinations in total. The other measurement bases are made up from the side-peaks in the histogram, which project the qubit onto the $|E\rangle$ or $|L\rangle$ state. The phase-settings are labelled B_1, B_2 and B_3, to indicate UMZI phases of 0, $\pi/2$ and $-\pi/2$ respectively.

The coincidence counts at each combination have been measured for one hour to suppress statistical uncertainty. After post-processing these data, each coincidence count is classified into one of the sixteen state projections required for QST and the results are shown in Table 4.2. For basis states which appear in more than one of the four phase settings, the counts are summed; this compensates the

TABLE 4.1: **Experimental results after post-processing.**

ν	S	I	B_1B_1	B_1B_2	B_3B_2	B_3B_1	n_v
1	$\|E\rangle_s$	$\|E\rangle_i$	3,030	2,863	2,828	2,810	11,531
2	$\|E\rangle_s$	$\|L\rangle_i$	21	19	30	21	91
3	$\|L\rangle_s$	$\|E\rangle_i$	12	20	19	10	61
4	$\|L\rangle_s$	$\|L\rangle_i$	2,558	2,760	2,429	2,500	10,247
5	$\|L\rangle_s$	$\|B_1\rangle_i$	2,778	-	-	2,727	5,505
6	$\|E\rangle_s$	$\|B_1\rangle_i$	2,998	-	-	2,682	5,680
7	$\|B_1\rangle_s$	$\|B_1\rangle_i$	10,511	-	-	-	10,511
8	$\|B_3\rangle_s$	$\|B_1\rangle_i$	-	-	-	5,771	5,771
9	$\|B_3\rangle_s$	$\|E\rangle_i$	-	-	2,570	2,512	5,082
10	$\|B_3\rangle_s$	$\|L\rangle_i$	-	-	2,761	2,811	5,572
11	$\|B_3\rangle_s$	$\|B_2\rangle_i$	-	-	10,007	-	10,007
12	$\|E\rangle_s$	$\|B_2\rangle_i$	-	2,729	2,671	-	5,400
13	$\|L\rangle_s$	$\|B_2\rangle_i$	-	2,777	2,631	-	5,408
14	$\|B_1\rangle_s$	$\|B_2\rangle_i$	-	6,154	-	-	6,154
15	$\|B_1\rangle_s$	$\|E\rangle_i$	2,811	2,752	-	-	5,563
16	$\|B_1\rangle_s$	$\|L_i\rangle$	2,840	2,833	-	-	5,673

TABLE 4.2: S and I represent measurement basis for signal and idler photon, respectively. B_1, B_2 and B_3 in the first row represent the different phase settings for each interferometer. A dash (-) indicates coincidences are not obtained for a basis state in the corresponding phase setting. The n_v column contains the total counts used for QST.

fact that the photons are less likely to be measured in the $|E\rangle_x$ and $|L\rangle_x$ time-basis states than the superposition states. It can be seen that the photons are highly correlated in the time-basis, with total counts of 10.2-11.5k for $|E\rangle_s|E\rangle_i$ and $|L\rangle_s|L\rangle_i$ and <100 for $|E\rangle_s|L\rangle_i$ and $|L\rangle_s|E\rangle_i$. These remaining counts are thought to be noise contributed by detector dark counts, Raman noise and multi-photon noise. In the other measurement bases, the counts are evenly distributed at around 5-6k, with the exception of $|B_1\rangle_s|B_1\rangle_i$ and $|B_3\rangle_s|B_2\rangle_i$, where constructive photon interference between the two components of the state boosts the counts to 10-10.5k. The coincidence rate of each combination is around 7 Hz which could be improved four-fold by placing detector at the unused outputs of the signal and idler UMZIs. Each channel has a collection efficiency of around 16 dB, including 3-4 dB from Filter2 and 3, 3 dB from the UMZI, 3-4 dB coupling loss to fibre, 2 dB loss from off chip filters, 1 dB loss from the PC, and 3 dB loss from detector inefficiency. This suggests an entangled pair generation rate of 45 kHz, around 10^{-3} pairs per pump pulse. Considering its potential applications in quantum network, further improvements are required to significantly boost the coincidence rate. This could include the use of a ring resonator to enhance the pair generation rate for a given pump power. Other possibilities include integrating low-loss and high isolation (>95 dB) filters [236], increasing the pump repetition rate [237], and integrating high-efficiency detector (or number-resolving detector) [224]. The mode-matching to fibre could also be considerably improved using inverse tapers of the output waveguides or polymer mode-converters [238].

First the results in the final column of Table 4.2 are used to carry out a linear reconstruction of the density matrix. The eigenvalues of this density matrix are 0.8742, 0.1153, 0.0267 and -0.0162. The presence of a slightly negative eigenvalue implies that an unphysical density matrix is obtained. This could be the result of statistical errors or fluctuations in the settings of the interferometer phases. A maximum likelihood estimation approach is adopted to find the physical density matrix which best fits the experimental results [14, 15]. The new eigenvalues are 0.9081, 0.0917, 0.0002 and 0 and the density matrix has $91 \pm 0.7\%$ fidelity compared with the ideal state, as shown in Figure 4.16(a) and Figure 4.16(b). This is consistent with the photon interference visibility of 88% measured in Figure 4.15 according to Eq.(3) in Ref.[239]. This fidelity is well above the classical threshold of 50%, as well as the 70.7% threshold to violate a Bell's inequality, confirming highly entangled photon pair are generated and analysed in this integrated Si_3N_4 circuits.

4.4.4 Discussion and conclusion

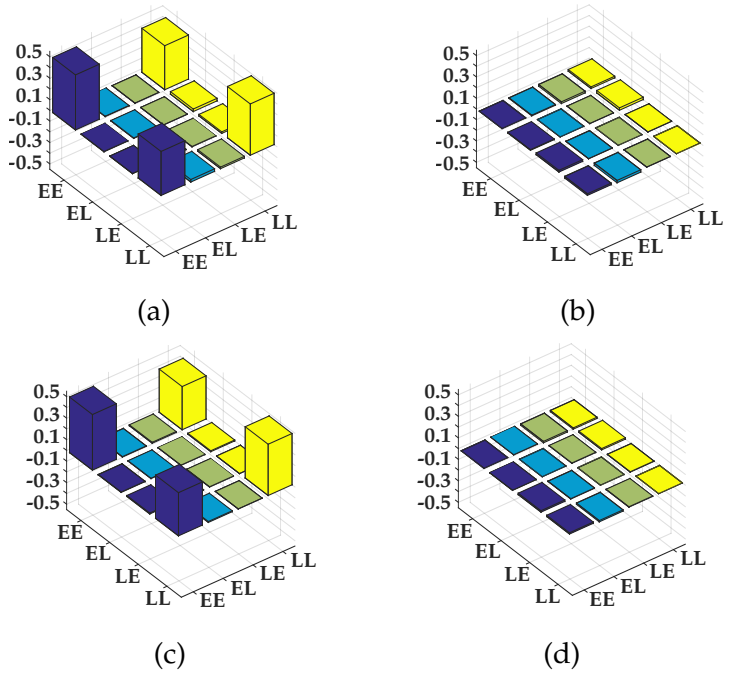

FIGURE 4.16: Density matrix of time-bin entangled photon pairs generated in two samples after maximum likelihood estimation. (a) and (b) show the real and imaginary parts of density matrix in the first sample, respectively. (c) and (d) show the real and imaginary parts of density matrix in the second sample, respectively. EE, EL, LE and LL represent $|E\rangle_s|E\rangle_i$, $|E\rangle_s|L\rangle_i$, $|L\rangle_s|E\rangle_i$ and $|L\rangle_s|L\rangle_i$, respectively.

The small deviation between the measured state and the ideal state is likely due to the influence of noise sources, such as SpRS noise in the Si_3N_4, and errors in the beam splitter ratios and phase-settings on the chip, partially due to

the thermal cross-talk between each heater. These problems could be significantly mitigated by cryogenic conditions and a dynamic feedback system [191, 240]. Compared with silicon nanowires, nonlinear photon pair generation in the double-stripe silicon nitride waveguides requires further improvement. Cryogenic temperatures and using ring resonator instead of spiral waveguides could significantly enhance the generation efficiency and the SNR [99]. With negligible Raman noise, a 100-fold improvement in count rate should be possible, above which multi-pair events are likely to contribute significant noise [94]. Another strategy to enhance the photon generation rate is to increase the pump repetition rate, where the upper limit is defined by the timing-jitter of the detection system, because the minimum delay to distinguish two time-bins is determined by the timing-jitter [237].

Apart from stability and scalability, reproducibility is another crucial advantage of CMOS compatible platforms. Another Si_3N_4 circuit on the same chip with an identical layout has been characterised in this work. The experimental results after post-processing are explained in Appendix A.2. After implementing maximum likelihood estimation, the density matrix is shown in Figure 4.16(c) and Figure 4.16(d). $89 \pm 0.6\%$ fidelity is obtained for the second sample and its eigenvalues are 0.9, 0.0983, 0.0016, 0. The 2% fidelity discrepancy between two sources originates from slightly different coupling ratios in UMZIs. The fidelity results of these two chips further confirm the reproducibility of this architecture. In the future, the external filters and SSPDs could also be integrated as high extinction filters and near-unity efficiency SSPDs have recently been demonstrated in a Si_3N_4 platform [236, 241]. This could allow scaling to more complicated functions, e.g. distributed quantum machine learning and multi-photon entangled state generation [242, 243]. Here, integrated Si_3N_4 circuits not only offer a compact and robust platform to generate entangled photons locally, but also allow entangled photons' transmission and analysis between separate photonic chips, such as using Port 10 and 11 shown in Figure 4.11 to analyse entangled photons from other nodes in the quantum network.

In this section, time-bin entangled photon pairs are generated and analysed for the first time on a single integrated photonic chip containing Si_3N_4 photonic circuits. The entangled states are analysed by QST and the maximum likelihood estimation indicates highly entangled photons are generated with $91 \pm 0.7\%$ fidelity compared with the ideal state. These results take another essential step toward the development of robust, scalable and cost-efficient quantum networks in the real world.

Contribution

I set up the experiment, took the data, and analysed the data under Dr. Bryn A. Bell, Dr. Chunle Xiong and Prof. Benjamin J. Eggleton's supervision. Dr. Andri Mahendra, and Prof. Philip H. W. Leong designed the FPGA circuits and interface with other components.

Chapter 5

Summary and Outlook

5.1 Summary

Photonic quantum technologies, which utilise the non-classical properties of single photons, are considered one of the leading strategies to demonstrate quantum advantages over classical paradigms. Applications include solving intractable computing problems and enabling unconditional information security. In Chapter 2, a systematic review of photonic quantum computing and quantum communication highlighted the major hurdles in each field. In particular, the lack of a high-efficiency single-photon source has hindered the development of photonic quantum computing. One of the remaining hurdles in photonic quantum communication lies in creating an integrated platform for compact and reconfigurable time-bin entanglement circuits. The work described in this thesis answers the following two questions:

1. Can we utilise the TMUX scheme to build a high-efficiency single-photon source?

2. Is silicon nitride a viable platform to develop an integrated time-bin entanglement chip?

The first question is posed as a result of a theoretical proposal published in 2011 [110]. This theoretical analysis suggested that TMUX can significantly enhance the single-photon generation probability by actively shifting heralded single photons from different temporal modes to fixed ones. Since 2015, a number of experimental demonstrations of TMUX showed a significant enhancement in single-photon generation probability [8, 66, 106, 196–200].

In Chapter 3, three different TMUX schemes have been proposed and experimentally demonstrated the feasibility of building a high-efficiency single-photon source. The first TMUX scheme interpreted in this chapter is ATM, which constantly shifts heralded single photons from different temporal modes into a fixed temporal mode. 100% enhancement of single-photon generation probability and 91% visibility of quantum interference is achieved in a proof-of-concept demonstration, thereby indicating that ATM is a potential approach for building a high-efficiency single-photon source. As an alternative scheme, TWDM is proposed for the case where only avalanche photodiodes are available for the heralding detection. Compared with superconducting single-photon detector, the avalanche photodiode is a more cost-efficient single-photon detector, but its

saturation margin is much smaller than the superconducting single-photon detector. In a TWDM scheme, the pump pulses are centred at different wavelengths with a constant wavelength interval between each other. These pump pulses are also interleaved with each other in the time domain, with a constant time interval. The phase-matching condition indicates that different wavelengths of heralding photons correspond to a fixed wavelength of heralded photons. The heralding photons are evenly distributed across multiple channels, instead of saturating one heralding channel. In a proof-of-principle demonstration, 90% enhancement of coincidence rate and 88% visibility of quantum interference indicate the TWDM scheme is another potential approach. The third TMUX scheme demonstrated in Chapter 3 is the RTM scheme, which allows an additional enhancement of N-photon generation probability over STM, such as ATM and TWDM, without increasing the complexity. Theoretical analysis indicates that the additional enhancement increases with the number of single-photon sources being multiplexed together. 90% additional enhancement obtained in a proof-of-principle demonstration agrees with the analytical value. 88% visibility of quantum interference shows heralded single photons are highly indistinguishable from one another after a joint synchronisation. At the end of Chapter 3, the potential limitation of the TMUX scheme with high repetition rate is identified as the timing-jitter of the detection system rather than nonlinear losses or Raman noise.

An integrated time-bin entanglement chip that includes a nonlinear photon source and linear analysis circuits would offer the possibility of developing a robust, scalable and cost-efficient quantum network. Meanwhile, the integrated solution imposes stringent requirements on the integration platform. In Chapter 4, a double-stripe silicon nitride waveguide is considered a viable platform to build such an integrated photonic chip for practical quantum network. Using a low-loss double-stripe silicon nitride waveguide, linear analysis circuits and an internal wavelength division multiplexer are fabricated in a single photonic chip. More than 86% visibility of photon interference with a constant single-photon rate in signal and idler channels confirm that highly entangled photons can be precisely controlled and analysed in such linear circuits. The nonlinearity of the double-stripe silicon nitride waveguide is characterised by a series of coincidence measurements. More than 185 kHz correlated photon pairs are generated in this silicon nitride waveguide. CAR>10 indicates 95% error free of QKD if we include such a nonlinear single-photon source [94]. After linear and nonlinear characterisations, we demonstrate time-bin entangled photon generation, noise suppression, wavelength division and entanglement analysis on a single photonic chip utilising low-loss double-stripe silicon nitride waveguide structures. 91% and 89% fidelity obtained from two identical circuits not only show that highly entangled photons are generated, manipulated and analysed in this photonic chip, but also verify the repeatability of this CMOS structure. These experimental results pave the way to build a practical quantum network.

The following two sections explain the future work to develop an integrated high-efficiency single-photon source and an integrated quantum node.

5.2 Outlook of an integrated high-efficiency single-photon source

Within the next few years, photonic quantum computing will play an important societal role. The major challenge of its practical applications lies in the development of a highly reliable and large-scale photonic quantum computing system. Building such a system based on free-space optical components is not a viable approach because of its lack of robustness, stability and scalability. In contrast, integrated quantum optics allows CMOS technologies to be harnessed and hence achieves multi-scale integration of passive and active components in a mature semiconductor-based platform that can be scaled for manufacturability [107, 155]. However, the major hurdle in creating a fully integrated photonic quantum computing system lies in an integrated high-efficiency single-photon source, as explained in Section 2.2. Although proof-of-principle demonstrations of TMUX explained in Chapter 3 show its potential, further improvements are required in three aspects to boost the generation probability $\mu > 0.75$ [64]. One aspect is an integrated optical switch with fast switching speed and ultra-low loss properties. The second aspect is an ultra-low loss waveguide for delay and transmission. The third aspect is a high-efficiency photon number resolving detector. The potential solutions are explained in the following sections.

5.2.1 Fast and low-loss optical switch

As explained in Section 3.2, the fast and low-loss optical switch is one of technical barriers in TMUX scheme. There are three potential solutions to build an integrated high-speed and low-loss optical switch. One is a graphene based modulator that harnesses the desirable properties of graphene to achieve a low energy threshold, broad-bandwidth and high speed switching [244, 245], as shown in Figure 5.1(a). The second solution is a hybrid switch that combines two types of optical switch— thermo-optic phase modulator (TOPM) and carrier-depletion modulator (CDM) [246]—as shown in Figure 5.1(b) [246]. The third strategy is using stress-optical effect to build an ultra-low loss modulator[206], as shown in Figure 5.1(c).

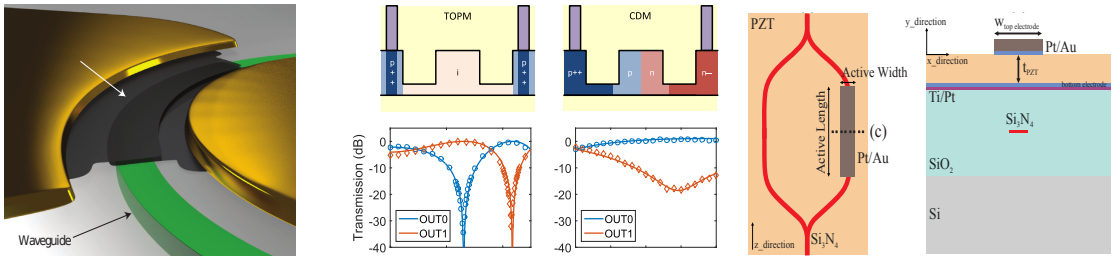

(a) (b) (c)

FIGURE 5.1: Different types of optical switch. (a) Graphene based switch [245]. (b) Hybrid switch [246]. (c) Stress-optical switch [67].

5.2.2 Ultra-low loss waveguide

An ultra-low loss waveguide is another core component for an integrated high-efficiency single-photon sources, as the MUX scheme requires transmission and delay lines. The standard silicon nanowire (220×460 nm) is unsuitable because of its 3 dB/cm propagation loss. As mentioned in Section 2.4.2, an etchless silicon nanowire has demonstrated 0.3 dB/cm propagation loss, which is comparable with other low-loss circuits. This could be a way to construct transmission and delay lines; However, a distinctive mode distribution between etchless and standard silicon nanowire, as shown in Figure 5.2 will adversely affect the coupling efficiency between linear circuits and nonlinear sources. Additional mode transformation components are required to enhance coupling efficiency.

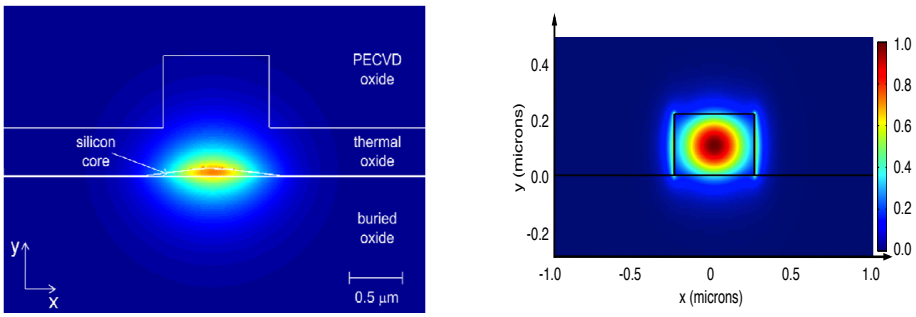

(a) (b)

FIGURE 5.2: Mode distribution in an etchless and standard silicon waveguide [68, 178]. (a) Mode distribution in an etchless waveguide [68]. (b) Mode distribution in a standard waveguide [178].

Another potential solution is a silicon nitride waveguide. In Section 4.4, nonlinear photon sources and linear delay lines have been demonstrated in a double-stripe Si_3N_4 waveguide, as shown in Figure 5.3(a). The experimental results indicate that the double-stripe Si_3N_4 waveguide is a viable structure; however, its low nonlinearity ($\gamma = 0.233/W/m$) will limit the performance of a large-scale quantum system. The other available structure is a Si_3N_4 rib waveguide, as shown in Figure 5.3(b) which has demonstrated high nonlinearity ($\gamma = 1/W/m$) and low-propagation loss (0.04 dB/cm) simultaneously [181]. To date, the stress limitation in Si_3N_4 material has been addressed through technical optimisations. A high-quality ($Q > 10^7$) ring resonator was used as a nonlinear source in a proof-of-principle demonstration [181]. The remaining work for the Si_3N_4 rib waveguide is to demonstrate large-scale linear circuits for single-photon transmission and switching.

The available platforms for constructing linear circuits also include silica waveguides, either fabricated by CMOS process or directly written by laser. Numerous experimental works show promising results [161–167], but its compactness is not as good as silicon or silicon nitride. Thus, the silica waveguide may not pose an optimal solution for photon transmission and switching.

(a) (b)

FIGURE 5.3: Double-stripe and rib Si_3N_4 waveguide. (a) SEM image of double-stripe Si_3N_4 waveguide [247]. (b) SEM image of rib Si_3N_4 waveguide [248].

5.2.3 High efficiency and photon number resolving detector

To date, there are several types of single-photon detectors (SPDs), such as photomultiplier, semiconductor SPD and superconducting SPD. In this section, we only discuss semiconductor SPD and superconducting SPD. After comparing their performance, an optimal solution for single-photon detection would be a superconducting SPD (SSPD) that simultaneously combines ultra-high detection rate ($>$ GHz), broad bandwidth, near-unity detection efficiency and ultra-low dark counts [73, 74, 249]. For photonic quantum computing to be useful in practice, complete system integration is essential. In this context, integrated SSPDs are one of the most attractive research objects. To date, several pioneering works have demonstrated SSPD on an integrated platform, using GaAs, silicon and Si_3N_4 [241, 250–252], as shown in Figure 5.4.

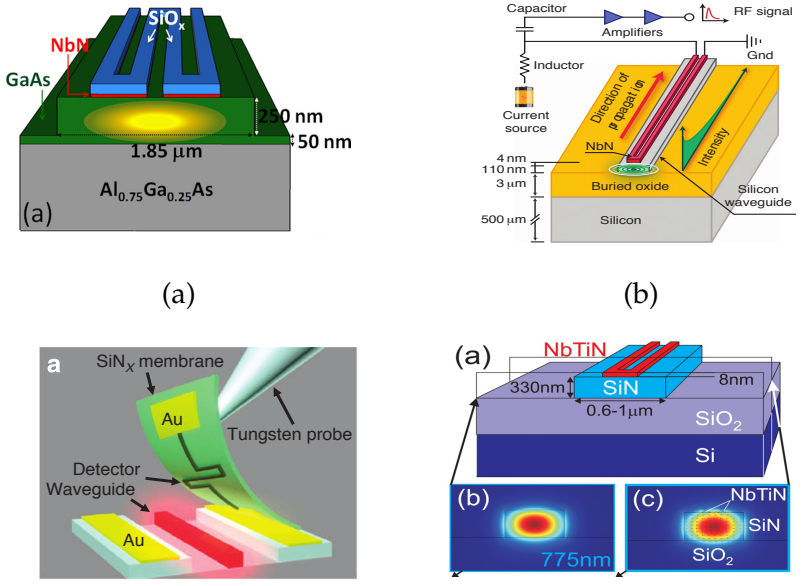

FIGURE 5.4: Illustration of SSPD on integrated platforms. (a) GaAs platform [251]. (b) Silicon platform [252]. (c) and (d) Si_3N_4 platform [241, 250]

The correct temporal information is a crucial element of TMUX, as explained in Section 3.5. If the jitter is comparable or even larger than the period of the temporal mode, it will result in an incorrect temporal mode detection. The other crucial aspect is a photon-number resolving detection, since single-photon pair generation is accompanied by multi-photon pair noise. The photon number detection has been demonstrated in two ways. One is to differentiate the output intensity, which is proportional to the number of input single photons, such as the superconducting transition edge sensor shown in Figure 5.5(a) [253]. The other approach is using a cascade of beam splitter to identify the photon number, as shown in Figure 5.5(b) [254]. The remaining works are to demonstrate broad bandwidth, near-unity detection efficiency, photon-number resolving, low timing-jitter and dark counts simultaneously in an integrated SSPD.

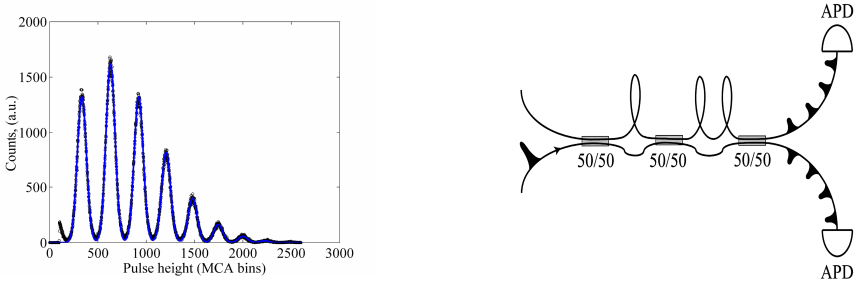

(a) (b)

FIGURE 5.5: Illustration of two types of photon number resolving detector. (a) Superconducting transition edge sensor [73]. (b) Splitting photon detector [254].

5.2.4 Frequency multiplexing scheme

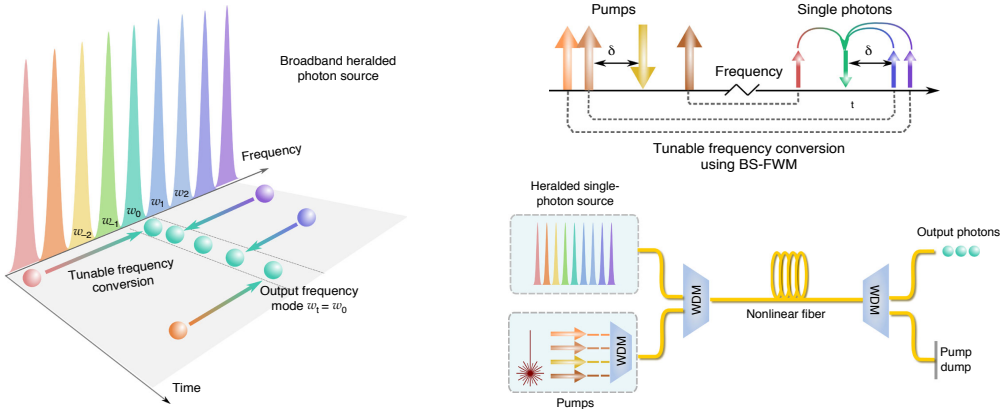

(a) (b)

FIGURE 5.6: Schematic of FMUX [8]. (a) Illustration of frequency conversion. (b) Principle of BS-FWM and the experiment method.

Recent works have demonstrated a more resource-efficient MUX scheme-FMUX, compared with SMUX and TMUX [8, 255]. Figure 5.6(a) shows the schematic

of FMUX. Although the heralded single photons are generated with a broad bandwidth, each photon is deterministically converted into an identical single wavelength. The underlying principle (BS-FWM) and experimental method are illustrated in Figure 5.6(b). Based on the wavelength of each heralding photon, the corresponding pump wavelength is actively reconfigured. The advantage of FMUX is a fixed loss, irrespective of the number of multiplexed frequency modes. Experimental results show a significant enhancement in the photon rate; however, deterministic BS-FWM in an integrated circuit is a nontrivial task. The main obstacles include dispersion engineering and linear/nonlinear losses. Si_3N_4 could be one of potential platforms to implement FMUX because of its desirable properties, such as large transparency window, high nonlinearity, negligible nonlinear loss and low-propagation loss [248, 256].

Once an integrated high-efficiency single-photon source is developed, a large-scale photonic quantum computing system that demonstrates quantum advantages over classical computing on specific problems will be a plausible target.

5.3 Outlook of an integrated quantum node

Developing a global-scale quantum network in a real-world application is a long-term project. As explained in the Section 2.3.3, the EB protocol is a more promising strategy because it not only provides unconditional information security, as with the PM protocol, but also allows higher capacity and is more robust than the PM protocol [243]. Building such a quantum network relies on the composition of basic units in an integrated quantum node that can generate, transmit, analyse and store entangled photon qubits in a broad bandwidth. However, some of the core technologies are not mature, such as quantum memory and single-photon wavelength conversion. This section briefly discusses the potential solutions to build an integrated quantum memory and high-efficiency single-photon wavelength conversion unit.

5.3.1 Quantum memory unit

Intermediate quantum nodes are the basic building blocks for a global-scale quantum network. The fundamental functionalities of each node are generating, manipulating and analysing entangled photons, as demonstrated in Chapter 4. The practical barrier of building a global-scale quantum network is the transmission loss, which exponentially increases with the length of fibre link. The maximum length is reached when the key rate becomes comparable to the noise level, at which point a useful key cannot be extracted [257]. A promising way to elevate the useful key rate and extend the transmission distance is integrating quantum memories in each intermediate node [258]. Figure 5.7 illustrates a quantum link comprising separate channels that are connected by intermediate nodes. The pink circles represent the entangled photons that are distributed between Nodes A, B, C and D. As a result of the inevitable transmission loss and non-unity storage

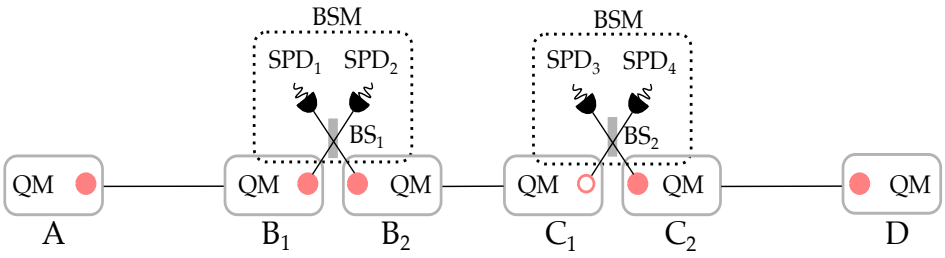

FIGURE 5.7: Illustration of a quantum link with quantum memory units. A, B, C and D represent the quantum nodes. QM:quantum memory unit; BS: beam splitter; SPD: single-photon detector; BSM: Bell-state measurement. The empty and solid circles represent entangled photons dissipated and stored in the quantum memory, respectively.

efficiency, the entangled photons are probabilistically stored in quantum memories. The solid and empty circles represent the stored and dissipated photons, respectively. If parts of entangled photons are dissipated during the key distribution process, such as C_1, its entangled partner in B_2 will be dumped immediately. The entanglement link between B_2 and C_1 requires additional entanglement distributions until two quantum memories (B_2 and C_1) store two entangled photons. Meanwhile, other parts of the quantum link are preserved as entangled photons are stored in the quantum memory units. Once the aforementioned link is rebuilt, the photon stored in quantum memory B_1, B_2, C_1 and C_2 will be released and implement bell state measurement within the Node B and C. The entanglement state between two remote nodes A and D will be heralded by the results of bell state measurement [26, 115, 141, 153, 154, 239, 243, 259, 260].

Figure 5.7 shows the significance of quantum memory units in a large-scale quantum network. To date, quantum memory has been demonstrated in a number of platforms, such as rare-earth ions in solids [261, 265], nitrogen-vacancy centre in diamonds [262, 265, 266], quantum dots [36, 267], trapped rubidium (Rb) atoms [263, 268, 269], cesium vapour [264] and erbium ions [270, 271], as partially shown in Figure 5.8. Moreover, a practical quantum network prefers an integrated quantum memory unit because of its scalability and robustness. Among these potential platforms, nitrogen-vacancy centres in a diamond waveguide would be one of several promising solutions because of its high fidelity [272], large bandwidth, and greater than ms storage time [273]. A pioneer work demonstrated a scalable diamond waveguide integrated in Si_3N_4 platform, as shown in Figure 5.8(b) [262]. A visible wavelength used in this work can be shifted into a telecom-band by utilising Raman interaction [274] or frequency conversion [275].

5.3.2 Single-photon wavelength conversion unit

In the short-term future, a large-scale quantum network will include numbers of end-users. The basic requirement is simultaneous key transmission without interference. Since the encryption keys are encoded on single photons, nonlinear effects, such as SPM and XPM, will play a negligible role during the key

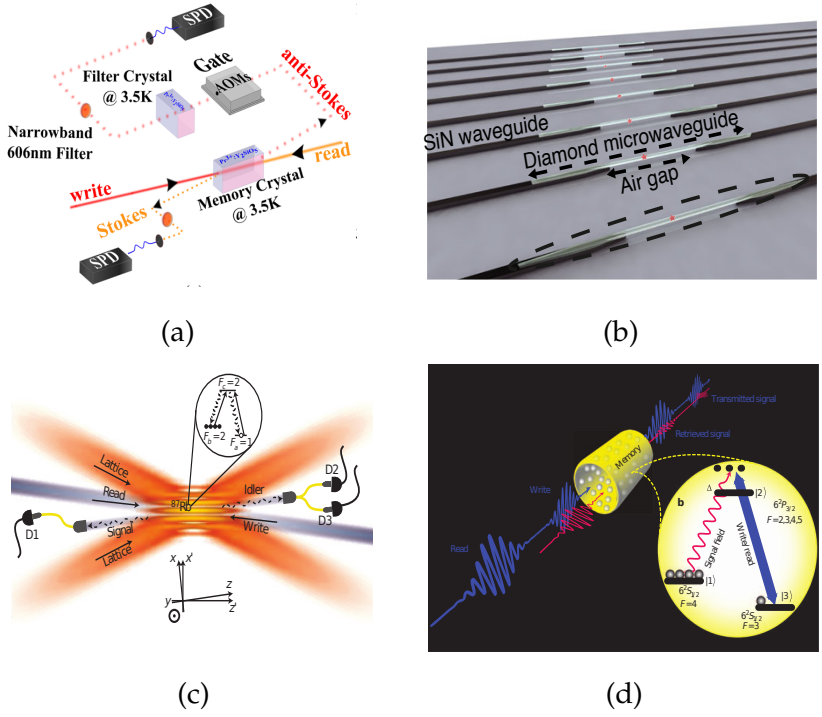

FIGURE 5.8: quantum memory in different platforms. (a) Rare-earth ion in crystal [261]. (b) nitrogen-vacancy centre in diamond [262]. (c) Rb atom [263]. (d) Caesium vapour [264].

transmission. The wavelength multiplexing scheme is the optimal way to transmit keys simultaneously within a broad bandwidth. Meanwhile, the wavelength multiplexing scheme also introduces another technical challenge-namely, single-photon wavelength conversion, since each end-user may use a different wavelength. In this case, a deterministic single-photon wavelength conversion without deteriorating the coherent state of entangled photons is key. Over the last decade, the single-photon wavelength conversion has been demonstrated on different platforms [8, 196, 248, 275–282]. All these pioneer works harness nonlinear optical effects to achieve frequency conversion at the single-photon level. For instance, single side-band (SSB) frequency modulation, optomechanical frequency shifter and BS-FWM use the $\chi^{(2)}$ nonlinear effect, optomechanical interaction and $\chi^{(3)}$ nonlinear effect, respectively [8, 280, 281].

Figure 5.9(a) shows the schematic of SSB frequency modulation [280]. The single-photon wavelength is translated by a frequency modulator driven by a radio frequency signal. After configuring four phase modulators with a specific phase, a new frequency $(\omega - \omega_m)$ appears as a side-band of the original input, ω. The bottom image of Figure 5.9(a) explicitly shows 25 GHz frequency shift after the SSB modulation. The single photons after the frequency conversion are verified by a HOM quantum interference, which clearly indicates the success of frequency conversion. The limitations of SSB phase modulation include non-unity conversion and limited shifting range.

The second approach to translate single-photon wavelength is mechanical deformation, as shown in Figure 5.9(b). The variation of optical length induced by

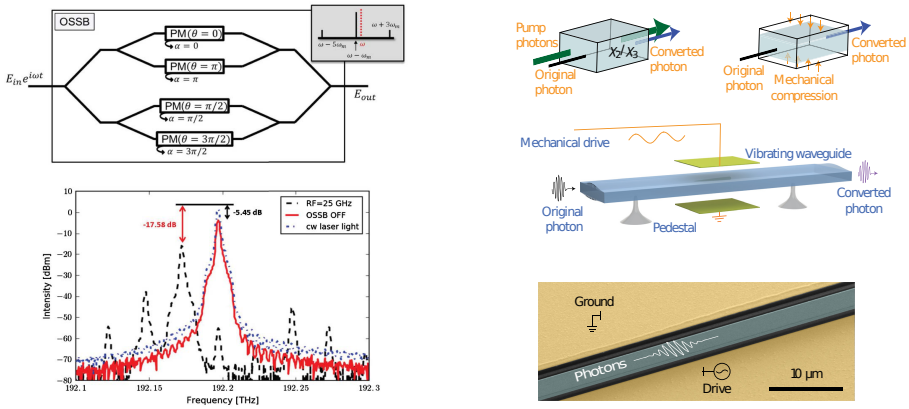

(a) (b)

FIGURE 5.9: Schematic of single-photon wavelength conversion. (a) Single side-band frequency modulation [280]. (b) Optomechanical frequency shifter [281].

mechanical deformation will result in a frequency shift. In a pioneering work, nearly 100% conversion efficiency was achieved over 150 GHz, as well as indistinguishability [281]. The mechanical deformation offers a robust and flexible way to realise 100% conversion efficiency without facing the obstacles of noise photons, narrow bandwidth and optical filtering. Mechanical deformation is one of several promising approaches to seamlessly converge multiple end-users with variable wavelengths.

The third approach is BS-FWM which harnesses third-order nonlinearity to realise deterministic single-photon wavelength conversion, as shown in Figure 5.6 [8]. In Section 5.2.4, near 100% conversion efficiency has been demonstrated in a dispersion engineered nonlinear fibre. Theoretical investigation indicates that high-efficiency single-photon conversion in an integrated circuit is feasible if the dispersion and pump wavelengths are well engineered [283]. Compared with phase modulation and optomechanical shifters, BS-FWM allows much broader bandwidth, as well as high conversion efficiency. Although the existence of pump pulses will result in additional nonlinear losses, this can be addressed by a suitable integration platform, such as Si_3N_4.

In the future, once time-bin entanglement circuits, high-efficiency quantum memories and single-photon wavelength conversion units are demonstrated in an integrated platform, building a global-scale quantum network will be a feasible project.

Appendix A

Appendix

A.1 The supplementary information for active temporal multiplexing

A.1.1 The synchronisation process

In synchronisation (I), a digital delay generator (DG1 in the full setup, see Figure 3.6) is used between the superconducting single-photon detector (SSPD) heralding signal output and field programmable gate array (FPGA). By doing an AND operation between the heralding detection signals and the FPGA clock, and comparing the FPGA output count rate with that on the SSPD software, we can find the correct delay using DG1. Once this is done, The synchronisation process is proceeded to synchronisation (II).

To simplify synchronisation (II), the FPGA is configured according to a heralding event, the three binary-digit output is latched until the next heralding event occurred. For example, if a photon pair is generated in time-bin t_1, '000' is applied to the switches until the next pair is generated. If the next pair is generated in time-bin t_4, the output of the FPGA will change to '110'. In this way, only the switching signals that control switch (SW1 in the full setup, see Figure 3.6) with the incoming photons needs a synchronisation, because once photons pass through SW1, they are routed directly through SW2 and SW3 that are always under the correct logic control, see Figure 3.6. Additionally, one temporal mode synchronisation is sufficient to ensure the synchronisation of other three modes, because the relative delay between heralding and heralded events is the same no matter in which time-bin the photon pairs are generated. As the initial input status to the switches is '0', the pump on the clock of either t_2 or t_4 is chosen for synchronisation because only these two pump modes require a logic '1' input to SW1 and are possible for the delay alignment. In the measurement, only the channel of fibre couplers (FCs) with 25 ns optical delays (i.e. t_2) is connected and applied a constant output '101' from the FPGA to the switches to take a coincidence measurement as the reference. Then a digital delay generator (DG2 in the full setup, see Figure 3.6) is added between the logic output pin1 of the FPGA and SW1. the delay of the switching signals to SW1 is continuously tuned via DG2 and measure the coincidences. By trial and error, the correct delay is found when the measured coincidences matched with the reference measurement. This delay is then double confirmed by coincidence measurements for the other three temporal pump modes. Note that DG2 only responds when the output logic from

pin1 changes from '0' to '1' and keeps SW1 at the 'switching' status for 100 ns, so the use of DG2 here is optional as long as the signals from the FPGA are sent to all three switches before the incoming photons. The advantages of applying DG2 for synchronisation are the accurate control to the switching network and thus can route some unheralded photons (i.e., pairs are generated but the heralding photons have been lost) to the dumped port.

In synchronisation (III), the optical fibres with the lengths providing delays of approximately 25 ns and 50 ns are manually cut and spliced the fibres in paths (c) and (d) of the switching network, as shown in Figure 3.6; and then off-the-shelf fibre-integrated optical tunable delay line (OTDL) are used with a tuning step of 1 ps in three channels of the fibre couplers (FCs) for MUX the pump to match the delays in the switching network. Compared with directly using OTDL in the switching network, this arrangement minimised the losses of the multiplexed heralded photons.

A.1.2 Polarisation management

Due to the use of non-polarisation maintaining components in the switching network, photons with the same polarisation at the input generally will have different polarisation at the output if they go through different optical paths. Depending on in which time-bin the heralded photons are generated, they go through the combination of optical paths shown in Figure 3.6, t_1:(a)+(b), t_2:(c)+(b), t_3:(a)+(d), t_4:(c)+(d). Adding one polarisation controller (PC) in each of (c) and (d) is sufficient to maintain the polarisation of the photons. For example, the photons from t_1 and t_2 share the path (b), the PC in (c) can always adjust the polarisation of photons to be the same to those in (a). Then (c) becomes equal to (a) in terms of polarisation. The same rule applies to (d) and (b) and thus photons from all time-bins will have the same polarisation at the output of the switching network.

A.1.3 Delay management

The delay management procedure described in Appendix A.1.1 aligns the photon arrival time to an accuracy of 1 ns, which is determined by the time resolution of the coincidence measurement system. The fourfold HOM interference requires the delay alignment at the accuracy of photons' coherence time which is of the order of the pump pulse width 10 ps. The measurements are taken in the following steps. First, only the channel of the 1-to-4 FCs without optical delay lines (ODLs) is connected as the pump of the MUX source so that photons are always generated in t_1. By varying the delay of OTDL4 in the second source (see Figure 3.6), the fine delay is adjusted via twofold HOM interference and fixed the delay on OTDL4. Second, the channel of the 1-to-4 FCs with OTDL1, OTDL2, or OTDL3, is connected in turn to determine and fix the fine delays for them via twofold measurements. Third, all four channels of the 1-to-4 FCs are connected to obtain the fully multiplexed source and take the twofold and fourfold HOM interference measurements by varying the fine delay on OTDL4.

A.2 The supplementary information for the second circuits

TABLE A.1: **Experimental results after post-processing.**

v	S	I	B_1B_1	B_1B_2	B_3B_2	B_3B_1	n_v
1	$\|E\rangle_s$	$\|E\rangle_i$	1,928	2,113	1,770	1,784	7,595
2	$\|E\rangle_s$	$\|L\rangle_i$	15	15	13	12	55
3	$\|L\rangle_s$	$\|E\rangle_i$	6	9	10	12	37
4	$\|L\rangle_s$	$\|L\rangle_i$	1,708	1,674	1,803	1,837	7,022
5	$\|L\rangle_s$	$\|B_1\rangle_i$	1,847	-	-	1,686	3,533
6	$\|E\rangle_s$	$\|B_1\rangle_i$	1,869	-	-	1,887	3,756
7	$\|B_1\rangle_s$	$\|B_1\rangle_i$	6,735	-	-	-	6,735
8	$\|B_3\rangle_s$	$\|B_1\rangle_i$	-	-	-	3,923	3,923
9	$\|B_3\rangle_s$	$\|E\rangle_i$	-	-	1,720	1,794	3,514
10	$\|B_3\rangle_s$	$\|L\rangle_i$	-	-	1,828	1,963	3,791
11	$\|B_3\rangle_s$	$\|B_2\rangle_i$	-	-	6,706	-	6,706
12	$\|E\rangle_s$	$\|B_2\rangle_i$	-	1,968	1,902	-	3,870
13	$\|L\rangle_s$	$\|B_2\rangle_i$	-	1,825	1,685	-	3,510
14	$\|B_1\rangle_s$	$\|B_2\rangle_i$	-	3,846	-	-	3,846
15	$\|B_1\rangle_s$	$\|E\rangle_i$	1,905	2,031	-	-	3,936
16	$\|B_1\rangle_s$	$\|L_i\rangle$	1,814	1,745	-	-	3,559

TABLE A.2: S and I represent measurement basis for signal and idler photon, respectively. B_1, B_2 and B_3 in the first row represent the different phase settings for each interferometer. A dash (-) indicates coincidences are not obtained for a basis state in the corresponding phase setting. The n_v column contains the total counts used for QST.

The section presents the coincidence results obtain in the second circuits on the same chip after post-processing, as shown in Table A.2. The photons in the time-basis are highly correlated, with total counts of 7.0-7.5k for $|E\rangle_s |E\rangle_i$ and $|L\rangle_s |L\rangle_i$ and <60 for $|E\rangle_s |L\rangle_i$ and $|L\rangle_s |E\rangle_i$. These remaining counts are thought to be noise contributed by detector dark counts, Raman noise and multi-photon noise. In the other measurement bases, the counts are evenly distributed at around 3.0k, with the exception of $|B_1\rangle_s |B_1\rangle_i$ and $|B_3\rangle_s |B_2\rangle_i$, where constructive photon interference between the two components of the state boosts the counts to 6.7k.

Bibliography

[1] J. C. Maxwell, "A Dynamical Theory of the Electromagnetic Field", Proceedings of the Royal Society of London **13**, 531–536 (1864).

[2] A. Einstein, "Über einen die Erzeugung und Verwandlung des Lichtes betreffenden heuristischen Gesichtspunkt", Annalen der Physik **322**, 132–148 (1905).

[3] A. H. Compton, "A Quantum Theory of the Scattering of X-rays by Light Elements", Physical Review **21**, 483–502 (1923).

[4] R. Hanbury Brown and R. Q. Twiss, "A Test of a New Type of Stellar Interferometer on Sirius", Nature **178**, 1046–1048 (1956).

[5] M. Collins, C. Xiong, I. Rey, T. Vo, J. He, S. Shahnia, C. Reardon, T. Krauss, M. Steel, A. Clark, and B. Eggleton, "Integrated spatial multiplexing of heralded single-photon sources", Nature Communications **4**, 1–7 (2013).

[6] X. Ding, Y. He, Z.-C. Duan, N. Gregersen, M.-C. Chen, S. Unsleber, S. Maier, C. Schneider, M. Kamp, S. Höfling, C.-Y. Lu, and J.-W. Pan, "On-Demand Single Photons with High Extraction Efficiency and Near-Unity Indistinguishability from a Resonantly Driven Quantum Dot in a Micropillar", Physical Review Letters **116**, 020401 (2016).

[7] N. Somaschi, V. Giesz, L. De Santis, J. C. Loredo, M. P. Almeida, G. Hornecker, S. L. Portalupi, T. Grange, C. Antón, J. Demory, C. Gómez, I. Sagnes, N. D. Lanzillotti-Kimura, A. Lemaítre, A. Auffeves, A. G. White, L. Lanco, and P. Senellart, "Near-optimal single-photon sources in the solid state", Nature Photonics **10**, 340–345 (2016).

[8] C. Joshi, A. Farsi, S. Clemmen, S. Ramelow, and A. L. Gaeta, "Frequency multiplexing for quasi-deterministic heralded single-photon sources", Nature Communications **9**, 847 (2018).

[9] C. K. Hong, Z. Y. Ou, and L. Mandel, "Measurement of subpicosecond time intervals between two photons by interference", Physical Review Letters **59**, 2044–2046 (1987).

[10] E. Knill, R. Laflamme, and G. J. Milburn, "A scheme for efficient quantum computation with linear optics", Nature **409**, 46–52 (2001).

[11] J. W. Silverstone, R. Santagati, D. Bonneau, M. J. Strain, M. Sorel, J. L. O'Brien, and M. G. Thompson, "Qubit entanglement between ring-resonator photon-pair sources on a silicon chip", Nature Communications **6**, 7948 (2015).

[12] C. Reimer, M. Kues, P. Roztocki, B. Wetzel, F. Grazioso, B. E. Little, S. T. Chu, T. Johnston, Y. Bromberg, L. Caspani, D. J. Moss, and R. Morandotti, "Generation of multiphoton entangled quantum states by means of integrated frequency combs", Science **351**, 1176–1180 (2016).

[13]C. Xiong, X. Zhang, A. Mahendra, J. He, D.-Y. Choi, C. J. Chae, D. Marpaung, A. Leinse, R. G. Heideman, M. Hoekman, C. G. H. Roeloffzen, R. M. Oldenbeuving, P. W. L. van Dijk, C. Taddei, P. H. W. Leong, and B. J. Eggleton, "Compact and reconfigurable silicon nitride time-bin entanglement circuit", Optica **2**, 724 (2015).

[14]D. F. V. James, P. G. Kwiat, W. J. Munro, and A. G. White, "Measurement of qubits", Physical Review A **64**, 052312 (2001).

[15]H. Takesue and Y. Noguchi, "Implementation of quantum state tomography for time-bin entangled photon pairs", Optics Express **17**, 10976 (2009).

[16]C. H. Bennett, "Quantum Information and Computation", Physics Today **48**, 24–30 (1995).

[17]J. Preskill, "Quantum Computing in the NISQ era and beyond", arXiv, 1–22 (2018).

[18]R. P. Feynman, "Simulating physics with computers", International Journal of Theoretical Physics **21**, 467–488 (1982).

[19]P. Kok, W. J. Munro, K. Nemoto, T. C. Ralph, J. P. Dowling, and G. J. Milburn, "Linear optical quantum computing with photonic qubits", Reviews of Modern Physics **79**, 135–174 (2007).

[20]H. Wang, Y.-M. He, Y.-H. Li, Z.-E. Su, B. Li, H.-L. Huang, X. Ding, M.-C. Chen, C. Liu, J. Qin, J.-P. Li, Y.-M. He, C. Schneider, M. Kamp, C.-Z. Peng, S. Höfling, C.-Y. Lu, and J.-W. Pan, "High-efficiency multiphoton boson sampling", Nature Photonics **11**, 361–365 (2017).

[21]P. W. Shor, "Polynomial-Time Algorithms for Prime Factorization and Discrete Logarithms on a Quantum Computer", SIAM Journal on Computing **26**, 1484–1509 (1997).

[22]D. R. Simon, "On the Power of Quantum Computation", SIAM Journal on Computing **26**, 1474–1483 (1997).

[23]T. D. Ladd, F. Jelezko, R. Laflamme, Y. Nakamura, C. Monroe, and J. L. O'Brien, "Quantum computers", Nature **464**, 45–53 (2010).

[24]L. K. Grover, "Quantum Mechanics Helps in Searching for a Needle in a Haystack", Physical Review Letters **79**, 325–328 (1997).

[25]D. S. Abrams and S. Lloyd, "Simulation of Many-Body Fermi Systems on a Universal Quantum Computer", Physical Review Letters **79**, 2586–2589 (1997).

[26]N. Gisin and R. Thew, "Quantum communication", Nature Photonics **1**, 165–171 (2007).

[27]D. Deutsch, "Quantum Theory, the Church-Turing Principle and the Universal Quantum Computer", Proceedings of the Royal Society A: Mathematical, Physical and Engineering Sciences **400**, 97–117 (1985).

[28]D. P. DiVincenzo, "The Physical Implementation of Quantum Computation", Fortschritte der Physik **48**, 771–783 (2000).

[29]J. B. Spring, B. J. Metcalf, P. C. Humphreys, W. S. Kolthammer, X.-M. Jin, M. Barbieri, A. Datta, N. Thomas-Peter, N. K. Langford, D. Kundys, J. C. Gates, B. J. Smith, P. G. R. Smith, and I. A. Walmsley, "Boson Sampling on a Photonic Chip", Science **339**, 798–801 (2013).

[30]M. A. Broome, A. Fedrizzi, S. Rahimi-Keshari, J. Dove, S. Aaronson, T. C. Ralph, and A. G. White, "Photonic Boson Sampling in a Tunable Circuit", Science **339**, 794–798 (2013).

[31]M. Tillmann, B. Dakić, R. Heilmann, S. Nolte, A. Szameit, and P. Walther, "Experimental boson sampling", Nature Photonics **7**, 540–544 (2013).

[32]Y. He, X. Ding, Z.-E. Su, H.-L. Huang, J. Qin, C. Wang, S. Unsleber, C. Chen, H. Wang, Y.-M. He, X.-L. Wang, W.-J. Zhang, S.-J. Chen, C. Schneider, M. Kamp, L.-X. You, Z. Wang, S. Höfling, C.-Y. Lu, and J.-W. Pan, "Time-Bin-Encoded Boson Sampling with a Single-Photon Device", Physical Review Letters **118**, 190501 (2017).

[33]J. I. Cirac and P. Zoller, "Quantum Computations with Cold Trapped Ions", Physical Review Letters **74**, 4091–4094 (1995).

[34]D. Kielpinski, C. Monroe, and D. J. Wineland, "Architecture for a large-scale ion-trap quantum computer", Nature **417**, 709–711 (2002).

[35]C. Monroe and J. Kim, "Scaling the Ion Trap Quantum Processor", Science **339**, 1164–1169 (2013).

[36]R. Hanson, L. P. Kouwenhoven, J. R. Petta, S. Tarucha, and L. M. K. Vandersypen, "Spins in few-electron quantum dots", Reviews of Modern Physics **79**, 1217–1265 (2007).

[37]M. Veldhorst, H. G. J. Eenink, C. H. Yang, and A. S. Dzurak, "Silicon CMOS architecture for a spin-based quantum computer", Nature Communications **8**, 1766 (2017).

[38]L. DiCarlo, J. M. Chow, J. M. Gambetta, L. S. Bishop, B. R. Johnson, D. I. Schuster, J. Majer, A. Blais, L. Frunzio, S. M. Girvin, and R. J. Schoelkopf, "Demonstration of two-qubit algorithms with a superconducting quantum processor", Nature **460**, 240–244 (2009).

[39]R. Barends, A. Shabani, L. Lamata, J. Kelly, A. Mezzacapo, U. L. Heras, R. Babbush, A. G. Fowler, B. Campbell, Y. Chen, Z. Chen, B. Chiaro, A. Dunsworth, E. Jeffrey, E. Lucero, A. Megrant, J. Y. Mutus, M. Neeley, C. Neill, P. J. J. O'Malley, C. Quintana, P. Roushan, D. Sank, A. Vainsencher, J. Wenner, T. C. White, E. Solano, H. Neven, and J. M. Martinis, "Digitized adiabatic quantum computing with a superconducting circuit", Nature **534**, 222–226 (2016).

[40]R. Barends, J. Kelly, A. Megrant, A. Veitia, D. Sank, E. Jeffrey, T. C. White, J. Mutus, A. G. Fowler, B. Campbell, Y. Chen, Z. Chen, B. Chiaro, A. Dunsworth, C. Neill, P. O'Malley, P. Roushan, A. Vainsencher, J. Wenner, A. N. Korotkov, A. N. Cleland, and J. M. Martinis, "Superconducting quantum circuits at the surface code threshold for fault tolerance", Nature **508**, 500–503 (2014).

[41]D. G. Cory, A. F. Fahmy, and T. F. Havel, "Ensemble quantum computing by NMR spectroscopy", Proceedings of the National Academy of Sciences **94**, 1634–1639 (1997).

[42]L. M. K. Vandersypen, M. Steffen, G. Breyta, C. S. Yannoni, M. H. Sherwood, and I. L. Chuang, "Experimental realization of Shor's quantum factoring algorithm using nuclear magnetic resonance", Nature **414**, 883–887 (2001).

[43]J. L. O'Brien, "Optical Quantum Computing", Science **318**, 1567–1570 (2007).

[44]J. O'Brien, B. Patton, M. Sasaki, and J. Vučković, "Focus on integrated quantum optics", New Journal of Physics **15**, 035016 (2013).

[45]H. Wang, W. Li, X. Jiang, Y.-M. He, Y.-H. Li, X. Ding, M.-C. Chen, J. Qin, C.-Z. Peng, C. Schneider, M. Kamp, W.-J. Zhang, H. Li, L.-X. You, Z. Wang, J. P. Dowling, S. Hofling, C.-Y. Lu, and J.-W. Pan, "Toward Scalable Boson Sampling with Photon Loss", arXiv **2**, 1–10 (2018).

[46]C. H. Bennett and D. P. DiVincenzo, "Quantum information and computation", Nature **404**, 247–255 (2000).

[47]H. Schmidt and A. Imamoglu, "Giant Kerr nonlinearities obtained by electromagnetically induced transparency", Optics Letters **21**, 1936 (1996).

[48]A. Imamoğlu, H. Schmidt, G. Woods, and M. Deutsch, "Strongly Interacting Photons in a Nonlinear Cavity", Physical Review Letters **79**, 1467–1470 (1997).

[49]S. Ferretti and D. Gerace, "Single-photon nonlinear optics with Kerr-type nanostructured materials", Physical Review B **85**, 033303 (2012).

[50]T. Volz, A. Reinhard, M. Winger, A. Badolato, K. J. Hennessy, E. L. Hu, and A. Imamoğlu, "Ultrafast all-optical switching by single photons", Nature Photonics **6**, 605–609 (2012).

[51]H. Sekoguchi, Y. Takahashi, T. Asano, and S. Noda, "Photonic crystal nanocavity with a Q-factor of 9 million", Optics Express **22**, 916 (2014).

[52]N. Matsuda, R. Shimizu, Y. Mitsumori, H. Kosaka, and K. Edamatsu, "Observation of optical-fibre Kerr nonlinearity at the single-photon level", Nature Photonics **3**, 95–98 (2009).

[53]J. Volz, M. Scheucher, C. Junge, and A. Rauschenbeutel, "Nonlinear π phase shift for single fibre-guided photons interacting with a single resonator-enhanced atom", Nature Photonics **8**, 965–970 (2014).

[54]A. V. Gorshkov, J. Otterbach, M. Fleischhauer, T. Pohl, and M. D. Lukin, "Photon-Photon Interactions via Rydberg Blockade", Physical Review Letters **107**, 133602 (2011).

[55]T. Peyronel, O. Firstenberg, Q.-Y. Liang, S. Hofferberth, A. V. Gorshkov, T. Pohl, M. D. Lukin, and V. Vuletić, "Quantum nonlinear optics with single photons enabled by strongly interacting atoms", Nature **488**, 57–60 (2012).

[56]O. Firstenberg, T. Peyronel, Q.-Y. Liang, A. V. Gorshkov, M. D. Lukin, and V. Vuletić, "Attractive photons in a quantum nonlinear medium", Nature **502**, 71–75 (2013).

[57]D. Paredes-Barato and C. S. Adams, "All-Optical Quantum Information Processing Using Rydberg Gates", Physical Review Letters **112**, 040501 (2014).

[58]J. H. Shapiro, "Single-photon Kerr nonlinearities do not help quantum computation", Physical Review A **73**, 062305 (2006).

[59]E. Knill, "Bounds on the probability of success of postselected nonlinear sign shifts implemented with linear optics", Physical Review A **68**, 064303 (2003).

[60]T. Rudolph, "Why I am optimistic about the silicon-photonic route to quantum computing", APL Photonics **2**, 030901 (2017).

[61]J. L. O'Brien, A. Furusawa, and J. Vučković, "Photonic quantum technologies", Nature Photonics **3**, 687–695 (2009).

[62]J. Carolan, C. Harrold, C. Sparrow, E. Martin-Lopez, N. J. Russell, J. W. Silverstone, P. J. Shadbolt, N. Matsuda, M. Oguma, M. Itoh, G. D. Marshall, M. G. Thompson, J. C. F. Matthews, T. Hashimoto, J. L. O'Brien, and A. Laing, "Universal linear optics", Science **349**, 711–716 (2015).

[63]J. C. Loredo, M. A. Broome, P. Hilaire, O. Gazzano, I. Sagnes, A. Lemaitre, M. P. Almeida, P. Senellart, and A. G. White, "Boson Sampling with Single-Photon Fock States from a Bright Solid-State Source", Physical Review Letters **118**, 130503 (2017).

[64]M. Varnava, D. E. Browne, and T. Rudolph, "How Good Must Single Photon Sources and Detectors Be for Efficient Linear Optical Quantum Computation?", Physical Review Letters **100**, 060502 (2008).

[65]H. Wang, Z.-C. Duan, Y.-H. Li, S. Chen, J.-P. Li, Y.-M. He, M.-C. Chen, Y. He, X. Ding, C.-Z. Peng, C. Schneider, M. Kamp, S. Höfling, C.-Y. Lu, and J.-W. Pan, "Near-Transform-Limited Single Photons from an Efficient Solid-State Quantum Emitter", Physical Review Letters **116**, 213601 (2016).

[66]F. Kaneda and P. G. Kwiat, "High-efficiency single-photon generation via large-scale active time multiplexing", arXiv, 1–12 (2018).

[67]H. Wang, Y. He, Y.-H. Li, Z.-E. Su, B. Li, H.-L. Huang, X. Ding, M.-C. Chen, C. Liu, J. Qin, J.-P. Li, Y.-M. He, C. Schneider, M. Kamp, C.-Z. Peng, S. Höfling, C.-Y. Lu, and J.-W. Pan, "High-efficiency multiphoton boson sampling", Nature Photonics **11**, 361–365 (2017).

[68]J. Cardenas, C. B. Poitras, J. T. Robinson, K. Preston, L. Chen, and M. Lipson, "Low loss etchless silicon photonic waveguides", Optics Express **17**, 4752 (2009).

[69]K. Wörhoff, R. G. Heideman, A. Leinse, and M. Hoekman, "TriPleX: a versatile dielectric photonic platform", Advanced Optical Technologies **4**, 189–207 (2015).

[70]G. S. Buller and R. J. Collins, "Single-photon generation and detection", Measurement Science and Technology **21**, 012002 (2010).

[71]J. Zhang, M. A. Itzler, H. Zbinden, and J.-W. Pan, "Advances in InGaAs/InP single-photon detector systems for quantum communication", Light: Science & Applications **4**, e286–e286 (2015).

[72]R. H. Hadfield, "Single-photon detectors for optical quantum information applications", Nature Photonics **3**, 696–705 (2009).

[73]A. E. Lita, A. J. Miller, and S. W. Nam, "Counting near-infrared single-photons with 95% efficiency", Optics Express **16**, 3032 (2008).

[74]F. Marsili, V. B. Verma, J. A. Stern, S. Harrington, A. E. Lita, T. Gerrits, I. Vayshenker, B. Baek, M. D. Shaw, R. P. Mirin, and S. W. Nam, "Detecting single infrared photons with 93% system efficiency", Nature Photonics **7**, 210–214 (2013).

[75]M. W. Doherty, N. B. Manson, P. Delaney, F. Jelezko, J. Wrachtrup, and L. C. Hollenberg, "The nitrogen-vacancy colour centre in diamond", Physics Reports **528**, 1–45 (2013).

[76]Y.-M. He, Y. He, Y.-J. Wei, D. Wu, M. Atatüre, C. Schneider, S. Höfling, M. Kamp, C.-Y. Lu, and J.-W. Pan, "On-demand semiconductor single-photon source with near-unity indistinguishability", Nature Nanotechnology **8**, 213–217 (2013).

[77]T. T. Tran, K. Bray, M. J. Ford, M. Toth, and I. Aharonovich, "Quantum emission from hexagonal boron nitride monolayers", Nature Nanotechnology **11**, 37–41 (2015).

[78]X. Ma, N. F. Hartmann, J. K. S. Baldwin, S. K. Doorn, and H. Htoon, "Room-temperature single-photon generation from solitary dopants of carbon nanotubes", Nature Nanotechnology **10**, 671–675 (2015).

[79]I. Aharonovich, D. Englund, and M. Toth, "Solid-state single-photon emitters", Nature Photonics **10**, 631–641 (2016).

[80]S. Unsleber, Y.-M. He, S. Gerhardt, S. Maier, C.-Y. Lu, J.-W. Pan, N. Gregersen, M. Kamp, C. Schneider, and S. Höfling, "Highly indistinguishable on-demand resonance fluorescence photons from a deterministic quantum dot micropillar device with 74% extraction efficiency", Optics Express **24**, 8539 (2016).

[81]I. Friedler, C. Sauvan, J. P. Hugonin, P. Lalanne, J. Claudon, and J. M. Gérard, "Solid-state single photon sources: the nanowire antenna", Optics Express **17**, 2095 (2009).

[82]N. Matsuda, "Deterministic reshaping of single-photon spectra using cross-phase modulation", Science Advances **2**, e1501223 (2016).

[83]R. B. Patel, A. J. Bennett, I. Farrer, C. A. Nicoll, D. A. Ritchie, and A. J. Shields, "Two-photon interference of the emission from electrically tunable remote quantum dots", Nature Photonics **4**, 632–635 (2010).

[84]A. Faraon, A. Majumdar, H. Kim, P. Petroff, and J. Vučković, "Fast Electrical Control of a Quantum Dot Strongly Coupled to a Photonic-Crystal Cavity", Physical Review Letters **104**, 047402 (2010).

[85]A. Faraon, D. Englund, I. Fushman, J. Vučković, N. Stoltz, and P. Petroff, "Local quantum dot tuning on photonic crystal chips", Applied Physics Letters **90**, 213110 (2007).

[86]F. Lenzini, B. Haylock, J. C. Loredo, R. A. Abrahão, N. A. Zakaria, S. Kasture, I. Sagnes, A. Lemaitre, H.-P. Phan, D. V. Dao, P. Senellart, M. P. Almeida, A. G. White, and M. Lobino, "Active demultiplexing of single photons from a solid-state source", Laser & Photonics Reviews **11**, 1600297 (2017).

[87]S. Tanzilli, H. De Riedmatten, W. Tittel, H. Zbinden, P. Baldi, M. De Micheli, D. Ostrowsky, and N. Gisin, "Highly efficient photon-pair source using periodically poled lithium niobate waveguide", Electronics Letters **37**, 26 (2001).

[88]H. Jin, F. M. Liu, P. Xu, J. L. Xia, M. L. Zhong, Y. Yuan, J. W. Zhou, Y. X. Gong, W. Wang, and S. N. Zhu, "On-Chip Generation and Manipulation of Entangled Photons Based on Reconfigurable Lithium-Niobate Waveguide Circuits", Physical Review Letters **113**, 103601 (2014).

[89]X.-L. Wang, L.-K. Chen, W. Li, H.-L. Huang, C. Liu, C. Chen, Y.-H. Luo, Z.-E. Su, D. Wu, Z.-D. Li, H. Lu, Y. Hu, X. Jiang, C.-Z. Peng, L. Li, N.-L. Liu, Y.-A. Chen, C.-Y. Lu, and J.-W. Pan, "Experimental Ten-Photon Entanglement", Physical Review Letters **117**, 210502 (2016).

[90]P. J. Mosley, J. S. Lundeen, B. J. Smith, P. Wasylczyk, A. B. U'Ren, C. Silberhorn, and I. A. Walmsley, "Heralded Generation of Ultrafast Single Photons in Pure Quantum States", Physical Review Letters **100**, 133601 (2008).

[91]J. W. Silverstone, D. Bonneau, K. Ohira, N. Suzuki, H. Yoshida, N. Iizuka, M. Ezaki, C. M. Natarajan, M. G. Tanner, R. H. Hadfield, V. Zwiller, G. D. Marshall, J. G. Rarity, J. L. O'Brien, and M. G. Thompson, "On-chip quantum interference between silicon photon-pair sources", Nature Photonics **8**, 104–108 (2014).

[92]J. He, B. A. Bell, A. Casas-Bedoya, Y. Zhang, A. S. Clark, C. Xiong, and B. J. Eggleton, "Ultracompact quantum splitter of degenerate photon pairs", Optica **2**, 779 (2015).

[93]C. A. Husko, A. S. Clark, M. J. Collins, A. De Rossi, S. Combrié, G. Lehoucq, I. H. Rey, T. F. Krauss, C. Xiong, and B. J. Eggleton, "Multi-photon absorption limits to heralded single photon sources", Scientific Reports **3**, 3087 (2013).

[94]H. Takesue and K. Inoue, "1.5 μm band quantum-correlated photon pair generation in dispersion-shifted fiber: suppression of noise photons by cooling fiber", Optics Express **13**, 7832 (2005).

[95]C. Xiong, C. Monat, A. S. Clark, C. Grillet, G. D. Marshall, M. J. Steel, J. Li, L. O'Faolain, T. F. Krauss, J. G. Rarity, and B. J. Eggleton, "Slow-light enhanced correlated photon pair generation in a silicon photonic crystal waveguide", Optics Letters **36**, 3413 (2011).

[96]J. He, C. Xiong, A. S. Clark, M. J. Collins, X. Gai, D.-Y. Choi, S. J. Madden, B. Luther-Davies, and B. J. Eggleton, "Effect of low-Raman window position on correlated photon-pair generation in a chalcogenide Ge 11.5 As 24 Se 64.5 nanowire", Journal of Applied Physics **112**, 123101 (2012).

[97]M. J. Collins, A. C. Judge, A. S. Clark, S. Shahnia, E. C. Mägi, M. J. Steel, C. Xiong, and B. J. Eggleton, "Broadband photon-counting Raman spectroscopy in short optical waveguides", Applied Physics Letters **101**, 211110 (2012).

[98]M. J. Collins, A. S. Clark, J. He, D.-Y. Choi, R. J. Williams, A. C. Judge, S. J. Madden, M. J. Withford, M. J. Steel, B. Luther-Davies, C. Xiong, and B. J. Eggleton, "Low Raman-noise correlated photon-pair generation in a dispersion-engineered chalcogenide As_2S_3 planar waveguide", Optics Letters **37**, 3393 (2012).

[99]X. Zhang, Y. Zhang, C. Xiong, and B. J. Eggleton, "Correlated photon pair generation in low-loss double-stripe silicon nitride waveguides", Journal of Optics **18**, 074016 (2016).

[100] A. S. Clark, C. Husko, M. J. Collins, G. Lehoucq, S. Xavier, A. De Rossi, S. Combrié, C. Xiong, and B. J. Eggleton, "Heralded single-photon source in a III–V photonic crystal", Optics Letters **38**, 649 (2013).

[101] C. Reimer, L. Caspani, M. Clerici, M. Ferrera, M. Kues, M. Peccianti, A. Pasquazi, L. Razzari, B. E. Little, S. T. Chu, D. J. Moss, and R. Morandotti, "Integrated frequency comb source of heralded single photons", Optics Express **22**, 6535 (2014).

[102] M. Kues, C. Reimer, P. Roztocki, L. R. Cortés, S. Sciara, B. Wetzel, Y. Zhang, A. Cino, S. T. Chu, B. E. Little, D. J. Moss, L. Caspani, J. Azaña, and R. Morandotti, "On-chip generation of high-dimensional entangled quantum states and their coherent control", Nature **546**, 622–626 (2017).

[103] D. J. Moss, R. Morandotti, A. L. Gaeta, and M. Lipson, "New CMOS-compatible platforms based on silicon nitride and Hydex for nonlinear optics", Nature Photonics **7**, 597–607 (2013).

[104] J. B. Spring, P. L. Mennea, B. J. Metcalf, P. C. Humphreys, J. C. Gates, H. L. Rogers, C. Söller, B. J. Smith, W. S. Kolthammer, P. G. R. Smith, and I. A. Walmsley, "Chip-based array of near-identical, pure, heralded single-photon sources", Optica **4**, 90 (2017).

[105] X.-s. Ma, S. Zotter, J. Kofler, T. Jennewein, and A. Zeilinger, "Experimental generation of single photons via active multiplexing", Physical Review A **83**, 043814 (2011).

[106] R. J. A. Francis-Jones, R. A. Hoggarth, and P. J. Mosley, "All-fiber multiplexed source of high-purity single photons", Optica **3**, 1270 (2016).

[107] J. Wang, S. Paesani, Y. Ding, R. Santagati, P. Skrzypczyk, A. Salavrakos, J. Tura, R. Augusiak, L. Mančinska, D. Bacco, D. Bonneau, J. W. Silverstone, Q. Gong, A. Acín, K. Rottwitt, L. K. Oxenløwe, J. L. O'Brien, A. Laing, and M. G. Thompson, "Multidimensional quantum entanglement with large-scale integrated optics", Science **360**, 285–291 (2018).

[108] A. Christ and C. Silberhorn, "Limits on the deterministic creation of pure single-photon states using parametric down-conversion", Physical Review A **85**, 023829 (2012).

[109] A. L. Migdall, D. Branning, and S. Castelletto, "Tailoring single-photon and multiphoton probabilities of a single-photon on-demand source", Physical Review A **66**, 053805 (2002).

[110] J. Mower and D. Englund, "Efficient generation of single and entangled photons on a silicon photonic integrated chip", Physical Review A **84**, 052326 (2011).

[111] M. Gimeno-Segovia, H. Cable, G. J. Mendoza, P. Shadbolt, J. W. Silverstone, J. Carolan, M. G. Thompson, J. L. O'Brien, and T. Rudolph, "Relative multiplexing for minimising switching in linear-optical quantum computing", New Journal of Physics **19**, 063013 (2017).

[112] W. Diffie and M. E. Hellman, "Multiuser cryptographic techniques", in Proceedings of the june 7-10, 1976, national computer conference and exposition on - afips '76 (1976), p. 109.

[113]R. L. Rivest, A. Shamir, and L. Adleman, "A method for obtaining digital signatures and public-key cryptosystems", Communications of the ACM **21**, 120–126 (1978).

[114]W. Diffie and M. Hellman, "New directions in cryptography", IEEE Transactions on Information Theory **22**, 644–654 (1976).

[115]N. Gisin, G. Ribordy, W. Tittel, and H. Zbinden, "Quantum cryptography", Reviews of Modern Physics **74**, 145–195 (2002).

[116]P. Shor, "Algorithms for quantum computation: discrete logarithms and factoring", in Proceedings 35th annual symposium on foundations of computer science (1994), pp. 124–134.

[117]C. H. Bennett and G. Brassard, "Quantum cryptography: Public key distribution and coin tossing", Theoretical Computer Science **560**, 7–11 (2014).

[118]A. K. Ekert, "Quantum cryptography based on Bell's theorem", Physical Review Letters **67**, 661–663 (1991).

[119]P. W. Shor and J. Preskill, "Simple Proof of Security of the BB84 Quantum Key Distribution Protocol", Physical Review Letters **85**, 441–444 (2000).

[120]H. Lo, "Unconditional Security of Quantum Key Distribution over Arbitrarily Long Distances", Science **283**, 2050–2056 (1999).

[121]V. Scarani, H. Bechmann-Pasquinucci, N. J. Cerf, M. Dušek, N. Lütkenhaus, and M. Peev, "The security of practical quantum key distribution", Reviews of Modern Physics **81**, 1301–1350 (2009).

[122]J. Carter and M. N. Wegman, "Universal classes of hash functions", Journal of Computer and System Sciences **18**, 143–154 (1979).

[123]M. N. Wegman and J. Carter, "New hash functions and their use in authentication and set equality", Journal of Computer and System Sciences **22**, 265–279 (1981).

[124]C. H. Bennett and G. Brassard, "Quantum cryptography: Public key distribution and coin tossing", IEEE International Conference on Computers, Systems & Signal Processing, 175–179 (1984).

[125]H.-K. Lo, M. Curty, and K. Tamaki, "Secure quantum key distribution", Nature Photonics **8**, 595–604 (2014).

[126]C. H. Bennett, G. Brassard, and N. D. Mermin, "Quantum cryptography without Bell's theorem", Physical Review Letters **68**, 557–559 (1992).

[127]H.-K. Lo, H. Chau, and M. Ardehali, "Efficient Quantum Key Distribution Scheme and a Proof of Its Unconditional Security", Journal of Cryptology **18**, 133–165 (2005).

[128]C. Gobby, Z. L. Yuan, and A. J. Shields, "Quantum key distribution over 122 km of standard telecom fiber", Applied Physics Letters **84**, 3762–3764 (2004).

[129]D. Rosenberg, J. W. Harrington, P. R. Rice, P. A. Hiskett, C. G. Peterson, R. J. Hughes, A. E. Lita, S. W. Nam, and J. E. Nordholt, "Long-Distance Decoy-State Quantum Key Distribution in Optical Fiber", Physical Review Letters **98**, 010503 (2007).

[130]H.-L. Yin, T.-Y. Chen, Z.-W. Yu, H. Liu, L.-X. You, Y.-H. Zhou, S.-J. Chen, Y. Mao, M.-Q. Huang, W.-J. Zhang, H. Chen, M. J. Li, D. Nolan, F. Zhou, X. Jiang, Z. Wang, Q. Zhang, X.-B. Wang, and J.-W. Pan, "Measurement-Device-Independent Quantum Key Distribution Over a 404 km Optical Fiber", Physical Review Letters **117**, 190501 (2016).

[131]D. Stucki, N. Gisin, O. Guinnard, G. Ribordy, and H. Zbinden, "Quantum key distribution over 67 km with a plug&play system", New Journal of Physics **4**, 341 (2002).

[132]B. Korzh, C. C. W. Lim, R. Houlmann, N. Gisin, M. J. Li, D. Nolan, B. Sanguinetti, R. Thew, and H. Zbinden, "Provably secure and practical quantum key distribution over 307 km of optical fibre", Nature Photonics **9**, 163–168 (2015).

[133]T. Schmitt-Manderbach, H. Weier, M. Fürst, R. Ursin, F. Tiefenbacher, T. Scheidl, J. Perdigues, Z. Sodnik, C. Kurtsiefer, J. G. Rarity, A. Zeilinger, and H. Weinfurter, "Experimental Demonstration of Free-Space Decoy-State Quantum Key Distribution over 144 km", Physical Review Letters **98**, 010504 (2007).

[134]W. T. Buttler, R. J. Hughes, P. G. Kwiat, S. K. Lamoreaux, G. G. Luther, G. L. Morgan, J. E. Nordholt, C. G. Peterson, and C. M. Simmons, "Practical Free-Space Quantum Key Distribution over 1 km", Physical Review Letters **81**, 3283–3286 (1998).

[135]R. J. Hughes, W. T. Buttler, P. G. Kwiat, S. K. Lamoreaux, G. L. Morgan, J. E. Nordholt, and C. G. Peterson, "Free-space quantum key distribution in daylight", Journal of Modern Optics **47**, 549–562 (2000).

[136]S.-K. Liao, W.-Q. Cai, W.-Y. Liu, L. Zhang, Y. Li, J.-G. Ren, J. Yin, Q. Shen, Y. Cao, Z.-P. Li, F.-Z. Li, X.-W. Chen, L.-H. Sun, J.-J. Jia, J.-C. Wu, X.-J. Jiang, J.-F. Wang, Y.-M. Huang, Q. Wang, Y.-L. Zhou, L. Deng, T. Xi, L. Ma, T. Hu, Q. Zhang, Y.-A. Chen, N.-L. Liu, X.-B. Wang, Z.-C. Zhu, C.-Y. Lu, R. Shu, C.-Z. Peng, J.-Y. Wang, and J.-W. Pan, "Satellite-to-ground quantum key distribution", Nature **549**, 43–47 (2017).

[137]C. Kurtsiefer, P. Zarda, M. Halder, H. Weinfurter, P. M. Gorman, P. R. Tapster, and J. G. Rarity, "A step towards global key distribution", Nature **419**, 450–450 (2002).

[138]S. Nauerth, F. Moll, M. Rau, C. Fuchs, J. Horwath, S. Frick, and H. Weinfurter, "Air-to-ground quantum communication", Nature Photonics **7**, 382–386 (2013).

[139]L. Salvail, M. Peev, E. Diamanti, R. Alléaume, N. Lütkenhaus, and T. Länger, "Security of trusted repeater quantum key distribution networks", Journal of Computer Security **18**, edited by J. Camenisch, J. Lopez, F. Massacci, M. Ciscato, and T. Skordas, 61–87 (2010).

[140]K. Mattle, H. Weinfurter, P. G. Kwiat, and A. Zeilinger, "Dense Coding in Experimental Quantum Communication", Physical Review Letters **76**, 4656–4659 (1996).

[141]I. Marcikic, H. de Riedmatten, W. Tittel, H. Zbinden, and N. Gisin, "Long-distance teleportation of qubits at telecommunication wavelengths", Nature **421**, 509–513 (2003).

[142]J.-W. Pan, C. Simon, Č. Brukner, and A. Zeilinger, "Entanglement purification for quantum communication", Nature **410**, 1067–1070 (2001).

[143]U. Vazirani and T. Vidick, "Fully Device-Independent Quantum Key Distribution", Physical Review Letters **113**, 140501 (2014).

[144]G. Brassard, "Brief history of quantum cryptography: a personal perspective", in IEEE information theory workshop on theory and practice in information-theoretic security, 2005. Vol. 2005 (2006), pp. 19–23.

[145]J. Yin, Y. Cao, Y.-H. Li, S.-K. Liao, L. Zhang, J.-G. Ren, W.-Q. Cai, W.-Y. Liu, B. Li, H. Dai, G.-B. Li, Q.-M. Lu, Y.-H. Gong, Y. Xu, S.-L. Li, F.-Z. Li, Y.-Y. Yin, Z.-Q. Jiang, M. Li, J.-J. Jia, G. Ren, D. He, Y.-L. Zhou, X.-X. Zhang, N. Wang, X. Chang, Z.-C. Zhu, N.-L. Liu, Y.-A. Chen, C.-Y. Lu, R. Shu, C.-Z. Peng, J.-Y. Wang, and J.-W. Pan, "Satellite-based entanglement distribution over 1200 kilometers", Science **356**, 1140–1144 (2017).

[146]J.-G. Ren, P. Xu, H.-L. Yong, L. Zhang, S.-K. Liao, J. Yin, W.-Y. Liu, W.-Q. Cai, M. Yang, L. Li, K.-X. Yang, X. Han, Y.-Q. Yao, J. Li, H.-Y. Wu, S. Wan, L. Liu, D.-Q. Liu, Y.-W. Kuang, Z.-P. He, P. Shang, C. Guo, R.-H. Zheng, K. Tian, Z.-C. Zhu, N.-L. Liu, C.-Y. Lu, R. Shu, Y.-A. Chen, C.-Z. Peng, J.-Y. Wang, and J.-W. Pan, "Ground-to-satellite quantum teleportation", Nature **549**, 70–73 (2017).

[147]G. Ribordy, J. Brendel, J.-D. Gautier, N. Gisin, and H. Zbinden, "Long-distance entanglement-based quantum key distribution", Physical Review A **63**, 012309 (2000).

[148]T. Honjo, S. W. Nam, H. Takesue, Q. Zhang, H. Kamada, Y. Nishida, O. Tadanaga, M. Asobe, B. Baek, R. Hadfield, S. Miki, M. Fujiwara, M. Sasaki, Z. Wang, K. Inoue, and Y. Yamamoto, "Long-distance entanglement-based quantum key distribution over optical fiber", Optics Express **16**, 19118 (2008).

[149]K. Kao and G. Hockham, "Dielectric-fibre surface waveguides for optical frequencies", Proceedings of the Institution of Electrical Engineers **113**, 1151–1158 (1966).

[150]S.-K. Liao, H.-L. Yong, C. Liu, G.-L. Shentu, D.-D. Li, J. Lin, H. Dai, S.-Q. Zhao, B. Li, J.-Y. Guan, W. Chen, Y.-H. Gong, Y. Li, Z.-H. Lin, G.-S. Pan, J. S. Pelc, M. M. Fejer, W.-Z. Zhang, W.-Y. Liu, J. Yin, J.-G. Ren, X.-B. Wang, Q. Zhang, C.-Z. Peng, and J.-W. Pan, "Long-distance free-space quantum key distribution in daylight towards inter-satellite communication", Nature Photonics **11**, 509–513 (2017).

[151]S. Jose, "Understanding the performance of free-space optics", J. Opt. Netw. **2**, 178–200 (2003).

[152]F. Steinlechner, S. Ecker, M. Fink, B. Liu, J. Bavaresco, M. Huber, T. Scheidl, and R. Ursin, "Distribution of high-dimensional entanglement via an intra-city free-space link", Nature Communications **8**, 15971 (2017).

[153]R. Valivarthi, M. G. Puigibert, Q. Zhou, G. H. Aguilar, V. B. Verma, F. Marsili, M. D. Shaw, S. W. Nam, D. Oblak, and W. Tittel, "Quantum teleportation across a metropolitan fibre network", Nature Photonics **10**, 676–680 (2016).

[154]Q.-C. Sun, Y.-L. Mao, S.-J. Chen, W. Zhang, Y.-F. Jiang, Y.-B. Zhang, W.-J. Zhang, S. Miki, T. Yamashita, H. Terai, X. Jiang, T.-Y. Chen, L.-X. You, X.-F. Chen, Z. Wang, J.-Y. Fan, Q. Zhang, and J.-W. Pan, "Quantum teleportation with independent sources and prior entanglement distribution over a network", Nature Photonics **10**, 671–675 (2016).

[155]N. C. Harris, G. R. Steinbrecher, M. Prabhu, Y. Lahini, J. Mower, D. Bunandar, C. Chen, F. N. C. Wong, T. Baehr-Jones, M. Hochberg, S. Lloyd, and D. Englund, "Quantum transport simulations in a programmable nanophotonic processor", Nature Photonics **11**, 447–452 (2017).

[156]J. W. Silverstone, D. Bonneau, J. L. O'Brien, and M. G. Thompson, "Silicon Quantum Photonics", IEEE Journal of Selected Topics in Quantum Electronics **22**, edited by G. T. Reed, 390–402 (2016).

[157]Y. Wang, M. Um, J. Zhang, S. An, M. Lyu, J.-N. Zhang, L.-M. Duan, D. Yum, and K. Kim, "Single-qubit quantum memory exceeding ten-minute coherence time", Nature Photonics **11**, 646–650 (2017).

[158]R. Santagati, J. Wang, A. A. Gentile, S. Paesani, N. Wiebe, J. R. McClean, S. Morley-Short, P. J. Shadbolt, D. Bonneau, J. W. Silverstone, D. P. Tew, X. Zhou, J. L. O'Brien, and M. G. Thompson, "Witnessing eigenstates for quantum simulation of Hamiltonian spectra", Science Advances **4**, eaap9646 (2018).

[159]C. Xiong, B. Bell, and B. J. Eggleton, "CMOS-compatible photonic devices for single-photon generation", Nanophotonics **5**, 427–439 (2016).

[160]L. Caspani, C. Xiong, B. J. Eggleton, D. Bajoni, M. Liscidini, M. Galli, R. Morandotti, and D. J. Moss, "Integrated sources of photon quantum states based on nonlinear optics", Light: Science & Applications **6**, e17100 (2017).

[161]A. Politi, M. J. Cryan, J. G. Rarity, S. Yu, and J. L. O'Brien, "Silica-on-Silicon Waveguide Quantum Circuits", Science **320**, 646–649 (2008).

[162]J. C. F. Matthews, A. Politi, A. Stefanov, and J. L. O'Brien, "Manipulation of multiphoton entanglement in waveguide quantum circuits", Nature Photonics **3**, 346–350 (2009).

[163]G. D. Marshall, A. Politi, J. C. F. Matthews, P. Dekker, M. Ams, M. J. Withford, and J. L. O'Brien, "Laser written waveguide photonic quantum circuits", Optics Express **17**, 12546 (2009).

[164]A. Politi, J. C. F. Matthews, and J. L. O'Brien, "Shor's Quantum Factoring Algorithm on a Photonic Chip", Science **325**, 1221–1221 (2009).

[165]M. Lobino and J. L. O'Brien, "Quantum photonics: Entangled photons on a chip", Nature **469**, 43–44 (2011).

[166]P. J. Shadbolt, M. R. Verde, A. Peruzzo, A. Politi, A. Laing, M. Lobino, J. C. F. Matthews, M. G. Thompson, and J. L. O'Brien, "Generating, manipulating and measuring entanglement and mixture with a reconfigurable photonic circuit", Nature Photonics **6**, 45–49 (2012).

[167] A. Peruzzo, P. Shadbolt, N. Brunner, S. Popescu, and J. L. O'Brien, "A Quantum Delayed-Choice Experiment", Science **338**, 634–637 (2012).

[168] K.-I. Harada, H. Takesue, H. Fukuda, T. Tsuchizawa, T. Watanabe, K. Yamada, Y. Tokura, and S.-I. Itabashi, "Frequency and Polarization Characteristics of Correlated Photon-Pair Generation Using a Silicon Wire Waveguide", IEEE Journal of Selected Topics in Quantum Electronics **16**, 325–331 (2010).

[169] E. Engin, D. Bonneau, C. M. Natarajan, A. S. Clark, M. G. Tanner, R. H. Hadfield, S. N. Dorenbos, V. Zwiller, K. Ohira, N. Suzuki, H. Yoshida, N. Iizuka, M. Ezaki, J. L. O'Brien, and M. G. Thompson, "Photon pair generation in a silicon micro-ring resonator with reverse bias enhancement", Optics Express **21**, 27826 (2013).

[170] W. C. Jiang, X. Lu, J. Zhang, O. Painter, and Q. Lin, "Silicon-chip source of bright photon pairs", Optics Express **23**, 20884 (2015).

[171] C. Xiong, C. Monat, A. S. Clark, C. Grillet, G. D. Marshall, M. J. Steel, J. Li, L. O'Faolain, T. F. Krauss, J. G. Rarity, and B. J. Eggleton, "Slow-light Enhanced Correlated Photon-Pair Generation in Silicon", Optics Letters **36**, 3413–3415 (2011).

[172] Chunle Xiong, M. J. Collins, M. J. Steel, T. F. Krauss, B. J. Eggleton, and A. S. Clark, "Photonic Crystal Waveguide Sources of Photons for Quantum Communication Applications", IEEE Journal of Selected Topics in Quantum Electronics **21**, 205–214 (2015).

[173] M. Davanço, J. R. Ong, A. B. Shehata, A. Tosi, I. Agha, S. Assefa, F. Xia, W. M. J. Green, S. Mookherjea, and K. Srinivasan, "Telecommunications-band heralded single photons from a silicon nanophotonic chip", Applied Physics Letters **100**, 261104 (2012).

[174] N. Matsuda, H. Takesue, K. Shimizu, Y. Tokura, E. Kuramochi, and M. Notomi, "Slow light enhanced correlated photon pair generation in photonic-crystal coupled-resonator optical waveguides", Optics Express **21**, 8596 (2013).

[175] X. Zhang, I. Jizan, J. He, A. S. Clark, D.-Y. Choi, C. J. Chae, B. J. Eggleton, and C. Xiong, "Enhancing the heralded single-photon rate from a silicon nanowire by time and wavelength division multiplexing pump pulses", Optics Letters **40**, 2489 (2015).

[176] J. E. Sharping, K. F. Lee, M. A. Foster, A. C. Turner, B. S. Schmidt, M. Lipson, A. L. Gaeta, and P. Kumar, "Generation of correlated photons in nanoscale silicon waveguides", Optics Express **14**, 12388 (2006).

[177] E. Engin, D. Bonneau, C. M. Natarajan, A. S. Clark, M. G. Tanner, R. H. Hadfield, S. N. Dorenbos, V. Zwiller, K. Ohira, N. Suzuki, H. Yoshida, N. Iizuka, M. Ezaki, J. L. O'Brien, and M. G. Thompson, "Photon pair generation in a silicon micro-ring resonator with reverse bias enhancement", Optics Express **21**, 27826 (2013).

[178] X. Wang, W. Shi, H. Yun, S. Grist, N. A. F. Jaeger, and L. Chrostowski, "Narrow-band waveguide Bragg gratings on SOI wafers with CMOS-compatible fabrication process", Optics Express **20**, 15547 (2012).

[179]E. Brainis, "Four-photon scattering in birefringent fibers", Physical Review A **79**, 023840 (2009).

[180]N. Matsuda, H. Le Jeannic, H. Fukuda, T. Tsuchizawa, W. J. Munro, K. Shimizu, K. Yamada, Y. Tokura, and H. Takesue, "A monolithically integrated polarization entangled photon pair source on a silicon chip", Scientific Reports **2**, 817 (2012).

[181]S. Ramelow, A. Farsi, S. Clemmen, D. Orquiza, K. Luke, M. Lipson, and A. L. Gaeta, "Silicon-Nitride Platform for Narrowband Entangled Photon Generation", arXiv, 1508.04358 (2015).

[182]K. Ikeda, R. E. Saperstein, N. Alic, and Y. Fainman, "Thermal and Kerr nonlinear properties of plasma-deposited silicon nitride/ silicon dioxide waveguides", Optics Express **16**, 12987 (2008).

[183]J. P. Epping, M. Hoekman, R. Mateman, A. Leinse, R. G. Heideman, A. van Rees, P. J. van der Slot, C. J. Lee, and K.-J. Boller, "High confinement, high yield Si3N4 waveguides for nonlinear optical applications", Optics Express **23**, 642 (2015).

[184]F. Morichetti, A. Melloni, M. Martinelli, R. G. Heideman, A. Leinse, D. H. Geuzebroek, and A. Borreman, "Box-Shaped Dielectric Waveguides: A New Concept in Integrated Optics?", Journal of Lightwave Technology **25**, 2579–2589 (2007).

[185]C. G. H. Roeloffzen, L. Zhuang, C. Taddei, A. Leinse, R. G. Heideman, P. W. L. van Dijk, R. M. Oldenbeuving, D. A. I. Marpaung, M. Burla, and K. .-.-J. Boller, "Silicon nitride microwave photonic circuits", Optics Express **21**, 22937 (2013).

[186]M.-C. Tien, J. F. Bauters, M. J. R. Heck, D. J. Blumenthal, and J. E. Bowers, "Ultra-low loss Si_3N_4 waveguides with low nonlinearity and high power handling capability", Optics Express **18**, 23562 (2010).

[187]C. J. Krückel, V. Torres-Company, P. A. Andrekson, D. T. Spencer, J. F. Bauters, M. J. R. Heck, and J. E. Bowers, "Continuous wave-pumped wavelength conversion in low-loss silicon nitride waveguides", Optics Letters **40**, 875 (2015).

[188]A. Fülöp, C. J. Krückel, D. Castelló-Lurbe, E. Silvestre, and V. Torres-Company, "Triply resonant coherent four-wave mixing in silicon nitride microresonators", Optics Letters **40**, 4006 (2015).

[189]C. G. H. Roeloffzen, M. Hoekman, E. J. Klein, L. S. Wevers, R. B. Timens, D. Marchenko, D. Geskus, R. Dekker, A. Alippi, R. Grootjans, A. van Rees, R. M. Oldenbeuving, J. P. Epping, R. G. Heideman, K. Worhoff, A. Leinse, D. Geuzebroek, E. Schreuder, P. W. L. van Dijk, I. Visscher, C. Taddei, Y. Fan, C. Taballione, Y. Liu, D. Marpaung, L. Zhuang, M. Benelajla, and K.-J. Boller, "Low-Loss Si3N4 TriPleX Optical Waveguides: Technology and Applications Overview", IEEE Journal of Selected Topics in Quantum Electronics **24**, 1–21 (2018).

[190]A. Dhakal, A. Z. Subramanian, P. Wuytens, F. Peyskens, N. L. Thomas, and R. Baets, "Evanescent excitation and collection of spontaneous Raman spectra using silicon nitride nanophotonic waveguides", Optics Letters **39**, 4025 (2014).

[191] A. S. Clark, M. J. Collins, A. C. Judge, E. C. Mägi, C. Xiong, and B. J. Eggleton, "Raman scattering effects on correlated photon-pair generation in chalcogenide", Optics Express **20**, 16807 (2012).

[192] C. Xiong, L. G. Helt, A. C. Judge, G. D. Marshall, M. J. Steel, J. E. Sipe, and B. J. Eggleton, "Quantum-correlated photon pair generation in chalcogenide As_2S_3 waveguides", Optics Express **18**, 16206 (2010).

[193] Q. Lin, F. Yaman, and G. P. Agrawal, "Photon-pair generation in optical fibers through four-wave mixing: Role of Raman scattering and pump polarization", Physical Review A **75**, 023803 (2007).

[194] Q. Lin, F. Yaman, and G. P. Agrawal, "Photon-pair generation by four-wave mixing in optical fibers", Optics Letters **31**, 1286 (2006).

[195] D. Bonneau, G. J. Mendoza, J. L. O'Brien, and M. G. Thompson, "Effect of loss on multiplexed single-photon sources", New Journal of Physics **17**, 043057 (2015).

[196] M. Grimau Puigibert, G. H. Aguilar, Q. Zhou, F. Marsili, M. D. Shaw, V. B. Verma, S. W. Nam, D. Oblak, and W. Tittel, "Heralded Single Photons Based on Spectral Multiplexing and Feed-Forward Control", Physical Review Letters **119**, 083601 (2017).

[197] F. Kaneda, B. G. Christensen, J. J. Wong, H. S. Park, K. T. McCusker, and P. G. Kwiat, "Time-multiplexed heralded single-photon source", Optica **2**, 1010 (2015).

[198] G. J. Mendoza, R. Santagati, J. Munns, E. Hemsley, M. Piekarek, E. Martín-López, G. D. Marshall, D. Bonneau, M. G. Thompson, and J. L. O'Brien, "Active temporal and spatial multiplexing of photons", Optica **3**, 127 (2016).

[199] C. Xiong, X. Zhang, Z. Liu, M. J. Collins, A. Mahendra, L. G. Helt, M. J. Steel, D. Y. Choi, C. J. Chae, P. H. W. Leong, and B. J. Eggleton, "Active temporal multiplexing of indistinguishable heralded single photons", Nature Communications **7**, 10853 (2016).

[200] R. A. Hoggarth, R. J. A. Francis-Jones, and P. J. Mosley, "Resource-efficient fibre-integrated temporal multiplexing of heralded single photons", Journal of Optics **19**, 125503 (2017).

[201] X. Zhang, Y. H. Lee, B. A. Bell, P. H. W. Leong, T. Rudolph, B. J. Eggleton, and C. Xiong, "Indistinguishable heralded single photon generation via relative temporal multiplexing of two sources", Optics Express **25**, 26067 (2017).

[202] C. K. Hong, Z. Y. Ou, and L. Mandel, "Measurement of subpicosecond time intervals between two photons by interference", Physical Review Letters **59**, 2044–2046 (1987).

[203] P. Ben Dixon, J. H. Shapiro, and F. N. C. Wong, "Spectral engineering by Gaussian phase-matching for quantum photonics", Optics Express **21**, 5879 (2013).

[204] K.-i. Harada, H. Takesue, H. Fukuda, T. Tsuchizawa, T. Watanabe, K. Yamada, Y. Tokura, and S.-i. Itabashi, "Indistinguishable photon pair generation using two independent silicon wire waveguides", New Journal of Physics **13**, 065005 (2011).

[205]E. Jeffrey, N. A. Peters, and P. G. Kwiat, "Towards a periodic deterministic source of arbitrary single-photon states", New Journal of Physics **6**, 100–100 (2004).

[206]N. Hosseini, R. Dekker, M. Hoekman, M. Dekkers, J. Bos, A. Leinse, and R. Heideman, "Stress-optic modulator in TriPleX platform using a piezoelectric lead zirconate titanate (PZT) thin film", Optics Express **23**, 14018 (2015).

[207]L. G. Helt, Z. Yang, M. Liscidini, and J. E. Sipe, "Spontaneous four-wave mixing in microring resonators", Optics Letters **35**, 3006 (2010).

[208]E. Pomarico, B. Sanguinetti, C. I. Osorio, H. Herrmann, and R. T. Thew, "Engineering integrated pure narrow-band photon sources", New Journal of Physics **14**, 033008 (2012).

[209]I. Esmaeil Zadeh, J. W. N. Los, R. B. M. Gourgues, V. Steinmetz, G. Bulgarini, S. M. Dobrovolskiy, V. Zwiller, and S. N. Dorenbos, "Single-photon detectors combining high efficiency, high detection rates, and ultra-high timing resolution", APL Photonics **2**, 111301 (2017).

[210]J. Zhang, R. Thew, J.-d. Gautier, N. Gisin, and H. Zbinden, "Comprehensive Characterization of InGaAs–InP Avalanche Photodiodes at 1550 nm With an Active Quenching ASIC", IEEE Journal of Quantum Electronics **45**, 792–799 (2009).

[211]K. Makino, Y. Hashimoto, J.-i. Yoshikawa, H. Ohdan, T. Toyama, P. van Loock, and A. Furusawa, "Synchronization of optical photons for quantum information processing", Science Advances **2**, e1501772 (2016).

[212]F. Kaneda, F. Xu, J. Chapman, and P. G. Kwiat, "Quantum-memory-assisted multi-photon generation for efficient quantum information processing", Optica **4**, 1034 (2017).

[213]D. Felinto, C. W. Chou, J. Laurat, E. W. Schomburg, H. de Riedmatten, and H. J. Kimble, "Conditional control of the quantum states of remote atomic memories for quantum networking", Nature Physics **2**, 844–848 (2006).

[214]J. Nunn, N. K. Langford, W. S. Kolthammer, T. F. M. Champion, M. R. Sprague, P. S. Michelberger, X.-M. Jin, D. G. England, and I. A. Walmsley, "Enhancing Multiphoton Rates with Quantum Memories", Physical Review Letters **110**, 133601 (2013).

[215]M. Gimeno-Segovia, H. Cable, G. J. Mendoza, P. Shadbolt, J. W. Silverstone, J. Carolan, M. G. Thompson, J. L. O'Brien, and T. Rudolph, "Relative multiplexing for minimising switching in linear-optical quantum computing", New Journal of Physics **19**, 1–13 (2017).

[216]F. Lenzini, B. Haylock, J. C. Loredo, R. A. Abrahão, N. A. Zakaria, S. Kasture, I. Sagnes, A. Lemaitre, H.-P. Phan, D. V. Dao, P. Senellart, M. P. Almeida, A. G. White, and M. Lobino, "Active demultiplexing of single photons from a solid-state source", Laser & Photonics Reviews **11**, 1600297 (2017).

[217]X. Zhang, R. Jiang, B. Bell, D.-Y. Choi, C. Chae, and C. Xiong, "Interfering Heralded Single Photons from Two Separate Silicon Nanowires Pumped at Different Wavelengths", Technologies **4**, 25 (2016).

[218]M. Heuck, M. Pant, and D. R. Englund, "Temporally and spectrally multiplexed single photon source using quantum feedback control for scalable photonic quantum technologies", New Journal of Physics **20**, 063046 (2018).

[219]F. Ladouceur and L. Poladian, "Surface roughness and backscattering", Optics Letters **21**, 1833 (1996).

[220]F. Morichetti, A. Canciamilla, M. Martinelli, A. Samarelli, R. M. De La Rue, M. Sorel, and A. Melloni, "Coherent backscattering in optical microring resonators", Applied Physics Letters **96**, 081112 (2010).

[221]C. Huang, J. Fan, and L. Zhu, "Dynamic nonlinear thermal optical effects in coupled ring resonators", AIP Advances **2**, 032131 (2012).

[222]R. Claps, D. Dimitropoulos, V. Raghunathan, Y. Han, and B. Jalali, "Observation of stimulated Raman amplification in silicon waveguides", Optics Express **11**, 1731 (2003).

[223]C. M. Natarajan, M. G. Tanner, and R. H. Hadfield, "Superconducting nanowire single-photon detectors: physics and applications", Superconductor Science and Technology **25**, 063001 (2012).

[224]M. D. Eisaman, J. Fan, A. Migdall, and S. V. Polyakov, "Invited Review Article: Single-photon sources and detectors", Review of Scientific Instruments **82**, 071101 (2011).

[225]I. Esmaeil Zadeh, J. W. N. Los, R. B. M. Gourgues, V. Steinmetz, G. Bulgarini, S. M. Dobrovolskiy, V. Zwiller, and S. N. Dorenbos, "Single-photon detectors combining high efficiency, high detection rates, and ultra-high timing resolution", APL Photonics **2**, 111301 (2017).

[226]O. J. Morris, R. J. Francis-Jones, K. G. Wilcox, A. C. Tropper, and P. J. Mosley, "Photon-pair generation in photonic crystal fibre with a 1.5GHz modelocked VECSEL", Optics Communications **327**, 39–44 (2014).

[227]I. Marcikic, H. de Riedmatten, W. Tittel, V. Scarani, H. Zbinden, and N. Gisin, "Time-bin entangled qubits for quantum communication created by femtosecond pulses", Physical Review A **66**, 062308 (2002).

[228]J. W. Silverstone, R. Santagati, D. Bonneau, M. J. Strain, M. Sorel, J. L. O'Brien, and M. G. Thompson, "Qubit entanglement between ring-resonator photon-pair sources on a silicon chip", Nature Communications **6**, 7948 (2015).

[229]H. Takesue, Y. Tokura, H. Fukuda, T. Tsuchizawa, T. Watanabe, K. Yamada, and S.-i. Itabashi, "Entanglement generation using silicon wire waveguide", Applied Physics Letters **91**, 201108 (2007).

[230]I. Marcikic, H. de Riedmatten, W. Tittel, H. Zbinden, M. Legré, and N. Gisin, "Distribution of Time-Bin Entangled Qubits over 50 km of Optical Fiber", Physical Review Letters **93**, 180502 (2004).

[231]K.-i. Harada, H. Takesue, H. Fukuda, T. Tsuchizawa, T. Watanabe, K. Yamada, Y. Tokura, and S.-i. Itabashi, "Generation of high-purity entangled photon pairs using silicon wire waveguide", Optics Express **16**, 20368 (2008).

[232]R. Wakabayashi, M. Fujiwara, K.-i. Yoshino, Y. Nambu, M. Sasaki, and T. Aoki, "Time-bin entangled photon pair generation from Si micro-ring resonator", Optics Express **23**, 1103 (2015).

[233]P. G. Kwiat, A. M. Steinberg, and R. Y. Chiao, "High-visibility interference in a Bell-inequality experiment for energy and time", Physical Review A **47**, R2472–R2475 (1993).

[234]J. Zhang, R. Thew, J.-d. Gautier, N. Gisin, and H. Zbinden, "Comprehensive Characterization of InGaAs-InP Avalanche Photodiodes at 1550 nm With an Active Quenching ASIC", IEEE Journal of Quantum Electronics **45**, 792–799 (2009).

[235]L. Zhuang, D. Marpaung, M. Burla, W. Beeker, A. Leinse, and C. Roeloffzen, "Low-loss, high-index-contrast Si3N4/SiO2 optical waveguides for optical delay lines in microwave photonics signal processing", Optics Express **19**, 23162 (2011).

[236]A. W. Elshaari, I. E. Zadeh, A. Fognini, M. E. Reimer, D. Dalacu, P. J. Poole, V. Zwiller, and K. D. Jöns, "On-chip single photon filtering and multiplexing in hybrid quantum photonic circuits", Nature Communications **8**, 379 (2017).

[237]X. Zhang, B. Bell, M. Pelusi, J. He, W. Geng, Y. Kong, P. Zhang, C. Xiong, and B. J. Eggleton, "High repetition rate correlated photon pair generation in integrated silicon nanowires", Applied Optics **56**, 8420 (2017).

[238]P.-I. Dietrich, M. Blaicher, I. Reuter, M. Billah, T. Hoose, A. Hofmann, C. Caer, R. Dangel, B. Offrein, U. Troppenz, M. Moehrle, W. Freude, and C. Koos, "In situ 3D nanoprinting of free-form coupling elements for hybrid photonic integration", Nature Photonics **12**, 241–247 (2018).

[239]H. de Riedmatten, I. Marcikic, J. A. W. van Houwelingen, W. Tittel, H. Zbinden, and N. Gisin, "Long-distance entanglement swapping with photons from separated sources", Physical Review A **71**, 050302 (2005).

[240]A. Mahendra, C. Xiong, X. Zhang, B. J. Eggleton, and P. H. W. Leong, "Multiwavelength stabilization control of a thermo-optic system with adaptive reconfiguration", Applied Optics **56**, 1113 (2017).

[241]C. Schuck, W. H. P. Pernice, and H. X. Tang, "NbTiN superconducting nanowire detectors for visible and telecom wavelengths single photon counting on Si3N4 photonic circuits", Applied Physics Letters **102**, 051101 (2013).

[242]Y.-B. Sheng and L. Zhou, "Distributed secure quantum machine learning", Science Bulletin **62**, 1025–1029 (2017).

[243]J.-W. Pan, Z.-B. Chen, C.-Y. Lu, H. Weinfurter, A. Zeilinger, and M. Żukowski, "Multiphoton entanglement and interferometry", Reviews of Modern Physics **84**, 777–838 (2012).

[244]W. Li, B. Chen, C. Meng, W. Fang, Y. Xiao, X. Li, Z. Hu, Y. Xu, L. Tong, H. Wang, W. Liu, J. Bao, and Y. R. Shen, "Ultrafast All-Optical Graphene Modulator", Nano Letters **14**, 955–959 (2014).

[245]C. T. Phare, Y.-H. Daniel Lee, J. Cardenas, and M. Lipson, "Graphene electro-optic modulator with 30 GHz bandwidth", Nature Photonics **9**, 511–514 (2015).

[246]P. Sibson, J. E. Kennard, S. Stanisic, C. Erven, J. L. O'Brien, and M. G. Thompson, "Integrated silicon photonics for high-speed quantum key distribution", Optica **4**, 172 (2017).

[247]A. Leinse, R. G. Heideman, M. Hoekman, F. Schreuder, F. Falke, C. G. H. Roeloffzen, L. Zhuang, M. Burla, D. Marpaung, D. H. Geuzebroek, R. Dekker, E. J. Klein, P. W. L. van Dijk, and R. M. Oldenbeuving, "TriPleX waveguide platform: low-loss technology over a wide wavelength range", in Integrated photonics: materials, devices, and applications II, edited by J.-M. Fédéli, L. Vivien, and M. K. Smit, May 2013 (May 2013), 87670E.

[248]I. Agha, S. Ates, M. Davanço, and K. Srinivasan, "A chip-scale, telecommunications-band frequency conversion interface for quantum emitters", Optics Express **21**, 21628 (2013).

[249]B. Baek, A. E. Lita, V. Verma, and S. W. Nam, "Superconducting a-WxSi1-x nanowire single-photon detector with saturated internal quantum efficiency from visible to 1850 nm", Applied Physics Letters **98**, 251105 (2011).

[250]F. Najafi, J. Mower, N. C. Harris, F. Bellei, A. Dane, C. Lee, X. Hu, P. Kharel, F. Marsili, S. Assefa, K. K. Berggren, and D. Englund, "On-chip detection of non-classical light by scalable integration of single-photon detectors", Nature Communications **6**, 5873 (2015).

[251]J. P. Sprengers, A. Gaggero, D. Sahin, S. Jahanmirinejad, G. Frucci, F. Mattioli, R. Leoni, J. Beetz, M. Lermer, M. Kamp, S. Höfling, R. Sanjines, and A. Fiore, "Waveguide superconducting single-photon detectors for integrated quantum photonic circuits", Applied Physics Letters **99**, 181110 (2011).

[252]W. Pernice, C. Schuck, O. Minaeva, M. Li, G. Goltsman, A. Sergienko, and H. Tang, "High-speed and high-efficiency travelling wave single-photon detectors embedded in nanophotonic circuits", Nature Communications **3**, 1325 (2012).

[253]A. E. Lita, A. J. Miller, and S. W. Nam, "Counting near-infrared single-photons with 95% efficiency", Optics Express **16**, 3032 (2008).

[254]D. Achilles, C. Silberhorn, C. Śliwa, K. Banaszek, and I. A. Walmsley, "Fiber-assisted detection with photon number resolution", Optics Letters **28**, 2387 (2003).

[255]M. Grimau Puigibert, G. H. Aguilar, Q. Zhou, F. Marsili, M. D. Shaw, V. B. Verma, S. W. Nam, D. Oblak, and W. Tittel, "Heralded Single Photons Based on Spectral Multiplexing and Feed-Forward Control", Physical Review Letters **119**, 083601 (2017).

[256]Q. Li, M. Davanço, and K. Srinivasan, "Efficient and low-noise single-photon-level frequency conversion interfaces using silicon nanophotonics", Nature Photonics **10**, 406–414 (2016).

[257]C. E. Shannon, "A Mathematical Theory of Communication", Bell System Technical Journal **27**, 623–656 (1948).

[258]H.-J. Briegel, W. Dür, J. I. Cirac, and P. Zoller, "Quantum Repeaters: The Role of Imperfect Local Operations in Quantum Communication", Physical Review Letters **81**, 5932–5935 (1998).

[259]R. Horodecki, P. Horodecki, M. Horodecki, and K. Horodecki, "Quantum entanglement", Reviews of Modern Physics **81**, 865–942 (2009).

[260]T. Inagaki, N. Matsuda, O. Tadanaga, M. Asobe, and H. Takesue, "Entanglement distribution over 300 km of fiber", Optics Express **21**, 23241 (2013).

[261]K. Kutluer, M. Mazzera, and H. de Riedmatten, "Solid-State Source of Nonclassical Photon Pairs with Embedded Multimode Quantum Memory", Physical Review Letters **118**, 210502 (2017).

[262]S. L. Mouradian, T. Schröder, C. B. Poitras, L. Li, J. Goldstein, E. H. Chen, M. Walsh, J. Cardenas, M. L. Markham, D. J. Twitchen, M. Lipson, and D. Englund, "Scalable Integration of Long-Lived Quantum Memories into a Photonic Circuit", Physical Review X **5**, 031009 (2015).

[263]R. Zhao, Y. O. Dudin, S. D. Jenkins, C. J. Campbell, D. N. Matsukevich, T. A. B. Kennedy, and A. Kuzmich, "Long-lived quantum memory", Nature Physics **5**, 100–104 (2009).

[264]K. F. Reim, J. Nunn, V. O. Lorenz, B. J. Sussman, K. C. Lee, N. K. Langford, D. Jaksch, and I. A. Walmsley, "Towards high-speed optical quantum memories", Nature Photonics **4**, 218–221 (2010).

[265]G. D. Fuchs, G. Burkard, P. V. Klimov, and D. D. Awschalom, "A quantum memory intrinsic to single nitrogen–vacancy centres in diamond", Nature Physics **7**, 789–793 (2011).

[266]K. C. Lee, M. R. Sprague, B. J. Sussman, J. Nunn, N. K. Langford, X. M. Jin, T. Champion, P. Michelberger, K. F. Reim, D. England, D. Jaksch, and I. A. Walmsley, "Entangling Macroscopic Diamonds at Room Temperature", Science **334**, 1253–1256 (2011).

[267]M. Kroutvar, Y. Ducommun, D. Heiss, M. Bichler, D. Schuh, G. Abstreiter, and J. J. Finley, "Optically programmable electron spin memory using semiconductor quantum dots", Nature **432**, 81–84 (2004).

[268]A. G. Radnaev, Y. O. Dudin, R. Zhao, H. H. Jen, S. D. Jenkins, A. Kuzmich, and T. A. B. Kennedy, "A quantum memory with telecom-wavelength conversion", Nature Physics **6**, 894–899 (2010).

[269]Y.-W. Cho, G. T. Campbell, J. L. Everett, J. Bernu, D. B. Higginbottom, M. T. Cao, J. Geng, N. P. Robins, P. K. Lam, and B. C. Buchler, "Highly efficient optical quantum memory with long coherence time in cold atoms", Optica **3**, 100 (2016).

[270]M. Rančić, M. P. Hedges, R. L. Ahlefeldt, and M. J. Sellars, "Coherence time of over a second in a telecom-compatible quantum memory storage material", Nature Physics **14**, 50–54 (2017).

[271]E. Saglamyurek, J. Jin, V. B. Verma, M. D. Shaw, F. Marsili, S. W. Nam, D. Oblak, and W. Tittel, "Quantum storage of entangled telecom-wavelength photons in an erbium-doped optical fibre", Nature Photonics **9**, 83–87 (2015).

[272]M. V. G. Dutt, L. Childress, L. Jiang, E. Togan, J. Maze, F. Jelezko, A. S. Zibrov, P. R. Hemmer, and M. D. Lukin, "Quantum Register Based on Individual Electronic and Nuclear Spin Qubits in Diamond", Science **316**, 1312–1316 (2007).

[273]C. Simon, M. Afzelius, J. Appel, A. Boyer de la Giroday, S. J. Dewhurst, N. Gisin, C. Y. Hu, F. Jelezko, S. Kröll, J. H. Müller, J. Nunn, E. S. Polzik, J. G. Rarity, H. De Riedmatten, W. Rosenfeld, A. J. Shields, N. Sköld, R. M. Stevenson, R. Thew, I. A. Walmsley, M. C. Weber, H. Weinfurter, J. Wrachtrup, and R. J. Young, "Quantum memories", The European Physical Journal D **58**, 1–22 (2010).

[274]A. E. Kozhekin, K. Mølmer, and E. Polzik, "Quantum memory for light", Physical Review A **62**, 033809 (2000).

[275]K. A. G. Fisher, D. G. England, J.-P. W. MacLean, P. J. Bustard, K. J. Resch, and B. J. Sussman, "Frequency and bandwidth conversion of single photons in a room-temperature diamond quantum memory", Nature Communications **7**, 11200 (2016).

[276]B. A. Bell, J. He, C. Xiong, and B. J. Eggleton, "Frequency conversion in silicon in the single photon regime", Optics Express **24**, 5235 (2016).

[277]P. S. Donvalkar, V. Venkataraman, S. Clemmen, K. Saha, and A. L. Gaeta, "Frequency translation via four-wave mixing Bragg scattering in Rb filled photonic bandgap fibers", Optics Letters **39**, 1557 (2014).

[278]I. Agha, M. Davanço, B. Thurston, and K. Srinivasan, "Low-noise chip-based frequency conversion by four-wave-mixing Bragg scattering in SiN_x waveguides", Optics Letters **37**, 2997 (2012).

[279]R. V. Roussev, C. Langrock, J. R. Kurz, and M. M. Fejer, "Periodically poled lithium niobate waveguide sum-frequency generator for efficient single-photon detection at communication wavelengths", Optics Letters **29**, 1518 (2004).

[280]H.-P. Lo and H. Takesue, "Precise tuning of single-photon frequency using an optical single sideband modulator", Optica **4**, 919 (2017).

[281]L. Fan, C.-L. Zou, M. Poot, R. Cheng, X. Guo, X. Han, and H. X. Tang, "Integrated optomechanical single-photon frequency shifter", Nature Photonics **10**, 766–770 (2016).

[282]L. J. Wright, M. Karpiński, C. Söller, and B. J. Smith, "Spectral Shearing of Quantum Light Pulses by Electro-Optic Phase Modulation", Physical Review Letters **118**, 023601 (2017).

[283]S. Lefrancois, A. S. Clark, and B. J. Eggleton, "Optimizing optical Bragg scattering for single-photon frequency conversion", Physical Review A **91**, 013837 (2015).